Supplementary Information (SI) for Green Chemistry.

KuQuinone-sensitized cobalt oxide nanoparticles for photoelectrocatalytic oxygen evolution with visible light

Ruggero Bonetto,[a,b] Nuria Romero,*[c] Federica Sabuzi,*[d] Mattia Forchetta,[d] Mirco Natali,[e] Raffaella Signorini,[b] Roger Bofill,[b] Laia Francàs,[b] Marcos Gil-Sepulcre,*[a,f] Olaf Rüdiger,[f] Serena DeBeer,[f] Jordi García-Antón,[a] Karine Philippot,[c] Pierluca Galloni,[d] Andrea Sartorel,*[b] and Xavier Sala*[a]

a: *Department of Chemistry, Faculty of Sciences, Autonomous University of Barcelona, 08193 Bellaterra, Catalonia, Spain*

E-mail: xavier.sala@uab.cat

b: *Department of Chemical Sciences, University of Padova, Via Francesco Marzolo 1, 35131 Padova, Italy*

E-mail: andrea.sartorel@unipd.it

c: *CNRS, LCC (Laboratoire de Chimie de Coordination), UPR8241, University of Toulouse, UPS, INPT, Toulouse cedex 4 F-31077, France*

E-mail: nuria.romero@lcc-toulouse.fr

d: *Department of Chemical Science and Technologies, University of Rome Tor Vergata, Via Della Ricerca Scientifica, snc 001133 Rome, Italy*

E-mail: federica.sabuzi@uniroma2.it

e: *Department of Chemical, Pharmaceutical and Agricultural Sciences, Via Fossato di Mortara 17, 44121 Ferrara, Italy*

f: *Max Planck Institute Chemical Energy Conversion, Stiftstrasse 34-36, D-45470 Mülheim an der Ruhr, Germany*

E-mail: marcos.gil-sepulcre@cec.mpg.de

Index

1. General

1.1 Synthesis

1-heptanol-stabilized Co_3O_4 NPs (**$Co_3O_4^{heptOH}$**) and KuQuinone dyes were prepared following previously reported protocols. [1–4] The synthesis of **$KuQ_n@Co_3O_4$** is described in the Main Text (**Methods** section).

1.2. Inductively Coupled Plasma (ICP) measurements

Inductively Coupled Plasma optical emission and mass spectrometry (ICP-OES and ICP-MS) analysis were performed by the Chemical Analysis Service (SAQ) of the Autonomous University of Barcelona.

1.3. Transmission Electron Microscopy (TEM)

Grids for Transmission Electron Microscopy (TEM) analyses were prepared by dropcasting a drop of a colloidal suspension onto a carbon film-coated copper grid. TEM analyses were carried out either in “Centre de Microcaractérisation Raymond Castaing” in Toulouse (UMS-CNRS 3623) or at the “Servei de Microscòpia” of the Autonomous University of Barcelona, using for both a JEOL JEM 1400 electron microscope operating at 100 or 120 kV with resolution point of 4.5 Å. High Resolution Transmission Electron Microscopy (HR-TEM), High-Angle Annular Dark-Field Scanning Transmission Electron Microscopy (STEM-HAADF) and Energy Dispersive X-ray spectroscopy (EDX) analyses were performed using a JEOL JEM-ARM200F Cold FEG instrument equipped with a EDS/EELS detector with a resolution point < 1.9 Å. Statistical size distributions were done using ImageJ Fiji software. At least 150 NPs were manually measured, assuming spherical shape. Mean size and standard deviation were calculated using this method. Fast Fourier Transform (FFT) analysis was carried out using Digital micrograph software.

1.4. Determination of surface Co_3O_4 sites and of KuQ3P : Co_3O_4 surface ratio

Quantification of surface sites was carried out by using the magic number rule from Co NPs, and extrapolating the result to Co_3O_4 NPs. [5] Co density is 8.9 g·cm^{-3} for a molar mass of 58.9 g·mol^{-1}. Considering the Avogadro number, the number of Co atoms per unit volume can be calculated from **Eq. S1**:

$$\frac{8.9.10^{-21}\ \mathrm{g}\cdot\mathrm{nm}^{-3}}{58.9\ \mathrm{g}\cdot\mathrm{mol}^{-1}}\cdot 6.02\cdot\frac{10^{23}\mathrm{atoms}}{\mathrm{mol}} = 91\ \mathrm{Co\ atoms}\cdot\mathrm{nm}^{-3} \qquad (\textbf{Eq. S1})$$

For a spherical 3 nm sized Co NPs, the average particle volume is 14.1 nm^3 and the number of Co atoms per NP is 1283 atoms.

Then, the magic number rule was applied for Co hcp structure: 1 + 14 + 50 + 110 + 194 + 302 + 434 = 1105 atoms in a 6 completed-shell particle.[5] The percentage of Co atoms at the surface was therefore calculated from **Eq. S2**:

$$\%Surface\ atoms = \frac{434}{1105} \cdot 100 = 39.3\% \qquad (\textbf{Eq. S2})$$

As a result, approximately 434 Co atoms are at the surface of $\mathbf{Co^{heptOH}}$ NPs. Extrapolating this result to $\mathbf{Co_3O_4^{heptOH}}$ NPs, *ca* 145 Co_3O_4 units are present at the surface, namely $[Co_3O_4]_{surface}$.The calculated surface fraction then allowed to determine the **KuQ3P** : $[Co_3O_4]_{surface}$ ratio, namely 1 : 3.9 and 1 : 1.9 for $\mathbf{KuQ3P_{0.1}@Co_3O_4}$ and $\mathbf{KuQ3P_{0.2}@Co_3O_4}$, respectively.

A quantitatively comparable result was obtained through a different approximation following the procedure reported by Bazzan *et al.*, applied to a 3 nm diameter spherical $\mathbf{Co_3O_4^{heptOH}}$ NP (surface, Σ = 28.274 nm^3; volume, V = 14.137 nm^3).[6] Briefly, the Co_3O_4 surface fraction was estimated from the lattice parameter of the Co_3O_4 unit cubic cell (l = 0.808 nm; σ = 0.6529 nm^2; v = 0.5275 nm^3, each cubic cell containing 8 Co_3O_4 units)[7] and their comparison to the surface and volume of the NP, according to **Eq. S3**.

$$\%Surface\ Co_3O_4 = \left(\frac{\Sigma}{\sigma}\right) \cdot \left(\frac{v}{V}\right) \cdot \frac{1}{4} \cdot 100 = 40\% \qquad (\textbf{Eq. S3})$$

2. Photoanodes preparation

FTO|SnO_2 photoanodes were prepared by blade-coating and thermally sintering a colloidal SnO_2 paste on clean FTO slides, following previously reported protocols. [8,9]

2.1. Dyad-based photoanodes

KuQ3P$_n$@Co$_3$O$_4$ NPs were suspended upon sonication (10 min) in freshly distilled THF to reach *ca* 1.7 mg·mL^{-1} concentration. Subsequently, aliquots of the colloidal suspension were deposited by dropcasting on the FTO|SnO_2 photoelectrodes. In between depositions, the substrates were dried with a gentle stream of air. Deposition was carefully restricted to the SnO_2 film.

To provide a meaningful comparison between the hybrid nanomaterials, photoanodes were prepared in order to attain a 140 nmol$_{dye}$·cm^{-2} nominal molar amount of **KuQ**. By knowing the molar mass of the hybrid nanomaterials (MW_{NP}) (independently determined by ICP and summarized in **Tables S1-S2**), the internal molar equivalents of **KuQ3P** dye in the dyads (n), the specific mass of hybrid nanomaterials ($\tilde{m}$) to be deposited on the FTO|SnO_2 photoelectrodes could be calculated by **Eq. S4**:

$$\tilde{m}\ (\mu g_{NP} \cdot cm^{-2}) = \frac{140\ nmol_{dye} \cdot cm^{-2}}{n\left(mol_{dye} \cdot mol_{NP}^{-1}\right)} \cdot MW_{NP}\ (g \cdot mol^{-1}) \cdot 10^{-3}\ (ng \cdot mg^{-1}) \qquad \textbf{(Eq. S4)}$$

By imposing the mass concentration of the colloidal suspension (c_{coll}) and the geometric area of the SnO_2 film (A), the total volume of colloidal suspension of NPs to be deposited (v_d) was calculated (**Eq. S5**):

$$v_d\ (\mu L) = A\ (cm^2) \cdot \frac{\tilde{m}\ (\mu g_{NP} \cdot cm^{-2})}{c_{coll}\ (mg \cdot mL^{-1})} \qquad \textbf{(Eq. S5)}$$

2.2. Dye-sensitized FTO|SnO_2 photoelectrodes preparation

2.2.1. SnO_2|KuQ3C, SnO_2|KuQ3P

Sensitization with **KuQ** dyes was performed based on the method already reported by some of us.[8,9] FTO|SnO_2 films were sensitized with **KuQ3C** by soaking for 24 h in a 0.11 mM solution of **KuQ3C** in THF. 2.0 mL of solution were used for each photoelectrode. Given the long dyeing time, the solvent was not distilled prior to use. After soaking, the photoelectrodes were recovered, rinsed with freshly distilled THF, and dried with a gentle stream of N_2. The photoelectrodes were then immersed in aqueous H_2SO_4 (pH 2.0) to achieve complete conversion of the dye to its enol form. This treatment greatly improves the chemical stability of the film in aqueous solution, due to the formation of a hydrophobic layer able to protect anchoring moieties from hydrolysis.[8] Sensitization with **KuQ3P** was achieved by soaking the SnO_2 films in a 0.15 mM solution of **KuQ3P** dye solution in methanol for 24 h, followed by rinsing with methanol and drying under a stream of N_2. 2.0 mL of solution were used for each photoelectrode. Incidentally, the photoelectrodes sensitized with **KuQ3P** displayed features consistent with the enol form of the dye before exposure to acid, plausibly due to the lower pK_a of the first deprotonation of the phosphonic function (**Figure S47**).[10] Regardless, the acidic treatment was performed also on SnO_2|**KuQ3P** photoelectrodes for consistency.

After acidic treatment, the photoelectrodes were rinsed with mQ water and dried with a gentle stream of air. They were subsequently characterized by UV/Vis absorption spectrophotometry before and after acidic treatment. In order to quantify the amount of dye chemisorbed on the SnO_2 films (dye loading), the THF solutions were analyzed by UV/Vis absorption spectrophotometry with a 1.0 mm optical path quartz cuvette. An aliquot of the starting THF solution was kept for reference. Prior to spectrophotometric analysis, all **KuQ** solutions were acidified with 25 µL of *p*-toluenesulfonic acid to quantitatively convert **KuQ** to its enol form and diluted (1:10). Quantification was based on the absorbance at 563 nm ($\varepsilon_{563} = 1.5 \cdot 10^4$ $M^{-1} \cdot cm^{-1}$), using the Beer-Lambert law.[8]

Photoelectrodes and dye solutions were characterized by UV-Vis absorption on an Agilent Cary 60 spectrophotometer. Emission spectroscopy characterization on **KuQ**-sensitized SnO_2 films was performed with a FLS1000 fluorimeter by Edinburgh Instruments.

2.2.2. SnO_2|KuQ|$Co_3O_4^{heptOH}$

After dyeing, the photoelectrodes were functionalized by dropcasting a 1.50 mg·mL^{-1} suspension of **$Co_3O_4^{heptOH}$** in methanol to reach a 1:10 **KuQ : $Co_3O_4^{heptOH}$** molar ratio. After deposition, photoanodes were dried under a gentle stream of air.

3.1. X-ray Photoelectron Spectroscopy (XPS)

X-ray Photoelectron Spectroscopy (XPS) measurements were performed at the Catalan Institute of Nanoscience and Nanotechnology (ICN2) in Barcelona with a Phoibos 150 analyzer (SPECS GmbH, Berlin, Germany) in ultra-high vacuum conditions (base pressure $5 \cdot 10^{-10}$ mbar) with a monochromatic aluminum K-alpha X-ray 456 source (1486.74 eV). The energy resolution was measured by the FWHM of the Ag 3d5/2 peak which for a sputtered silver foil was 0.62 eV.

3.2. Resonance Raman spectroscopy

Raman measurements were conducted using a Micro-Raman setup. An argon ion laser emitting a single-line served as the excitation light source, featuring two primary lines at 488 and 514.5 nm (Spectra Physics Stabilite 2017 with an output power of 1 W). The 488 nm radiation was filtered out, and a half-wave plate was employed to control the polarization of the incident light. Optical density filters were strategically placed on a remotely controlled reel to regulate the intensity of light reaching the sample. The laser beam was coupled to a microscope (Olympus BX 40) and directed onto the sample through a 20× or 50× objective (Olympus SLMPL, NA D 0:75), resulting in a typical spot diameter of 3 or ~1 μm at the focus, respectively. The back-scattered Raman signal, distinct from Rayleigh scattering, was separated using an edge filter and subsequently analyzed through a 320 mm focal length imaging spectrograph (TRIAX-320 ISA) and a liquid nitrogen-cooled CCD camera (Spectrum One, JobinYvon). Each Raman spectrum was recorded utilizing the 50× microscope objective, and the spectrograph slit was set at 100 μm. Spectra were generated by averaging ten repeated measurements, each with an acquisition time of 10 seconds (10 seconds × 10 times).

3.3. Attenuated Total Reflection Infrared (ATR-FTIR) Spectroscopy

Infrared spectra were recorded on a Perkin Elmer spectrometer, equipped with a universal attenuated total reflectance (ATR) accessory with a diamond window in the range from 4000 to 500 cm^{-1}.

3.4. X-ray Absorption Spectroscopy (XAS)

XAS measurements were performed at CLÆSS (Static Co K-edge XAS and EXAFS) beamline (BL22) of the ALBA Synchrotron under proposals No. 2021095409 and 2022086973. The powder samples were measured as pellets mixing the cobalt samples with cellulose, covered with 38 μm Kapton tape and transferred to the sample holder. Photoelectrodes were prepared by using the standard protocol (see **Sections 2** and **5**), covered with 38 μm Kapton tape and transferred to the sample holder. The incident energy was selected by a Si (311) double crystal monochromator. The incident flux was *ca* $1 \cdot 10^{11}$ $ph \cdot sec^{-1}$ and X-rays were focused to achieve an approximate beam size of 250 μm × 500 μm (h × *v*). Samples were kept below 80 K in a N_2 LN_2-cryo cryostat during the measurements. The data were collected in transmission mode for powder samples (pellets), and in fluorescence mode for photoelectrodes using a 3-channel silicon-drift fluorescence detector. The incident energy was calibrated by assigning the first inflection point of Co foil spectra to 7709 eV. A step size of 0.2 eV and 0.5 eV were used in the pre-edge and edge XANES regions, respectively, and 1 eV in the EXAFS region (1 s integration time). Beam damage was evaluated during the measurements by performing fast scans in a single spot and attenuating the beam, and no evidence of photoreduction was observed during data collection. The XAS data treatment was performed using Athena and Artemis programs, included in the DEMETER software package.[11]

3.5. Photophysical characterization

Photoluminescence spectra were taken on an Edinburgh Instrument spectrofluorometer.

Fluorescence lifetimes were measured using a time-correlated single photon counting (TC-SPC) apparatus (PicoQuant Picoharp 300) equipped with a subnanosecond LED source (460 nm, 500−700 ps pulse width) powered by a PicoQuant PDL 800-B variable (2.5−40 MHz) pulsed power supply. The decays were analyzed by means of PicoQuant FluoFit Global fluorescence decay analysis software.

Transient absorption spectroscopy measurements were taken on a laser flash photolysis apparatus comprised of a Continuum Surelite II Nd:YAG laser (excitation at 532 nm, FWHM = 6–8 ns, provided by SHG from the 1064 nm fundamental). Light transmitted by the sample was focused onto the entrance slit of a 300 mm focal length Acton SpectraPro 2300i triple grating, flat field, and the double exit monochromator was equipped with a photomultiplier detector (Hamamatsu R3896). Signals from the photomultiplier were processed by means of a TeledyneLeCroy 604Zi (400 MHz, 20 GS/s) digital oscilloscope.

Analyses were performed on **KuQ3P$_{0.2}$@Co$_3$O$_4$** suspensions (0.3 mg·mL^{-1}) in $NaHCO_3/Na_2SiF_6$ (pH 5.6) buffer. **KuQ3P** emission quenching with and without sodium persulfate was studied in $NaHCO_3/Na_2SiF_6$ (pH 5.6) buffer solutions displaying an absorbance value of 0.5 at the excitation wavelength (λ_{exc} = 532 nm). The probed wavelength was λ_{em} = 610 nm.

4. Photoinduced oxygen evolution

Photoirradiation was performed in $NaHCO_3/Na_2SiF_6$ pH 5.60 buffer.[12,13,14] The reaction mixture contained 0.6–1.0 mg·mL^{-1} **$Co_3O_4^{heptOH}$** particles (weighed on a Mettler Toledo MX5 microbalance) and 84 mM $Na_2S_2O_8$. The particles and the persulfate were suspended and dissolved, respectively, in separate portions of the buffer and mixed in a custom-made 6 mL thermostated glass reactor (**Figures S23**, **S27**) prior to reaction. The temperature was kept at 25.0 °C by means of a water jacket controlled by a Huber thermostat. The reactor was sealed with a rubber septum. Oxygen content was monitored with a gas-phase Clark-type amperometric oxygen sensor (Unisense Ox-N needle microsensor) connected to a Unisense UniAmp ammeter. The probe needle of the Clark sensor was used to pierce the rubber septum and placed in the headspace of the photoreactor. The reaction mixture was degassed by sparging the liquid and gas phases with Ar gas for 20 minutes each. After degassing, the rubber septum was protected with Parafilm M and silicone grease.

The reactor was irradiated with an Abet Technologies LS150 150 W Xe short-arc lamp mounting an AM 1.5G filter and equipped with a 400 nm SP400LP Abet Technologies long-pass optical filter mounted on a Thorlabs SM1L03 holder. The distance between the light source and the photoreactor was set to reach a nominal incident power of 100 mW·cm^{-2}. A Thorlabs FDS100 Si photodiode (0.13 cm^2 detector area, responding to wavelengths in the range 350–1100 nm) connected to a digital multimeter was used to measure the incident light intensity.

The Clark sensor was calibrated after each photoirradiation session by degassing the reaction mixture and the reactor headspace with Ar and by performing subsequent additions of known volumes of O_2 with a gastight Hamilton syringe. A pseudo-calibration curve was constructed by plotting the steady-state differential signal of the Clark sensor after each gas addition as a function of the O_2 volume and, by means of the ideal gas law, of the molar amount of O_2 (**Figure S24**).

At the end of photoirradiation (**Figures S26**, **S27**, **S28**), the liquid phase was recovered and centrifuged. The supernatant was filtered over Celite. The residue was washed with mQ water (× 3), with methanol (× 3) and with diethyl ether (× 3), and finally left to dry to be further analyzed by ICP, TEM, HR-TEM and XAS. The experiments were either upscaled or performed multiple times to produce sufficient amounts of material for analysis. The results of the ICP analyses are summarized in **Table S4**.

After the photoirradiation experiments, the photoreactor and the stirrer bar were thoroughly cleaned by sonicating with *aqua regia* for 10 minutes followed by rinsing with deionized water, and finally sonicated with deionized water (10 minutes) and mQ water (5 minutes).

5. Electrochemical and Photoelectrochemical experiments

Cyclic Voltammetry (CV), Linear Sweep Voltammetry (LSV), Chronoamperometry (CA) and Open Circuit Chronopotentiometry (OC-CP) experiments on photoelectrodes were performed in a glass single-compartment cell (**Figure S38**) by using $NaHCO_3/Na_2SiF_6$ (pH 5.8) electrolyte. The cell was fitted with a PFTE holder. The working electrodes were FTO|SnO_2, the reference electrode was Ag/AgCl (3 M NaCl) (BASi), the auxiliary electrode was a glassy carbon disk (ø 3 mm, BASi). The working electrode was connected *via* an alligator clip soldered to a thin copper wire. The contacts were protected with a layer of Parafilm M to prevent contact with the electrolyte solution. The experiments were performed by means of a PalmSens4 potentiostat-galvanostat-impedance analyzer controlled with the PSTrace 5.9 software.

Photoelectrodes were irradiated from the side of the back contact with an Abet Technologies LS150 150 W Xe lamp equipped with a 400 nm SP400LP Abet Technologies long-pass optical filter mounted on a Thorlabs SM1L03 holder. A Thorlabs FDS100 Si photodiode connected to a digital multimeter was used to measure the incident light intensity, set to 100 $mW{\cdot}cm^{-2}$ for each photoelectrode. In chopped-light experiments, irradiation was manually interrupted by interposing a piece of black cardboard between the light source and the photoelectrochemical cell.

(Photo)current densities were in all cases reported considering the geometric area of the electrodes. In the case of CV experiments on **KuQ3P** in NaH_2PO_4/Na_2HPO_4 solution (pH 5.8, containing 0.5 M Na_2SO_4), a Metrohm Autolab PGSTAT2024 potentiostat-galvanostat controlled with Nova software was employed. A glassy carbon disk (ø 3 mm, BioLogic) working electrode, an Ag/AgCl (3 M NaCl) reference electrode and a Pt rod auxiliary electrode were used. The Ohmic drop was compensated *via* the positive feedback compensation implemented in the potentiostat-galvanostat. The working electrode was polished in between measurements, by using DP-Paste on a DP-Nap (Struers), followed by rinsing with ethanol, sonicating for 30 s in ethanol, rinsing and finally drying under a gentle stream of Ar.

In all cases, potentials were reported *vs* the Reversible Hydrogen Electrode (RHE), according to **Eq. S6**:

$$E\ (V\ vs\ RHE) = E\ (V\ vs\ Ag/AgCl, 3M\ NaCl) + 0.197 + 0.0592 \times pH \qquad \textbf{(Eq. S6)}$$

6. Determination of the Faradaic efficiency for O_2 evolution (FE_{O2})

The generator-collector method previously described was used to quantify evolved O_2.[8,15,16] Briefly, the photoanode, used as oxygen generator, was interfaced to a FTO electrode used as oxygen sensor (collector). Collector electrodes were pre-treated by 10 min sonication in KOH saturated in isopropanol (^{i}PrOH), 10 min sonication in ^{i}PrOH, and thermal treatment at 500 °C for 30 min in air, followed by natural cooling to room temperature. The inert spacer between the collector and generator electrodes was constituted by an H-shaped mask made with three layers of unstretched Parafilm M, with openings left to allow for electrolyte exchange between the bulk and the thin layer of solution between the electrodes (*ca* 0.5 mm). Connections were made *via* glue-free copper tape posed on the edge of each electrode. The contacts, the alligator clips, and all parts not intended to come into contact with the electrolyte solution were isolated by wrapping them with Parafilm M.

Once the contacts had been prepared and the Parafilm M mask was laid between the electrodes, these were clamped together by means of a custom-made PEEK frame held together by four polyamide nuts (realized by Lorenzo Dainese, technician in the Department of Chemical Sciences of the University of Padova). The setup is reproduced in **Figure S41**.

The experiments were run in a four-electrode setup controlled by a Metrohm Autolab PGSTAT302N bipotentiostat. The two working electrodes were the generator and collector electrodes, while an Ag/AgCl (3 M NaCl) (BASi) and a platinum wire were used as reference and auxiliary electrodes, respectively. The single-compartment glass cell was fitted with a PFTE holder. The photoanodes were illuminated with 100 $mW \cdot cm^{-2}$ simulated solar light from a LOT-Quantum Design solar simulator, equipped with an AM 1.5G filter and an Andover Corp. 400fh90-50s 400 nm long-pass optical filter to cut the contribution of UV light.

The electrolyte solution ($NaHCO_3$/Na_2SiF_6, pH 5.8) was introduced by means of a syringe after placing the electrodes in the cell, and thoroughly degassed with N_2 for 20 minutes before each measurement. During measurements, the electrolyte solution was kept under a blanket of N_2 provided by a gentle stream of the gas above the solution.

CAs were performed by poising the generator electrode at 1.14 V *vs* RHE and the collector electrode at –0.36 V *vs* RHE. This latter value was chosen as sufficiently cathodic to provide extensive oxygen reduction on FTO.[8] The experiments were constituted by a 100 s dark phase to ensure stabilization of the collector baseline current, followed by a 150 s illumination phase. In the case of longer-term experiments, the illumination phase was extended to 650 s. The expected anodic photocurrent response was indeed accompanied by a specular cathodic current at the collector electrode, after an induction time associated with O_2 diffusion. Finally, after interrupting the illumination phase, chronoamperograms were recorded to ensure complete consumption of the evolved O_2, indicated by a decay to the baseline signal of the collector current (usually 200 s were required). Determination of the Faradaic efficiency for O_2 evolution (FE_{O2}) was performed by integrating the generator photocurrent during the illumination phase and the collector current during the illumination phase and the subsequent dark recovery phase, according to **Eq. S7**:

$$FE_{O_2} = \frac{Q_C}{Q_G} \times \frac{1}{\eta_{coll}} \qquad \textbf{(Eq. S7)}$$

Where Q_C and Q_G are the charge flowing through the collector and generator electrodes, respectively. Q_G is the integrated photocurrent trace during the illumination phase, while Q_C is the integrated current trace at the collector during the illumination and recovery phases.

The collection efficiency of the setup, η_{coll}, was independently determined *via* calibration of the cell.[8,16] The equipment, the electrolyte, and the degassing procedures were the same as those used for the experiments on photoanodes. The cell was calibrated by employing a FTO generator interfaced with a FTO collector poised at –0.36 V *vs* RHE. The double-step chronoamperometric experiments were composed by a first phase (60 s), in which the generator was poised at 1.14 V *vs* RHE, followed by a second phase (120 s) in which the generator potential was stepped to a higher value, so to access electrocatalytic oxygen evolution by the FTO generator. Oxygen evolution was induced to an increasing degree by varying the generator potential during this second oxygen-evolving phase, from 1.94 V *vs* RHE to 2.44 V *vs* RHE in a series of experiments. Incidentally, this chronoamperometric method was intended as a viable strategy to produce variable generator charges, and therefore to vary the amount of O_2 evolved in the thin layer between the working electrodes, *in the same time interval*. An equivalent method could have relied on working at a single oxygen-evolving generator potential at variable times. Finally, the generator potential was brought back to 1.14 V *vs* RHE to measure the recovery trace until complete exhaustion of the evolved O_2 by the collector (*ca* 240 s). The outcome of the calibration experiments is reported in **Figure S42**.

This procedure provides a calibration setup in the closest conditions to the photoelectrocatalytic regime. Conceptually, the second potential step is intended as a simulation of the irradiation phase during photoelectrochemical experiments.

Integration of the generator (during the second phase) and collector (during the second and third phases) current traces provided the charges Q_G and Q_C used to construct the calibration curve (**Figure S42**, bottom) under the assumption of unit Faradaic efficiency for WO by the FTO generator. The slope of the calibration curve was used as the collection efficiency of the cell (η_{coll} = 76%).

7. Incident photon-to-current conversion efficiency (IPCE) determination

Experiments were performed by employing a custom-made PFTE one-compartment cell equipped with two diametrically opposed quartz windows, in between of which the photoanodes (used as working electrodes) were located. Cell design allowed for fitting on common holders compatible with optical benches. The electrical contact was achieved by means of a PTFE clamp internally lined with copper foil and containing a copper cylinder (ø 1 mm), fitted through a rubber septum to allow for height regulation (**Figure S53**).

A PalmSens4 potentiostat was used to control the cell. The auxiliary electrode (glassy carbon disk, ø 3 mm, BASi) and the reference electrode (Ag/AgCl, 3 M NaCl, BASi) were inserted through a distinct port and located adjacent to the working electrode. The electrolyte solution ($NaHCO_3$/Na_2SiF_6, pH 5.8) was introduced by means of a syringe after inserting and connecting the electrodes.

The setup used for the IPCE determination in full photo-action spectral measurements was courtesy of Prof. Jordi Hernando (Autonomous University of Barcelona) and is depicted in **Figure S53**. The light source was a 150 W Xe short-arc lamp powered by an Applied Photophysics 04-122 Power Controlled Lamp Supply and mounted in an Applied Photophysics lamp housing. The light beam was collimated by means of optical lenses of an Applied Photophysics Laser Kinetic Spectrometer. Monochromatic irradiation was obtained with an Applied Photophysics 05-109 pbp SpectraKinetic Monochromator controlled *via* custom-made software. Inlet and outlet slit openings of 5 mm were selected to maximize the irradiance output and obtain a better signal-to-noise ratio in photoelectrochemical experiments. The photoelectrochemical cell was placed in front of the monochromator. Illumination of the photoanode was performed from the side of its back contact.

CAs were recorded at 1.14 V *vs* RHE. A 10 s dark phase was followed by 30 s of illumination and, finally, by another 10 s dark phase. Steady-state photocurrent densities were measured from the difference between the stabilized photocurrent at the end of the 30 s illumination phase and the stabilized dark current in the last dark phase of the experiment (**Figure S53**).

The incident light irradiance was measured with a Thorlabs S120VC photodiode connected to a Thorlabs PM100A power meter (responsive in the range 200–1100 nm, detector area 0.94 cm^2).

When using LED sources as monochromatic light sources, the cell was fitted to a Thorlabs MB3060U/M optical bench by means of Thorlabs BA1S/M mounting base. Irradiation was performed using Thorlabs M680L4, M590L4, M530L4, M490L4, M430L4, M405L4 LED sources (λ_{em} = 680 nm, 590 nm, 530 nm, 490 nm, 430 nm, 405 nm, respectively), equipped with Thorlabs FB680-10, FB590-10, FB530-10, FB490-10, FB430-10, FB405-10 band-pass optical filters to achieve a FWHM of 10 nm, and with a Thorlabs SM1U25-A collimator.

The light was collimated to fully illuminate the optical quartz window of the photoelectrochemical cell. The output power of the LEDs was regulated by connecting the light sources to a Thorlabs LEDD1B driver. The power was selected to provide photocurrents in the range of those obtained with the Xe lamp-monochromator system. The setup is displayed in **Figure S54**. The irradiance was measured, as in the case of the Xe lamp source, with a Thorlabs S120VC photodiode connected to a Thorlabs PM100A power meter.

The conversion efficiency of incident light into photocurrent by a photoelectrode is quantified by the incident photon-to-current conversion efficiency (IPCE).[17,18] It is expressed as per **Eq. S8**:

$$IPCE\ (\%) = \frac{\Phi_e}{\Phi_{hv}} \times 100 \qquad \textbf{(Eq. S8)}$$

In **Eq. S8**, Φ_e and $\Phi_{h\nu}$ are the fluxes of electrons and incident photons, respectively. The term Φ_e is related to the measured photocurrent density. The photon flux, on the other hand, is related to the power of the incident light.[19,20]

IPCE may be expressed to highlight its physico-chemical significance in microscopic terms by **Eq. S9**:

$$IPCE = LHE \times \varphi_{inj} \times \varphi_{coll} \qquad \textbf{(Eq. S9)}$$

The expression contains the terms φ_{inj} and φ_{coll}, the injection and collection yields, respectively. The light harvesting efficiency (LHE), on the other hand, represents the portion of incident photons that are absorbed by the photoactive element of the electrode (*i.e.*, by the dye molecules in a dye-sensitized photoelectrode), and is expressed by **Eq. S10**:

$$LHE = 1 - 10^{-Absorbance} \qquad \textbf{(Eq. S10)}$$

Eq. S9 may be reformulated in terms of the photocurrent density (J, in $\mu A \cdot cm^{-2}$) and of the irradiance (P, in $W \cdot m^{-2}$) at each individual wavelength (λ, in nm), following **Eq. S11**:

$$IPCE \approx 1240 \times \frac{J_\lambda}{\lambda \times P_\lambda} \qquad \textbf{(Eq. S11)}$$

8. KuQ3P excited state potential determination

Excited state redox potentials for **KuQ3P** were determined according to **Eq. S12**:[21]

$$E^0(\boldsymbol{KuQ3P}^*/\boldsymbol{KuQ3P}^{\bullet-}) = E^0_{\boldsymbol{KuQ3P/KuQ3P}^{\bullet-}} + \frac{\Delta G_{\boldsymbol{KuQ3P}^*}}{e_0} \qquad \textbf{(Eq. S12)}$$

In **Eq. S12**, $\Delta G_{\mathbf{KuQ3P^*}}$ is the energy stored in the excited state of the dye (**^{1*}KuQ3P**), expressed in eV (and thus in V *vs* NHE) upon division by the elemental charge (*e_0*). In the present work, it is estimated from the crossing point between the normalized electronic absorption and emission spectra of the dye ($E_{0–0}$) in aqueous $NaHCO_3$/Na_2SiF_6 buffer (**Figure S18**), being 2.19 eV, *i.e.*, 2.53 V *vs* RHE. To obtain a value closer to the photoelectrochemical regime applied in the study, with **KuQ3P** being anchored on a metal oxide surface, we also recorded the spectra on FTO|SnO_2 films functionalized with **KuQ3P**. From the data in **Figure S18**, we estimated $E_{0–0}$ = 2.02 eV, corresponding to 2.36 V *vs* RHE at pH 5.8.

E^0(**KuQ3P/KuQ3P$^{\bullet-}$**) is the standard reduction potential for **KuQ3P** in the ground state, approximated to the half-wave potential ($E_{1/2}$) obtained from CV measurements on 0.2 mM **KuQ3P** at pH 5.8 (**Figure S19**), 0.26 V *vs* RHE.

Based on these considerations, **Eq. S12** can be expressed as per **Eq. S13**:

$$E^0(\boldsymbol{KuQ3P}^*/\boldsymbol{KuQ3P}^{\bullet-}) \approx E_{1/2}(vs\ RHE) + [E_{0-0}(eV) + 0.0592 \times pH] \qquad \textbf{(Eq. S13)}$$

By **Eq. S13**, we estimate an excited state potential E^0(**KuQ3P*/KuQ3P$^{\bullet-}$**) of 2.79 V *vs* RHE, slightly decreasing to 2.62 V *vs* RHE on SnO_2 films coherent with previous reports.[8,22]

9. Open circuit chronopotentiometry

The SnO_2|**$KuQ3P_n@Co_3O_4$** photoanodes were analyzed by open circuit chronopotentiometry (OC-CP) under dark/light intermittent cycles (**Figure S52** reports the traces for **$KuQ3P_{0.1}@Co_3O_4$** and **$KuQ3P_{0.2}@Co_3O_4$** compared with **$Co_3O_4^{heptOH}$**). The open circuit potential (V_{OC}) for SnO_2|**$KuQ3P_{0.2}@Co_3O_4$** was found to drop substantially under illumination (*ca* 170 mV, with V_{OC} stabilizing to 0.56 V *vs* RHE). The observed decrease of V_{OC} under illumination indicates a positive shift of the quasi-Fermi level of the electrons in SnO_2, in turn corresponding to a greater relative rate of charge injection under illumination conditions. When turning the irradiation off, the slow recovery trace indicates an effective mobilization of charge carriers in the SnO_2 film upon light absorption. Moreover, OC-CP measurements suggest that the degree of photoinduced charge mobilization within SnO_2 films is comparable for the two hybrid nanomaterials, as well as for the “unbound” photoelectrodes (**Figure S49**). This suggests a similar degree of charge mobilization within SnO_2 irrespective of the chemical linkage between **KuQ** dyes, SnO_2 and Co_3O_4 NPs. Therefore, we feel confident in **i)** ruling out charge injection as a factor limiting attainable photocurrent and **ii)** decoupling the effect of dye interaction with SnO_2 and Co_3O_4 NPs on photoinduced charge injection and FE_{O2}. On the other hand, electrodes prepared with unsensitized **$Co_3O_4^{heptOH}$** display a much lower voltage drop (82 mV) and a fast recovery trace, with V_{OC} rapidly reaching its pristine value in less than 30 s.[23–27]

10. Photoelectrocatalytic turnover frequency estimation

Estimation of TOF_{O2} for the dyad-based photoanodes was carried out by using **Eq. S14**:

$$TOF_{O_2} = \frac{J_{SS}}{n_e \times F} \times \frac{FE_{O_2}}{100} \times \frac{1}{n_{Co_3O_4}^{surface}} \qquad \textbf{(Eq. S14)}$$

In **Eq. S14**, J_{SS} are the steady-state photocurrent densities reported in **Table 1** in the Main Text (expressed in $A \cdot cm^{-2}$), n_e is the number of electrons required to oxidize H_2O to O_2 (4), F is the Faraday constant (96485 $C \cdot mol^{-1}$) , FE_{O2} the Faradaic efficiency for oxygen evolution (see **Table 1** in the Main Text) and $n_{Co3O4}^{surface}$ the catalyst loading (expressed in mol), scaled by the fraction of surface sites.

11. "Unbound" electrodes optical and photoelectrochemical characterization

Prior to **$Co_3O_4^{heptOH}$** loading, SnO_2|**KuQ** photoelectrodes were analyzed by means of spectroscopic techniques. Indeed, resonance Raman spectroscopy confirmed covalent anchoring of **KuQ3P** to SnO_2 (**Figure S37**). Subsequently, the transparent SnO_2 films were characterized by optical absorption spectroscopy in transmission mode. Accordingly, dye loading was estimated to be 140 $nmol \cdot cm^{-2}$ (see **Section 2.2**). The spectroscopic features of the dyes were identified both in the enolate, orange form (λ_{max} 510 nm) and in the enol, pink state (λ_{max} 533 nm, 570 nm), **Figure S47**. The two absorption maxima displayed by photoelectrodes obtained after acidic treatment were red-shifted with respect to solutions of **KuQ**, with a worse-resolved character of the peaks. Both observations were attributed to dye aggregation on the oxide film. Indeed, **KuQ**-functionalized photoanodes rely on π-stacking of dye molecules constituting a locally hydrophobic layer that prevents the deprotonation of the dye molecules (pK_a 4.7 in solution), otherwise spontaneous in the electrolyte solution.[8,9,28,29]

SnO_2|**KuQ3P** photoanodes were characterized by emission spectroscopy, registering their emission spectrum at an excitation wavelength of 510 nm. They exhibited a broad emission peaking at 700 nm, redshifted with respect to the dye in aqueous solution (see Main Text) likely due to aggregation. Estimation of the $E_{0\text{–}0}$ of **KuQ3P** anchored on SnO_2 films from the intersection between normalized absorption and emission spectra yielded 2.02 eV, a value consistent with previous reports.[10]

The SnO_2|**KuQ3C** and SnO_2|**KuQ3C|$Co_3O_4^{heptOH}$** photoelectrodes were tested in photoelectrochemical conditions, in $NaHCO_3/Na_2SiF_6$ (pH 5.8) electrolyte (**Figures S48–S49**). The LSV traces of the sensitized photoelectrodes in the absence of cobalt oxide display a photocurrent trend analogous to that measured by LSV for the dyad-based systems, albeit with higher photocurrents. CAs at 1.14 V *vs* RHE gave rise to initial photocurrent densities of 80 $\mu A \cdot cm^{-2}$, again rapidly decaying to a lower value (20 $\mu A \cdot cm^{-2}$). The higher photocurrents observed than in the case of the dyads are indeed ascribed to the direct chemical linkage between SnO_2 and the chromophore. As previously ascertained, the SnO_2|**KuQ** anodes are not kinetically able to perform the 4-electron water oxidation reaction: therefore, the photocurrent observed is to be ascribed to other photoinduced chemical processes. Substantial self-degradation or detachment of the dye on the timescale of the CA was excluded, given the restored photocurrent trace obtainable upon depolarization of the photoanode (**Figure S48**).

SnO_2|**KuQ3C** photoanodes were then modified by dropcasting a 1.50 mg·mL^{-1} suspension of **Co_3O_4^{heptOH}** in methanol (**Figure S49**), to attain a nominal dye:WOC 1:10 molar ratio and reproduce the composition of the **KuQ3P$_{0.1}$@Co_3O_4** dyad. An analogous procedure was followed for preparing SnO_2|**KuQ3P|Co_3O_4^{heptOH}** photoanodes, tested in Faradaic efficiency determination chronoamperometric experiments (*vide infra*).

Loading of **Co_3O_4^{heptOH}** resulted in physically stable photoelectrodes in the electrolyte solution, leaching of cobalt oxide particles being likely prevented by the hydrophobic 1-heptanol shell. The LSV and CA traces of SnO_2|**KuQ3C|Co_3O_4^{heptOH}** registered under irradiation reproducibly exhibited a decrease in photocurrent densities upon introduction of **Co_3O_4^{heptOH}**. Specifically, an initial photocurrent density of 30 µA·cm^{-2} decayed to 9 µA·cm^{-2} over the course of the 20 s illumination phase of the CA. Such observation may be rationalized upon invoking the high WOC loading on the photoelectrode. In fact, the presence of catalyst particles introduces electron scavenging sites that may result, assuming the reductive quenching mechanism, in back electron transfer from **KuQ$^{\bullet-}$** to the oxidized **Co_3O_4^{heptOH}**. The somewhat counterintuitive anti-catalytic effect of the presence of the catalyst on the photocurrent is therefore justified (see also the following **Section**). The introduction of a catalyst able to selectively drive the WO process may also contribute to the drop in photocurrent albeit through its productive mechanism: not only electrons funnelled in the circuit travel through a more complicated ET chain, but also they are garnered upon the slow water oxidation reaction. As a corollary, Finke and co-workers reported that a further detrimental role might be played by "carbon impurities" introduced by either the dye or the WOC deposition on SnO_2, this semiconducting oxide (SCO) being particularly affected by C-based recombination sites.[25] However, this aspect was not experimentally investigated for the **KuQ|Co_3O_4^{heptOH}** system.

12. Photoelectrochemical performance of SnO_2|KuQ3P$_n$@Co_3O_4 photoelectrodes

The two hybrid nanomaterials **KuQ3P$_{0.1}$@Co_3O_4** and **KuQ3P$_{0.2}$@Co_3O_4**, featuring a chromophore:catalytic site ratio 0.25:1 and 0.5:1, respectively, achieve a similar performance in terms of J_{SS} and FE_{O2} (see **Table 1** in the Main Text). Likewise, the turnover frequency for oxygen evolution (TOF_{O2}), determined from the latter parameters (*vide supra*, **Section 10**), provides analogous values of $5.3 \cdot 10^{-5} \cdot s^{-1}$ for **KuQ3P$_{0.1}$@Co_3O_4** and $6.3 \cdot 10^{-5} \cdot s^{-1}$ for **KuQ3P$_{0.2}$@Co_3O_4**. These observations may be interpreted functionally to rationalizing the limiting factors in the photoinduced electron transfer sequence, in turn determining photoanode performance. Indeed, the photocurrent decay observed in CA with respect to the initial anodic spike (**Figure 3B** in the Main Text) is indicative of charge injection by **KuQ3P$_n$@Co_3O_4** into SnO_2, that is not sustained over time.[25–28,32] Comparison of the two hybrid nanomaterials based on attainable photocurrents suggests that an increase in the amount of chromophore molecules within the Co_3O_4 NPs shell does not result in a higher photoanodic activity. Based on such combined evidence, we are confident in ruling out both **(i)** light harvesting and **(ii)** electron injection as limiting factors of our device. On the other hand, accumulation of oxidation equivalents on a catalytic Co_3O_4 site is comparatively more demanding, provided that it is carried out by single-photon, single-electron transfer events, albeit proton-coupled. Furthermore, the kinetically demanding WO poses an additional kinetic constraint to our system. Considering selective WO as the outcome of the productive fraction of the dye-sensitized photoanode operation cycles, the major shortcoming would therefore be: **(i)** intrinsically demanding kinetics of Co_3O_4, in turn allowing for **(ii)** back electron transfer from **KuQ3P$^{\bullet-}$** to progressively oxidized Co_3O_4, competing with electron injection by **KuQ3P$^{\bullet-}$** into the SnO_2 conduction band.[31,32]

KuQ3C$_{0.1}$@Co_3O_4, on the other hand, displays a more modest photoelectrochemical activity (**Figure S46**). Given the similar FE_{O2} associated to this material compared to **KuQ3P$_n$@Co_3O_4**, we infer a more than doubled TOF_{O2} for the hybrid nanomaterials constructed by using **KuQ3P** with respect to **KuQ3C**. The overall worse performance of **KuQ3C$_{0.1}$@Co_3O_4**, displaying photocurrent densities only 50% greater than unsensitized **$Co_3O_4^{heptOH}$** (**Figure S39**), is attributable to a less stable dye-WOC interaction that impairs its usability (see also caption of **Figure S45**).

13. Figures and Tables

	After synthesis		
	%Co	**%P**	**eq. KuQ3P**
$Co_3O_4^{heptOH}$	31	0	
$KuQ3P_{0.1}Co_3O_4$	35	0.52	0.08
$KuQ3P_{0.2}Co_3O_4$	33	1.02	0.18
0.1 eq **KuQ3P** + **$Co_3O_4^{heptOH}$**	9.3	0.39	–

Table S1. ICP analysis data (wt.%) relative to the **$Co_3O_4^{heptOH}$**-based NPs.

Particles	MW (g·mol⁻¹)
$Co_3O_4^{heptOH}$	564.28
$KuQ3P_{0.1}@Co_3O_4$	505.11
$KuQ3P_{0.2}@Co_3O_4$	535.73

Table S2. Molecular weights of the **$Co_3O_4^{heptOH}$**-based NPs calculated from ICP.

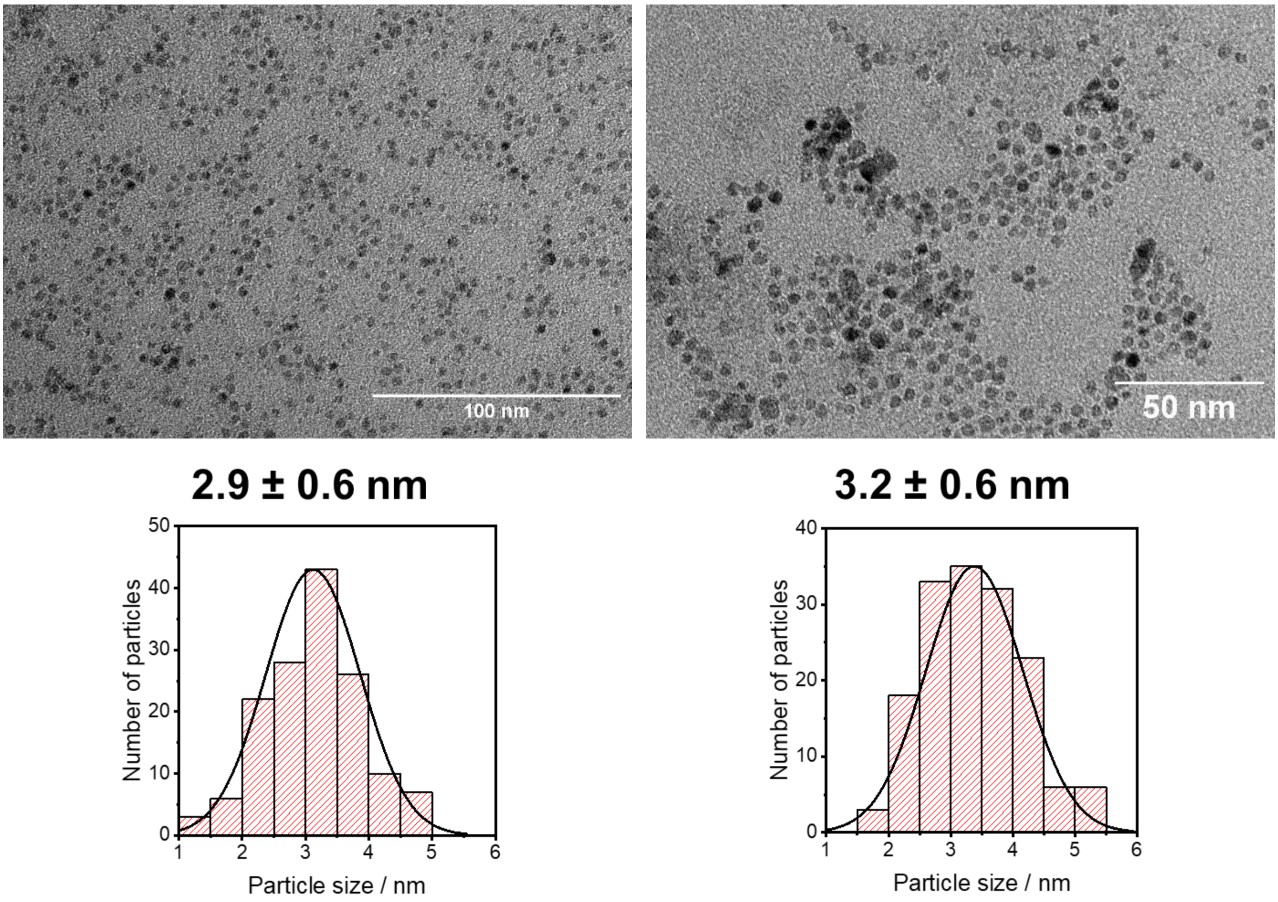

Figure S1. Top: HR-TEM images of **Co^{heptOH}** (**left**) and **$Co_3O_4^{heptOH}$** (**right**) NPs. **Bottom:** Size distribution for **Co^{heptOH}** (**left**) and **$Co_3O_4^{heptOH}$** (**right**) NPs.

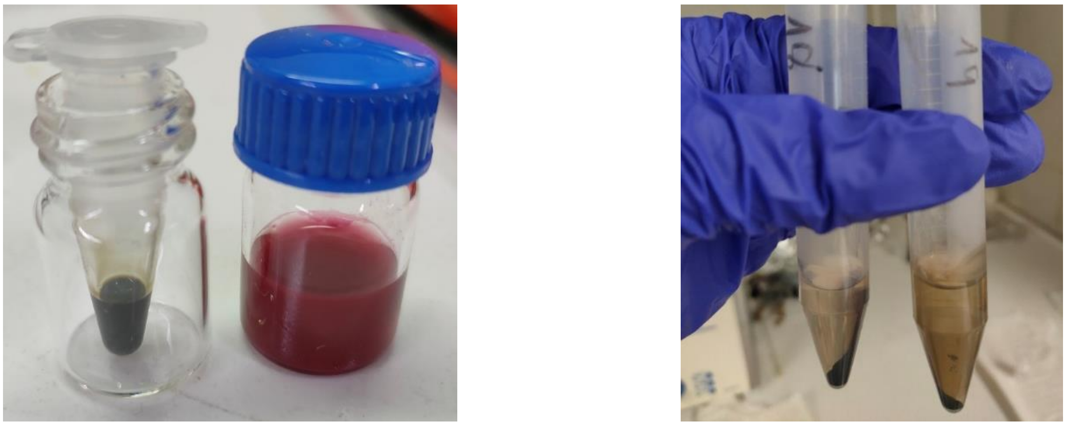

Figure S2. Pictures of the **$Co_3O_4^{heptOH}$** and **KuQ3P** suspension before mixing (**left**) and of the centrifuged suspension after stirring **KuQ3P** together with **$Co_3O_4^{heptOH}$** NPs (**right**).

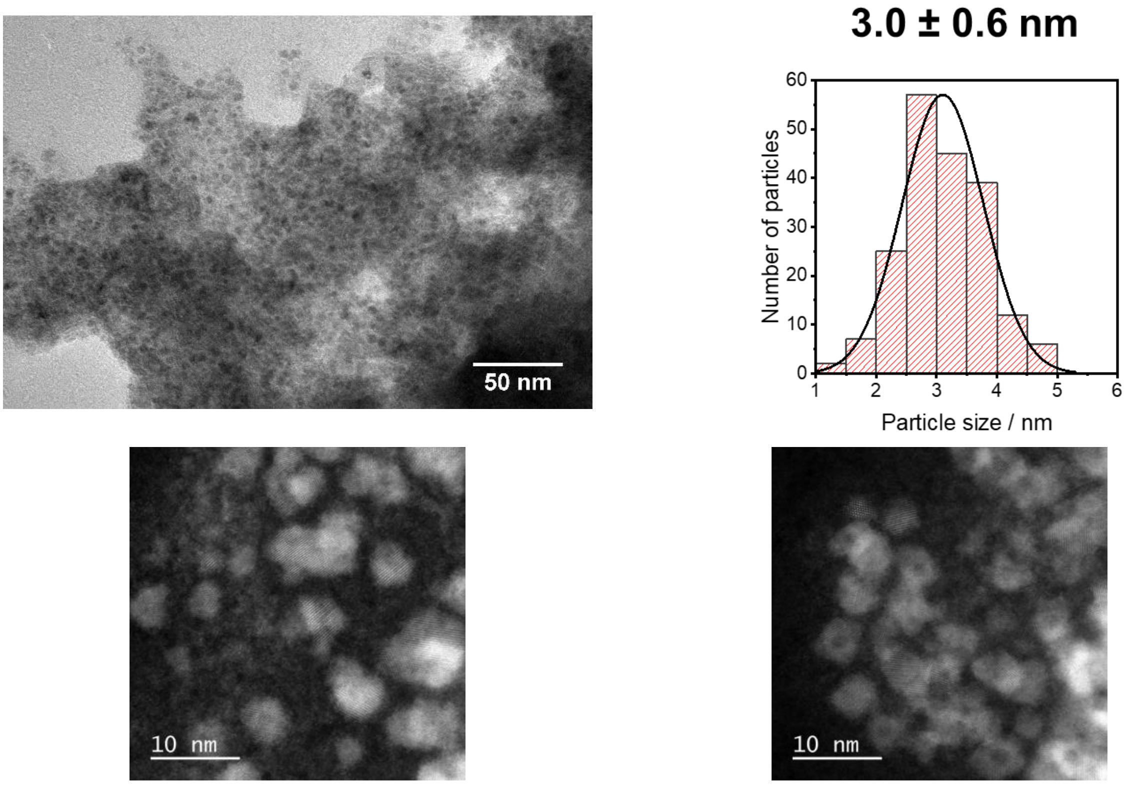

Figure S3. Top: HR-TEM image of **$KuQ3P_{0.2}@Co_3O_4$** NPs (**left**) and their size distribution (**right**). **Bottom:** STEM-HAADF images of **$KuQ3P_{0.2}@Co_3O_4$** NPs.

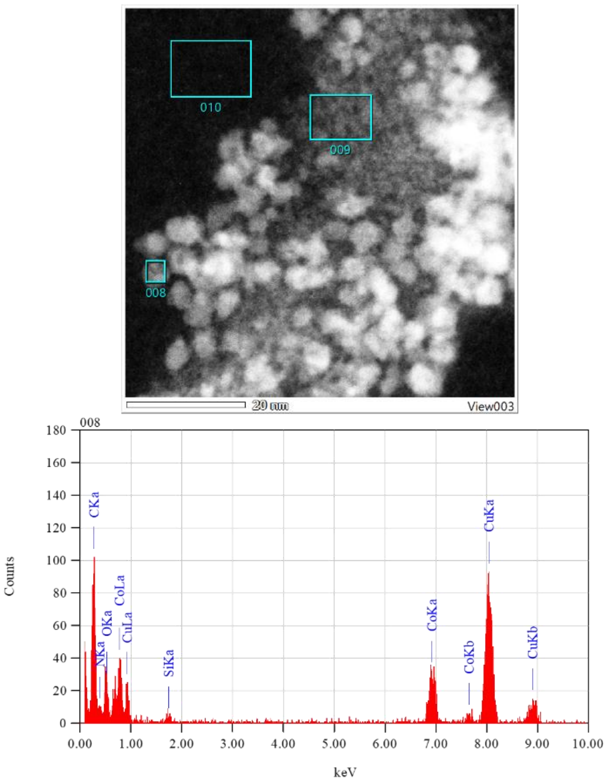

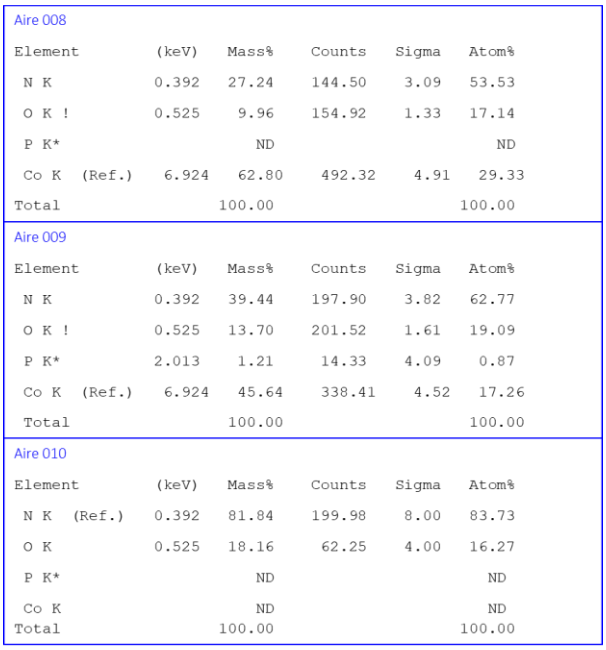
Aire 008

Element	(keV)	Mass%	Counts	Sigma	Atom%
N K	0.392	27.24	144.50	3.09	53.53
O K !	0.525	9.96	154.92	1.33	17.14
P K*		ND			ND
Co K (Ref.)	6.924	62.80	492.32	4.91	29.33
Total		100.00			100.00

Aire 009

Element	(keV)	Mass%	Counts	Sigma	Atom%
N K	0.392	39.44	197.90	3.82	62.77
O K !	0.525	13.70	201.52	1.61	19.09
P K*	2.013	1.21	14.33	4.09	0.87
Co K (Ref.)	6.924	45.64	338.41	4.52	17.26
Total		100.00			100.00

Aire 010

Element	(keV)	Mass%	Counts	Sigma	Atom%
N K (Ref.)	0.392	81.84	199.98	8.00	83.73
O K	0.525	18.16	62.25	4.00	16.27
P K*		ND			ND
Co K		ND			ND
Total		100.00			100.00

Figure S4. STEM-HDAAF image (**top left**) with corresponding EDX spectrum for **KuQ3P$_{0.1}$@Co$_3$O$_4$** NPs (**bottom left**) and corresponding elemental report for three selected locations (**right**).

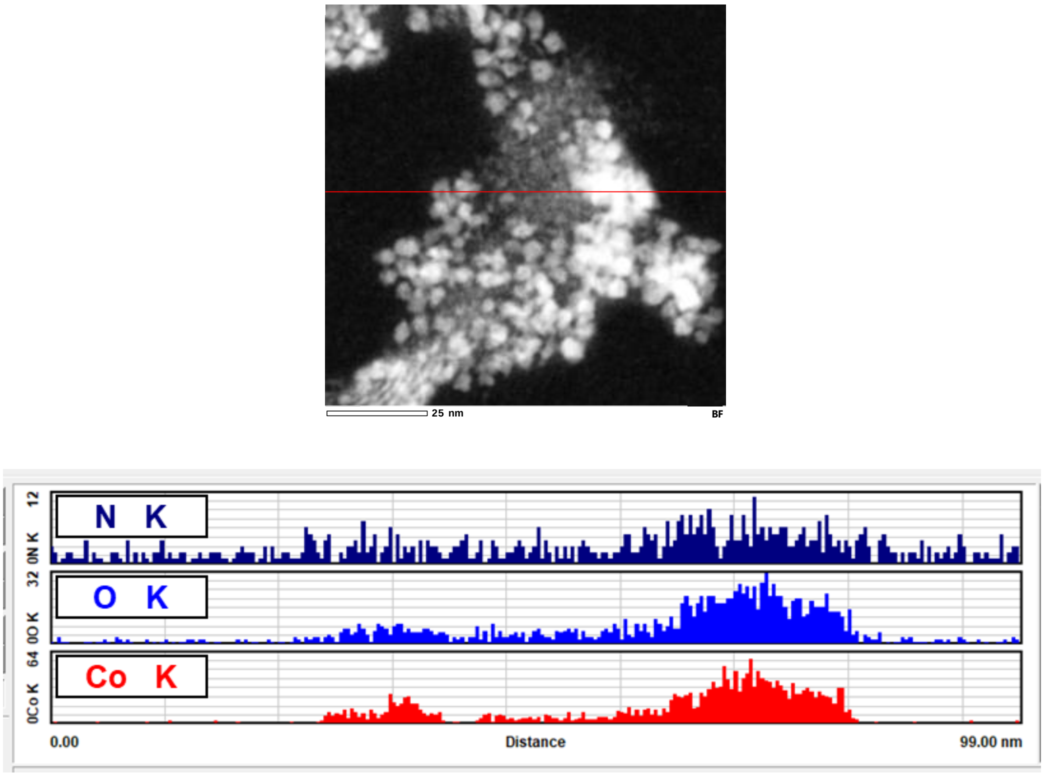

Figure S5. STEM-HAADF image with corresponding EDX spectrum for **KuQ3P$_{0.1}$@Co$_3$O$_4$** (**top**) and corresponding elemental spatial profile for N, O and Co K emission (**bottom**).

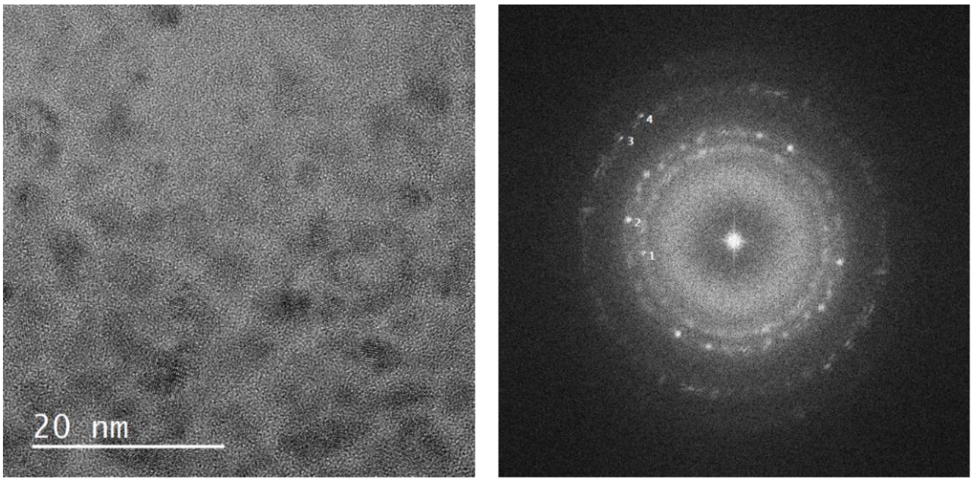

```
FFT of LNR1018-400000X-0012
-------------------------------------------------------------
    Spot#    d-Spacing (nm)    Rec. Pos.(1/nm)   Degrees to Spot 1
      1          0.2487            4.022               0.00
      2          0.2108            4.743              18.68
      3          0.1478            6.764              49.52
      4          0.1448            6.906              60.50
```

Figure S6. Electron diffraction pattern of **KuQ3P$_{0.1}$@Co$_3$O$_4$** NPs.

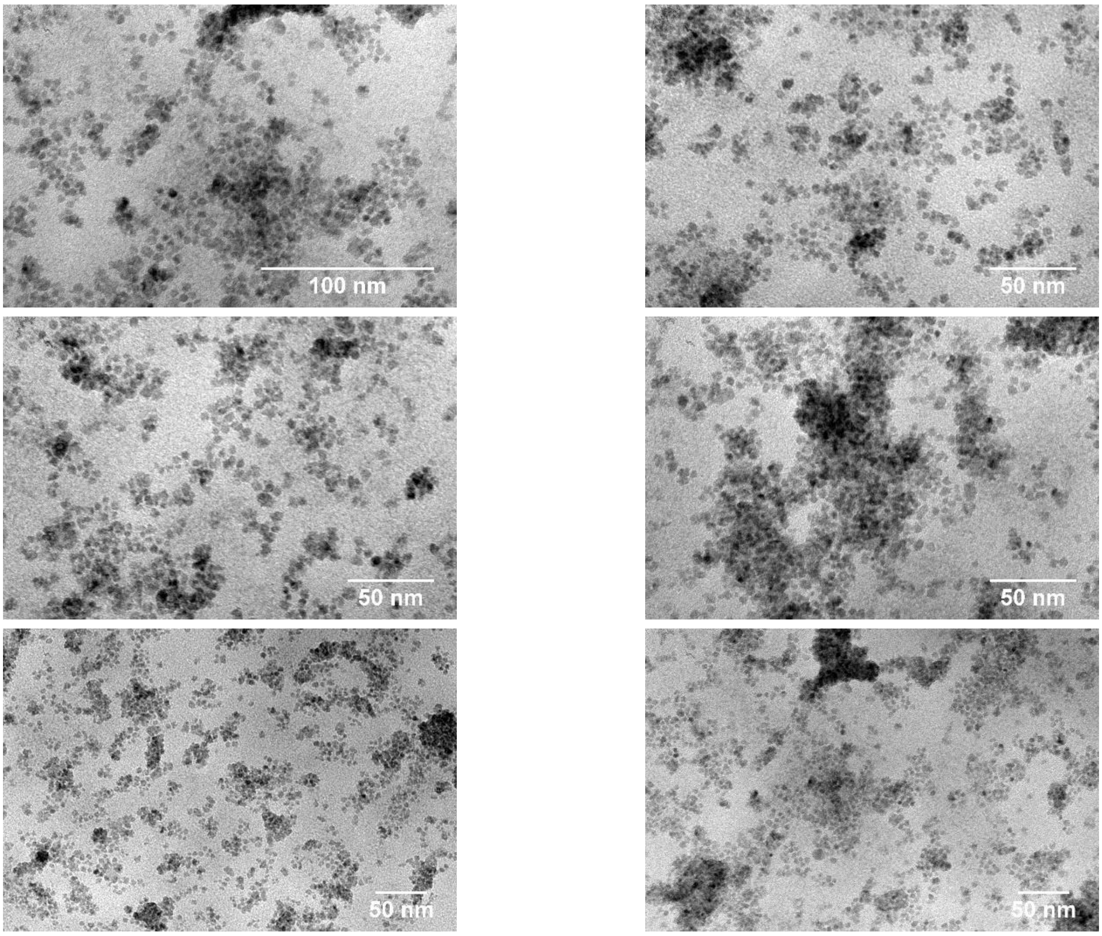

Figure S7. HR-TEM images of **Co$_3$O$_4$^{heptOH}** NPs subjected to stirring in H_2O/MeOH.

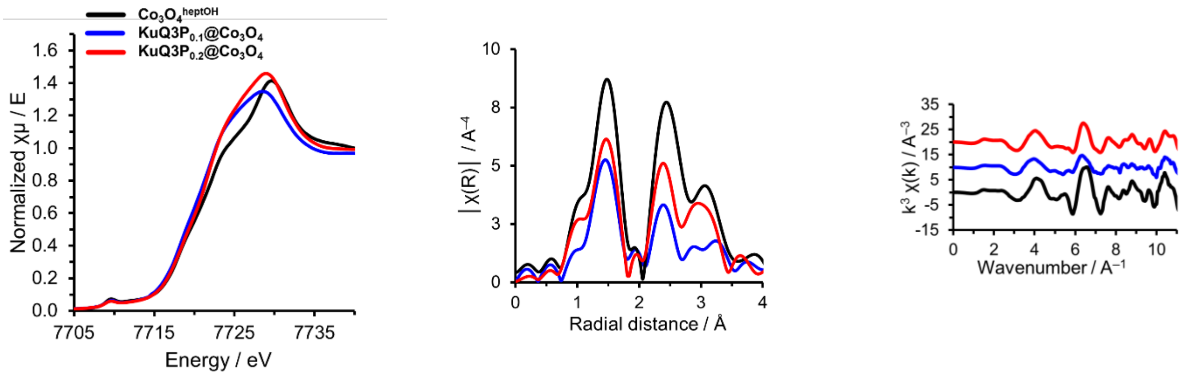

Figure S8. Left: Normalized Co K-edge spectra of **$Co_3O_4^{heptOH}$** (black lines), **KuQ3P$_{0.1}$@Co_3O_4** (blue lines) and **KuQ3P$_{0.2}$@Co_3O_4** (red lines). **Middle:** Fourier transforms of the k^3-weighted Co EXAFS spectra for the same samples. **Right:** Corresponding k^3-weighted Co EXAFS spectra.

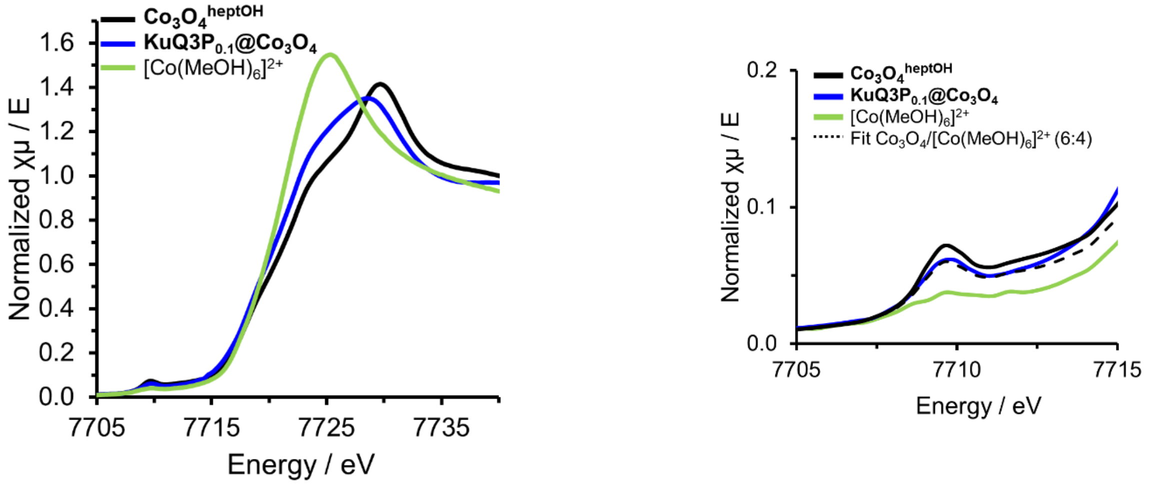

Figure S9. Left: Normalized Co K-edge spectra of **$Co_3O_4^{heptOH}$** (black lines), **KuQ3P$_{0.1}$@Co_3O_4** (blue lines) and $[Co(MeOH)_6]^{2+}$ (green lines), pretreated by dissolving $Co(BF_4)_2$ in pure MeOH. **Right:** Pre-edge region of normalized Co K-edge spectra of **$Co_3O_4^{heptOH}$**, **KuQ3P$_{0.1}$@Co_3O_4** and $[Co(MeOH)_6]^{2+}$ along with the fitting of the pre-edge with a mixture of **$Co_3O_4^{heptOH}$** and $[Co(MeOH)_6]^{2+}$ as a purely octahedrally coordinated model in a 6:4 ratio.

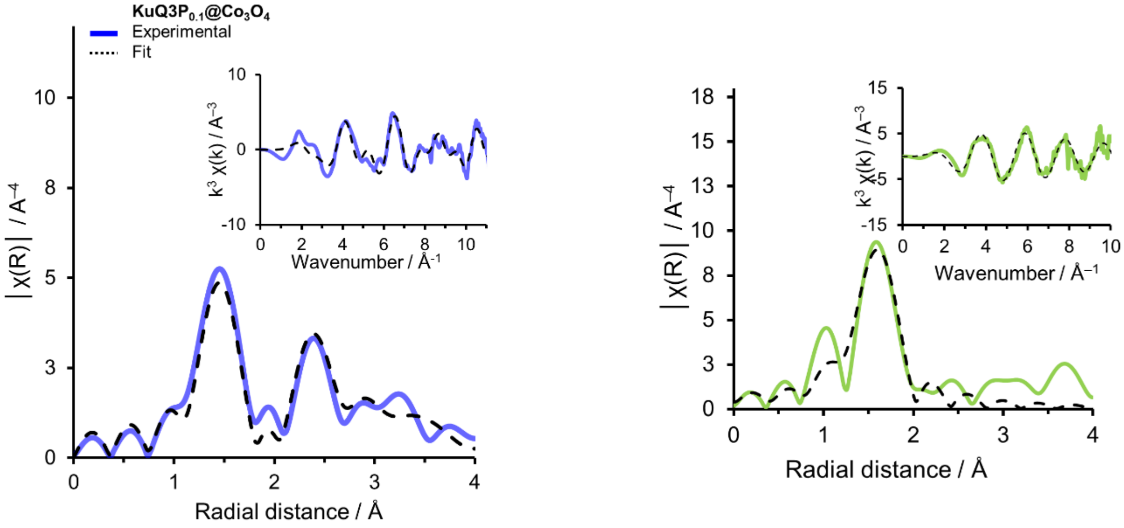

Figure S10. Fourier transforms of the k^3-weighted Co EXAFS spectra for **KuQ3P$_{0.1}$@Co$_3$O$_4$** (**left**, blue lines) and $[\mathrm{Co(MeOH)_6}]^{2+}$ (**right**, green lines). **Insets:** Corresponding k^3-weighted Co EXAFS spectra. Experimental data are represented as solid lines and fitted data as dashed lines. Experimental spectra were fitted for over a k-range 3–11 Å^{-1}.

Sample	Region	Shell, N	R, Å	σ² (10⁻³ Å²)	S_0^2	E_0, eV	R-factor	Reduced χ²
$[\mathrm{Co(MeOH)_6}]^{2+}$	k = 3 – 11	Co-O, 6	2.06	5.3	0.9	–3.7	0.035	44
	R = 1 – 4.2							

Table S3. EXAFS fitting parameters for $[\mathrm{Co(MeOH)_6}]^{2+}$ shown **Figure S10**. Fitting parameters for **KuQ3P$_{0.1}$@Co$_3$O$_4$** are reported in **Table S5**.

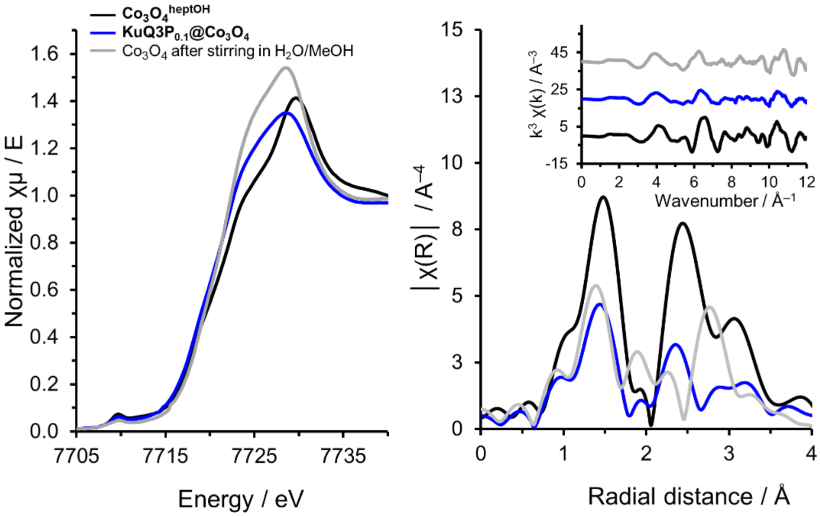

Figure S11. Left: Normalized Co K-edge spectra of **Co$_3$O$_4$$^{\mathrm{heptOH}}$** (black lines), **KuQ3P$_{0.1}$@Co$_3$O$_4$** (blue lines) and **Co$_3$O$_4$$^{\mathrm{heptOH}}$** treated under the same functionalization conditions than **KuQ3P$_{0.1}$@Co$_3$O$_4$** in the absence of **KuQ3P** (grey lines). **Right:** Fourier transforms of the k^3-weighted Co EXAFS spectra for the same samples. **Inset:** Corresponding k^3-weighted Co EXAFS spectra.

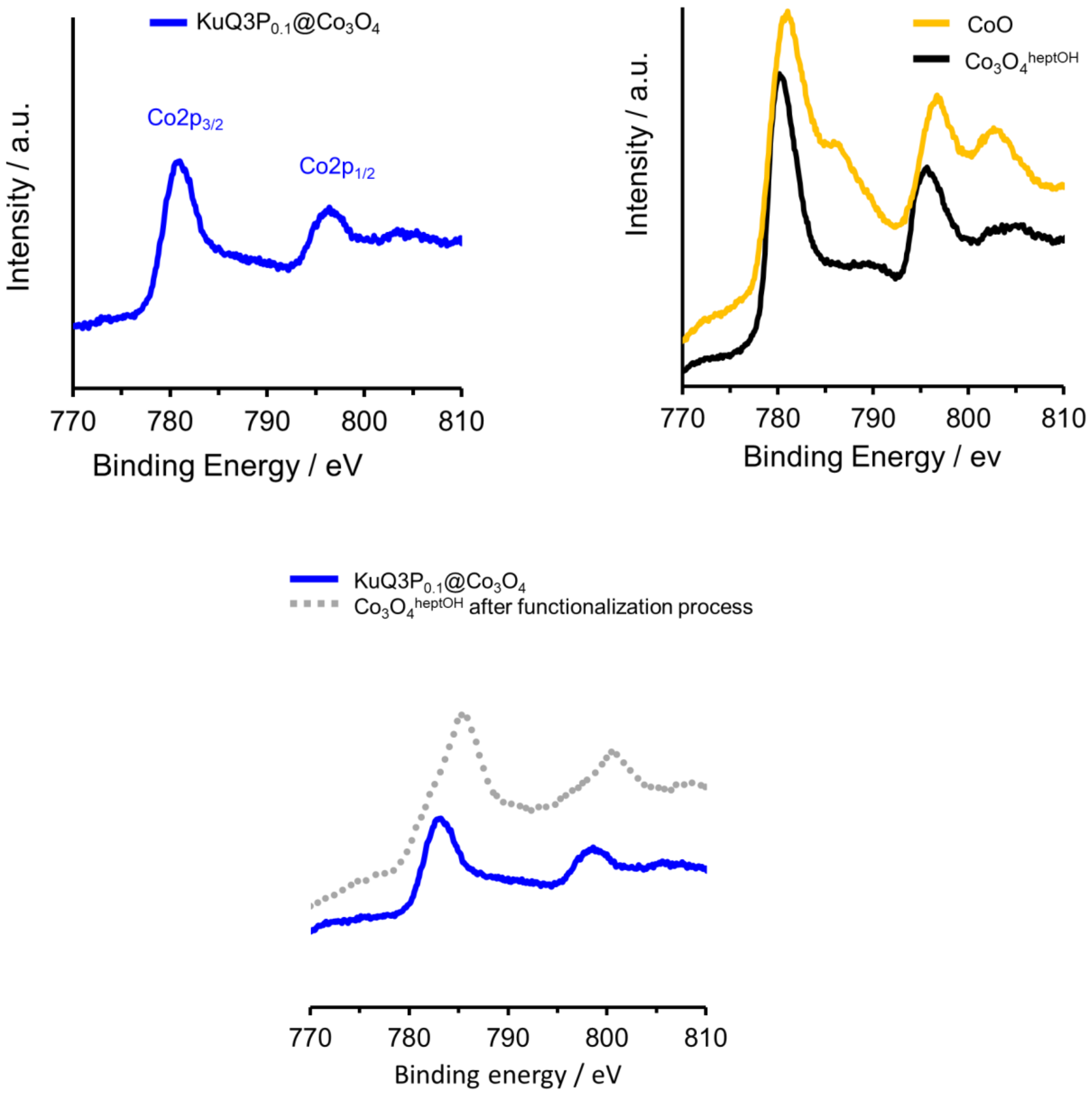

Figure S12. Co2*p* XPS data of **KuQ3P$_{0.1}$@Co$_3$O$_4$** (**top left**) and **Co$_3$O$_4$^{heptOH}** NPs (**top right**, black line; compared to a CoO reference, yellow line)**. Bottom** displays the **XPS** spectrum of **KuQ3P$_{0.1}$@Co$_3$O$_4$** (blue line) compared to that of **Co$_3$O$_4$^{heptOH}** NPs subjected to stirring in H_2O/MeOH mixture (simulating the conditions used in the functionalization process with **KuQ3P**), grey dotted line.

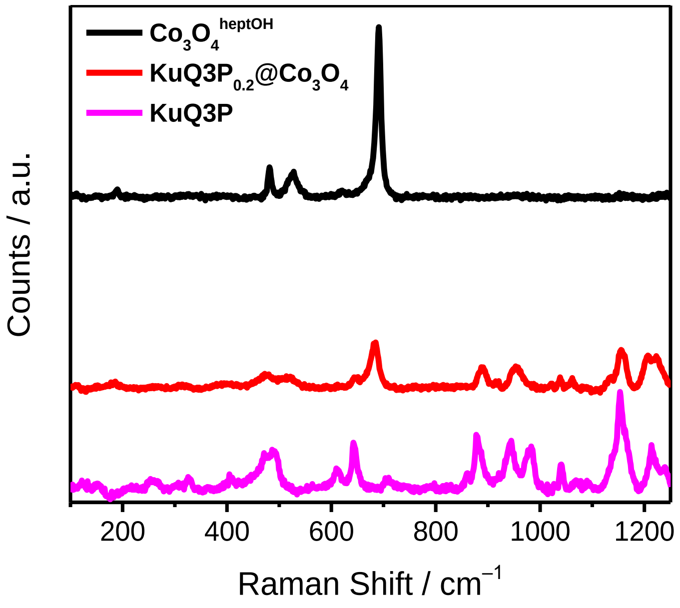

Figure S13. Resonance Raman spectrum of **$Co_3O_4^{heptOH}$** (black line), **$KuQ3P_{0.2}@Co_3O_4$** (red line) and **KuQ3P** (magenta line).

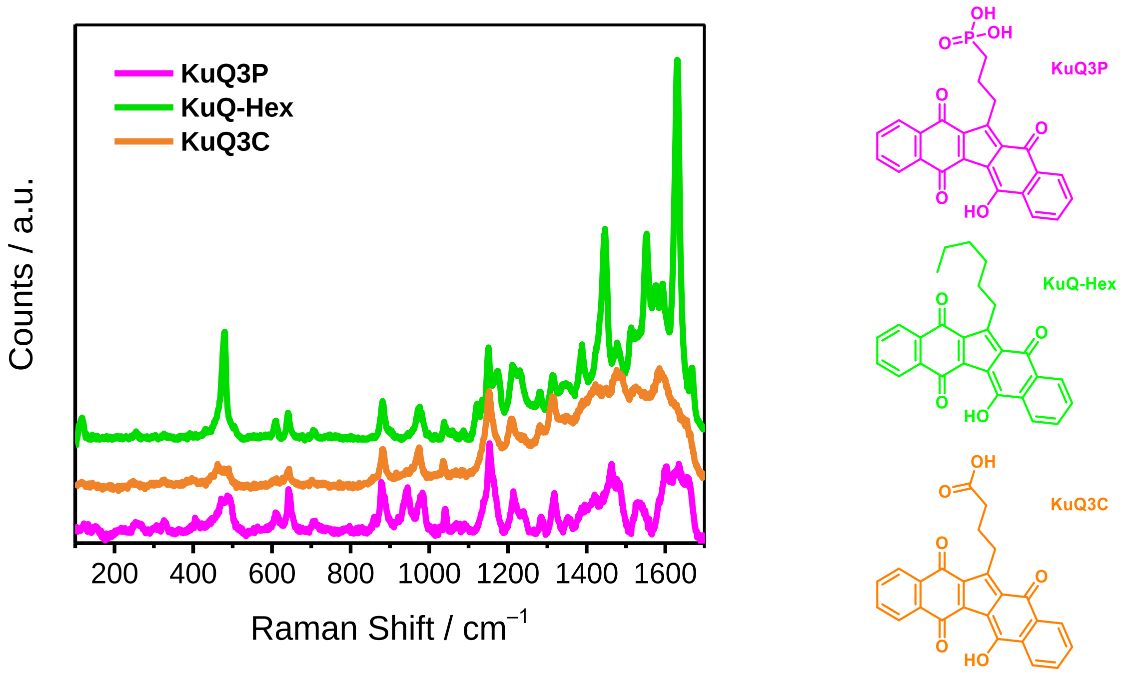

Figure S14. Left: Resonance Raman spectrum of **KuQ3P** (magenta line), **Ku-Hex** (green line) and **KuQ3C** (orange line). Right: corresponding chemical structures of the three **KuQ** dyes, with the same color code.

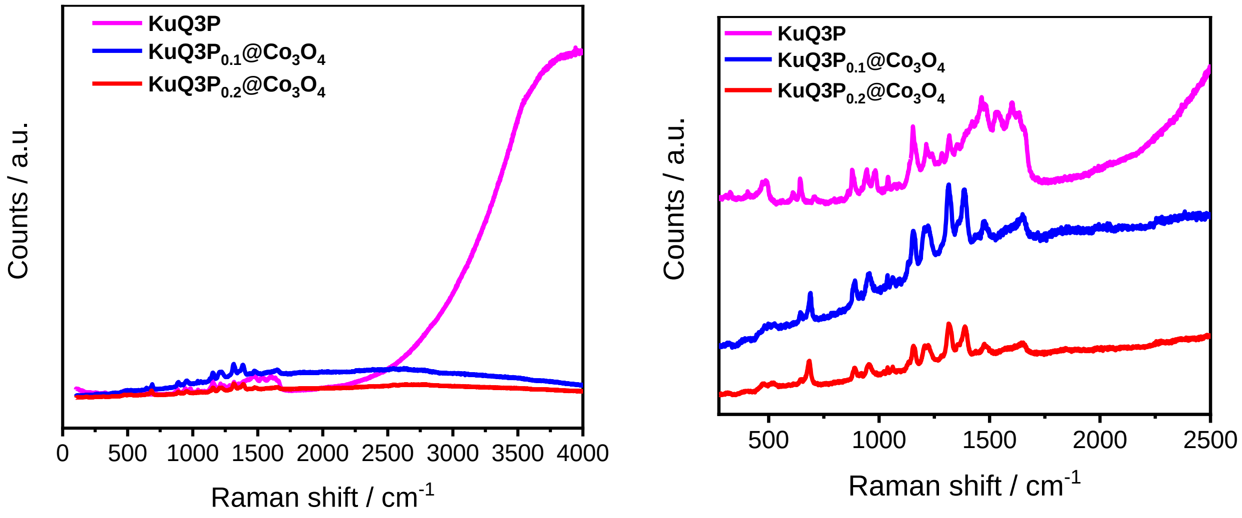

Figure S15. Resonance Raman spectrum of **KuQ3P** (magenta line), **KuQ3P$_{0.1}$@Co$_3$O$_4$** (blue line) and **KuQ3P$_{0.2}$@Co$_3$O$_4$** (red line). The **right** panel displays the full spectrum in the range 0–4000 cm^{-1}, while the **left** panel is focused on the region containing the characteristic Co$_3$O$_4$ and **KuQ3P** signals. **Note:** in the latter case, spectra have been vertically translated for the sake of clarity. In both, the onset of the **KuQ3P** fluorescence is displayed (*ca* 2000 cm^{-1}).

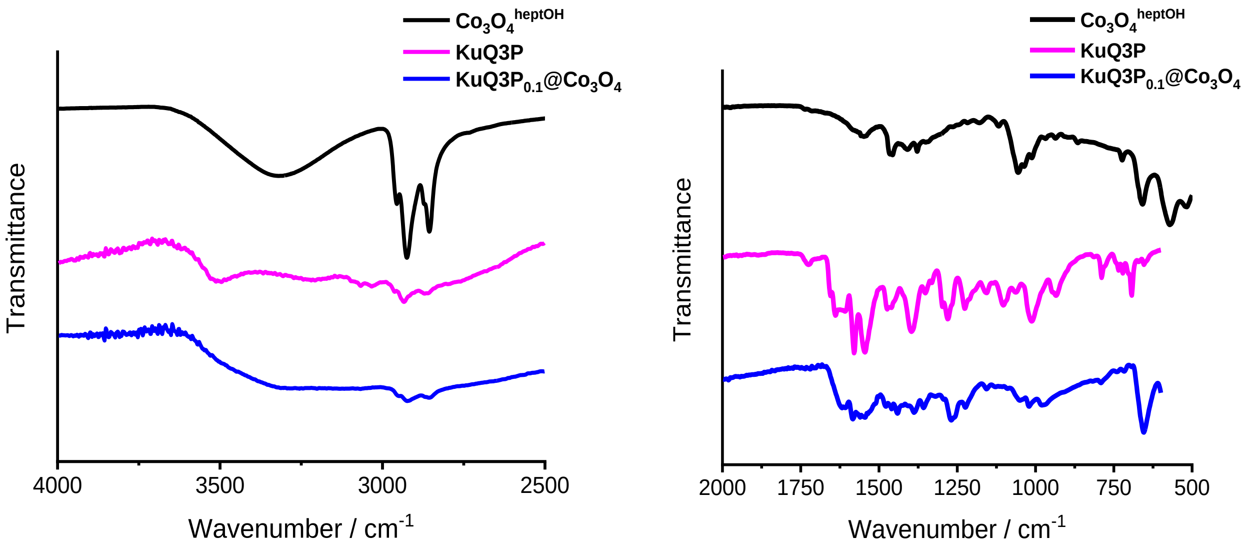

Figure S16. ATR-FTIR spectra of **Co$_3$O$_4^{heptOH}$** (black line), **KuQ3P** (magenta line) and **KuQ3P$_{0.1}$@Co$_3$O$_4$** (blue line).

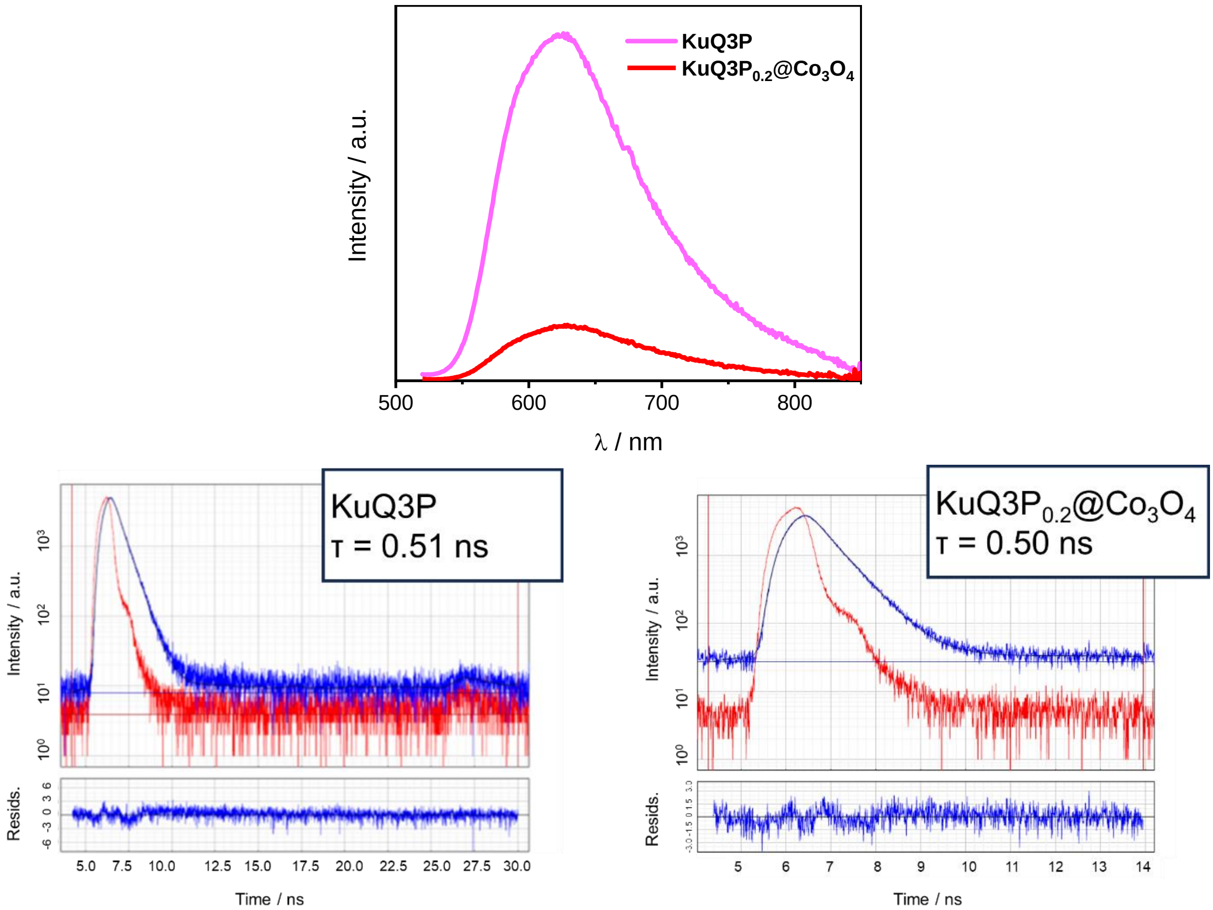

Figure S17. Top: Emission spectra of the free **KuQ3P** dye (magenta line) and **KuQ3P$_{0.2}$@Co$_3$O$_4$** (red line), registered in NaHCO$_3$/Na$_2$SiF$_6$ (pH 5.6) electrolyte. **Bottom:** Probability histograms (blue lines) obtained by TCPSC (λ_{exc} = 532 nm, λ_{em} = 610 nm) of **KuQ3P** (**left**) and **KuQ3P$_{0.2}$@Co$_3$O$_4$** (**right**) in NaHCO$_3$/Na$_2$SiF$_6$ buffer (pH 5.6) with the corresponding deconvolution and fitting (IRF is shown as red lines in both graphs). For **KuQ3P$_{0.2}$@Co$_3$O$_4$**, the lifetime found is identical (within experimental error) to the one of **KuQ3P** and is associated with residual **KuQ3P** dye in solution.

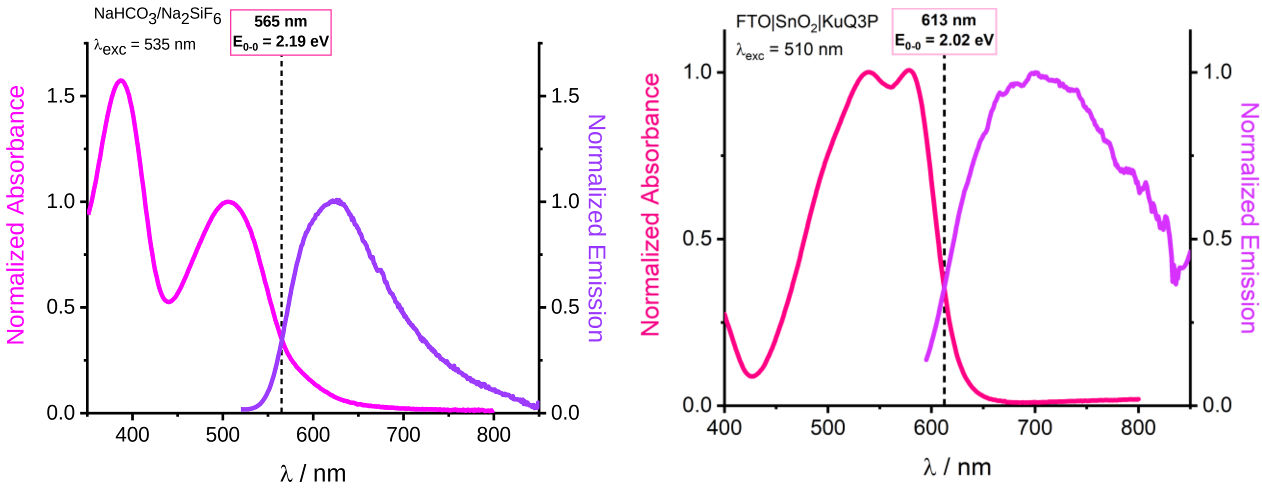

Figure S18. Left: Normalized absorption (magenta line) and emission (violet line, λ_{exc} = 532 nm) spectra of **KuQ3P** in NaHCO$_3$/Na$_2$SiF$_6$ buffer. **Right:** Normalized absorption (pink line) and emission (lavender line, λ_{exc} = 510 nm) of SnO$_2$|**KuQ3P** photoelectrodes. The crossing point, corresponding to the $E_{0–0}$ value, is indicated by the black dashed line.

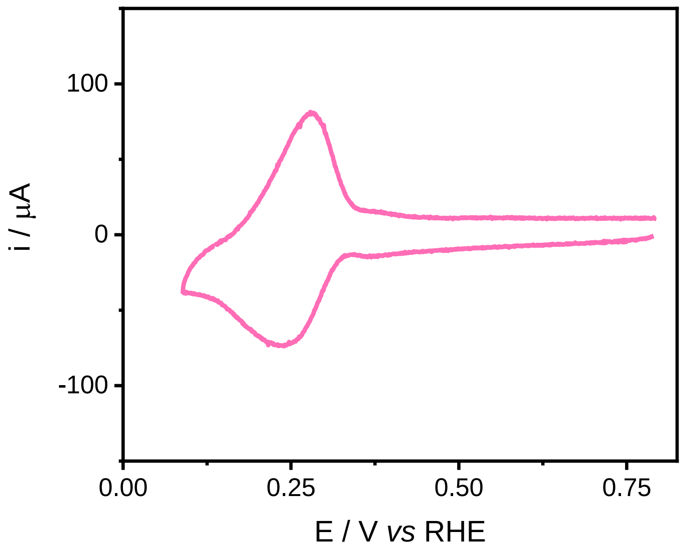

Figure S19. CV of 0.2 mM **KuQ3P** in 0.1 M NaH_2PO_4/Na_2HPO_4 (pH 5.8) solution containing 0.5 M Na_2SO_4 as supporting electrolyte, at 2.00 V·s^{-1} scan rate. Conditions: glassy carbon disk working electrode (ø 3 mm), Ag/AgCl (3 M NaCl) reference electrode, platinum rod auxiliary electrode.

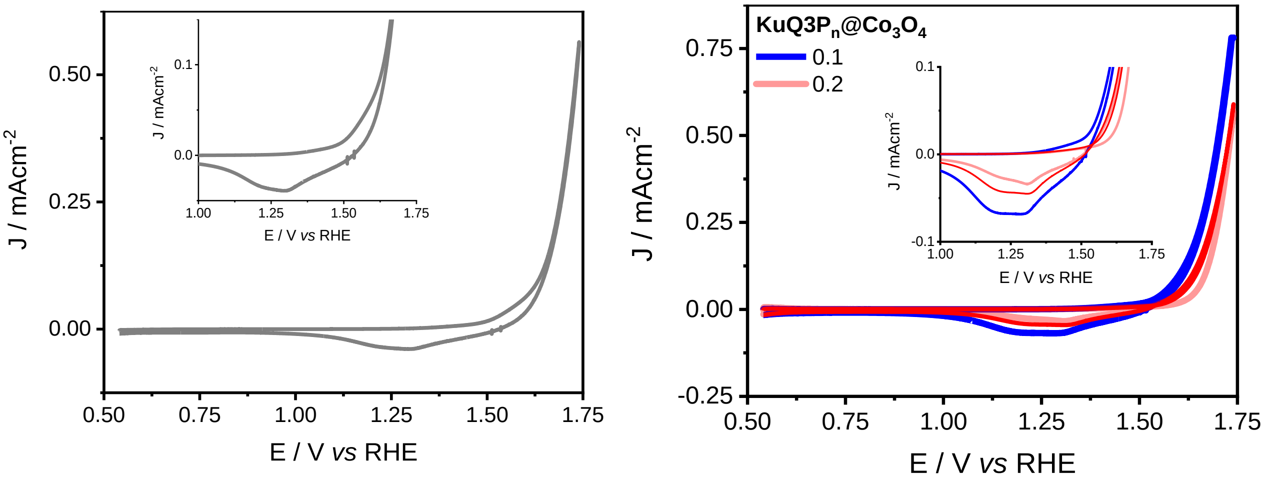

Figure S20. Left: CVs of SnO_2|**$Co_3O_4^{heptOH}$** (**left**) and SnO_2|**KuQ3P$_n$@Co_3O_4** (**right**) electrodes recorded in $NaHCO_3/Na_2SiF_6$ (pH 5.8) electrolyte at 0.020 V·s^{-1} scan rate. Ag/AgCl (3 M NaCl) reference electrode, glassy carbon disk auxiliary electrode.

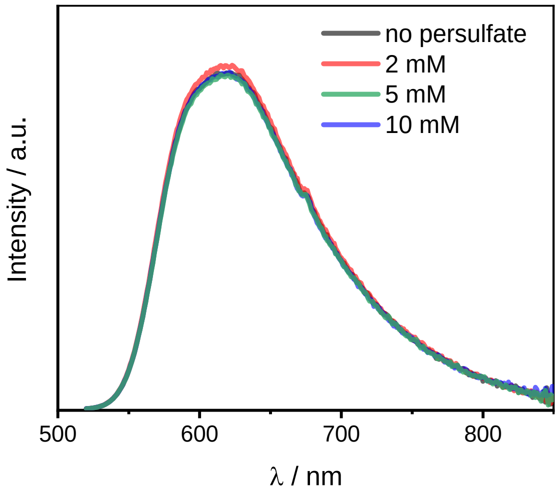

Figure S21. Fluorescence spectra of **KuQ3P** in $NaHCO_3/Na_2SiF_6$ buffer (pH 5.6) in the presence of 0–10 mM $Na_2S_2O_8$ (λ_{exc} = 532 nm). The similar profiles indicate negligible quenching of the singlet excited state by persulfate.

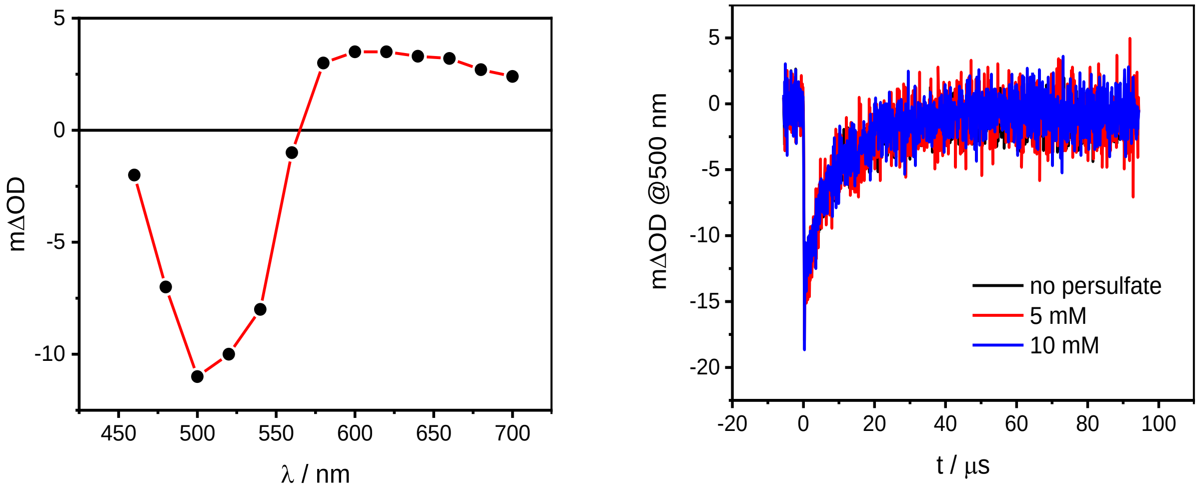

Figure S22. Left: Transient absorption spectrum of the triplet excited state of **KuQ3P** measured by laser flash photolysis (λ_{exc} = 532 nm) of **KuQ3P** in $NaHCO_3/Na_2SiF_6$ buffer (pH 5.6). **Right:** Kinetic traces in the presence of 0–10 mM $Na_2S_2O_8$. The similar decaying profiles indicate negligible quenching of the triplet excited state by persulfate.

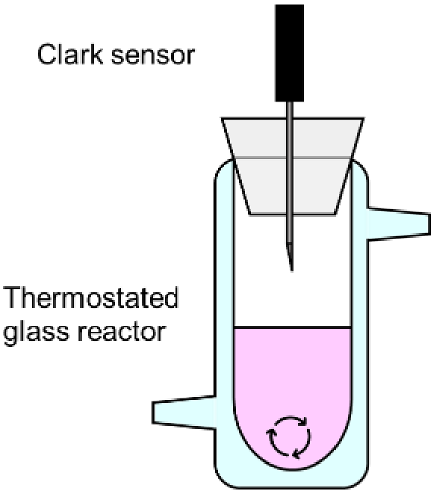

Figure S23. Schematic representation of the thermostated glass photoreactor (assembled). The Clark sensor inserted in the headspace is displayed.

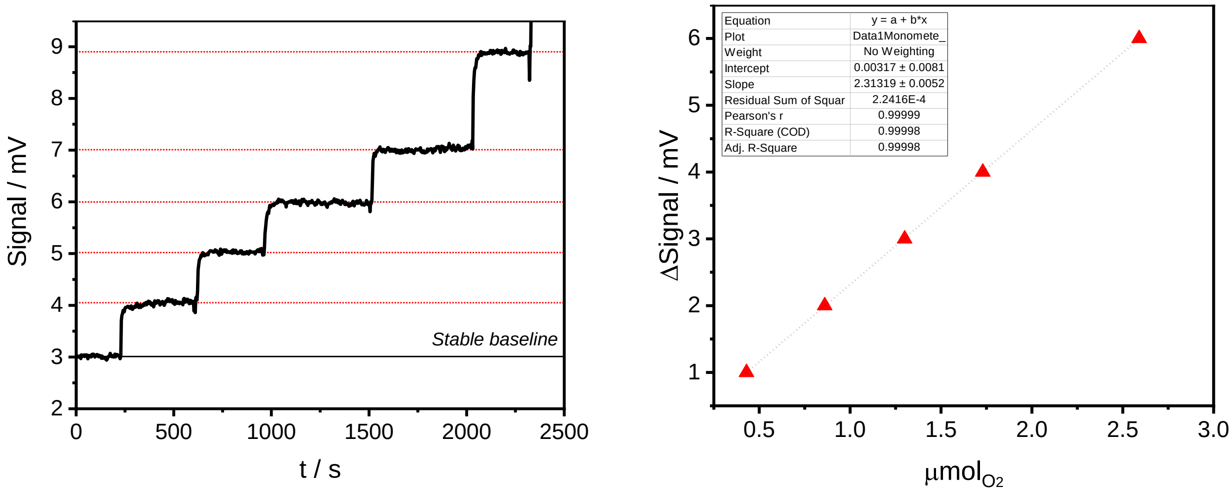

Equation	y = a + b*x
Plot	Data1Monomete_
Weight	No Weighting
Intercept	0.00317 ± 0.0081
Slope	2.31319 ± 0.0052
Residual Sum of Squar	2.2416E-4
Pearson's r	0.99999
R-Square (COD)	0.99998
Adj. R-Square	0.99998

Figure S24. Left: response of the Clark sensor upon additions of known volumes of air. **Right:** pseudo-calibration curve of the Clark sensor.

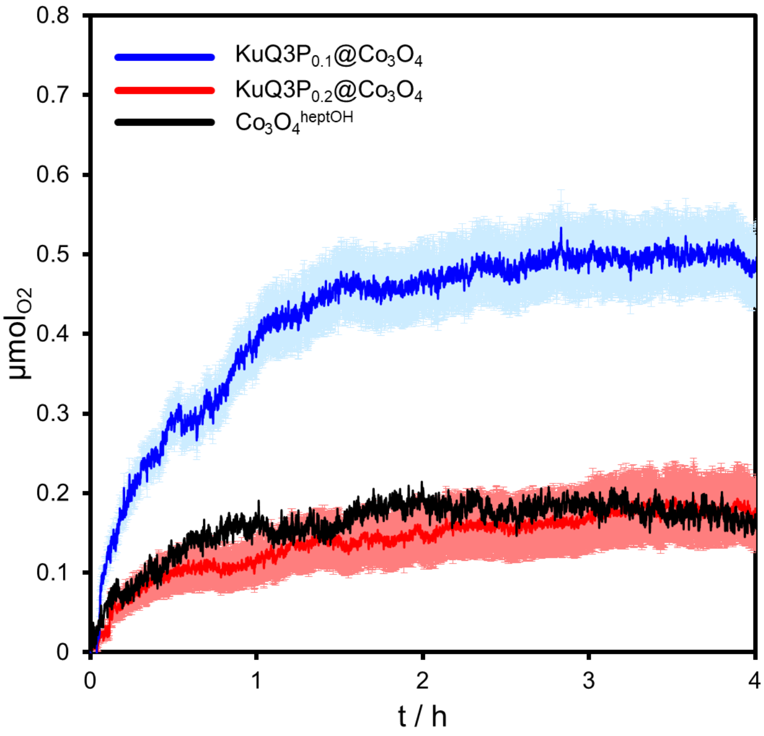

Figure S25. Oxygen detection kinetic traces for **$KuQ3P_n$@Co_3O_4** recorded under 100 mW·cm^{-2} simulated solar visible light (λ > 400 nm), in $NaHCO_3/Na_2SiF_6$ (pH 5.8) buffer.

	After catalysis		
	%Co	**%P**	**Liquid analysis (mg·L^{-1})**
$Co_3O_4^{heptOH}$			
$KuQ3P_{0.1}Co_3O_4$	43	0.17	[Co] = 21 [P] = 4.7
$KuQ3P_{0.2}Co_3O_4$	41	0.16	[Co] = 13 [P] = 4.4
0.1 eq **KuQ3P + $Co_3O_4^{heptOH}$**	28	0.09	–

Table S4. ICP analysis data relative to the different NPs before and after photoirradiation.

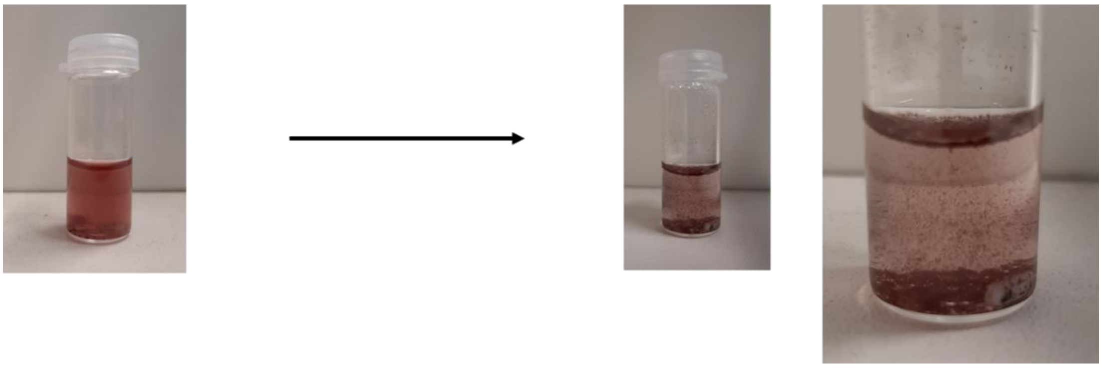

Figure S26. Pictures of a mixture of 0.925 mg of $\mathbf{Co_3O_4}^{\mathbf{heptOH}}$ NPs and 0.087 mg (0.12 eq) of **KuQ3P** in 1.50 mL $NaHCO_3/Na_2SiF_6$ (pH 5.8) buffer before and after stirring for 6 h in the dark.

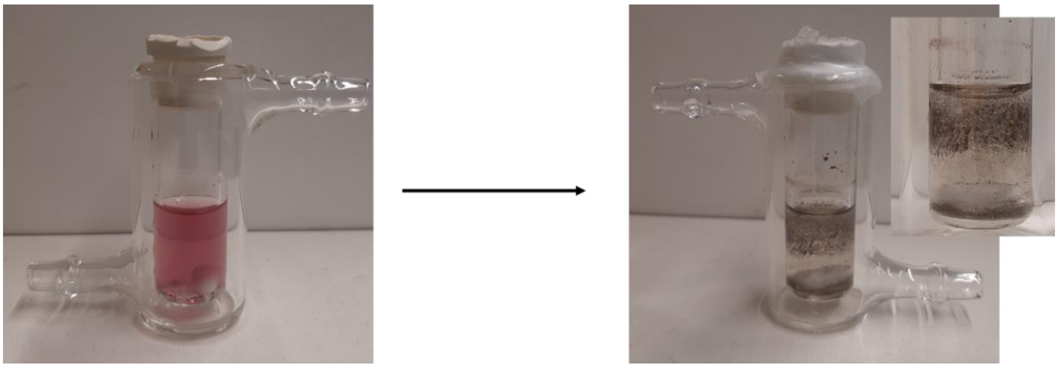

Figure S27. Pictures of a mixture of $\mathbf{Co_3O_4}^{\mathbf{heptOH}}$ NPs and 0.1 eq **KuQ3P** in $NaHCO_3/Na_2SiF_6$ (pH 5.8) buffer before and after photoirradiation with 100 mW·cm^{-2} simulated visible solar light, λ > 400 nm.

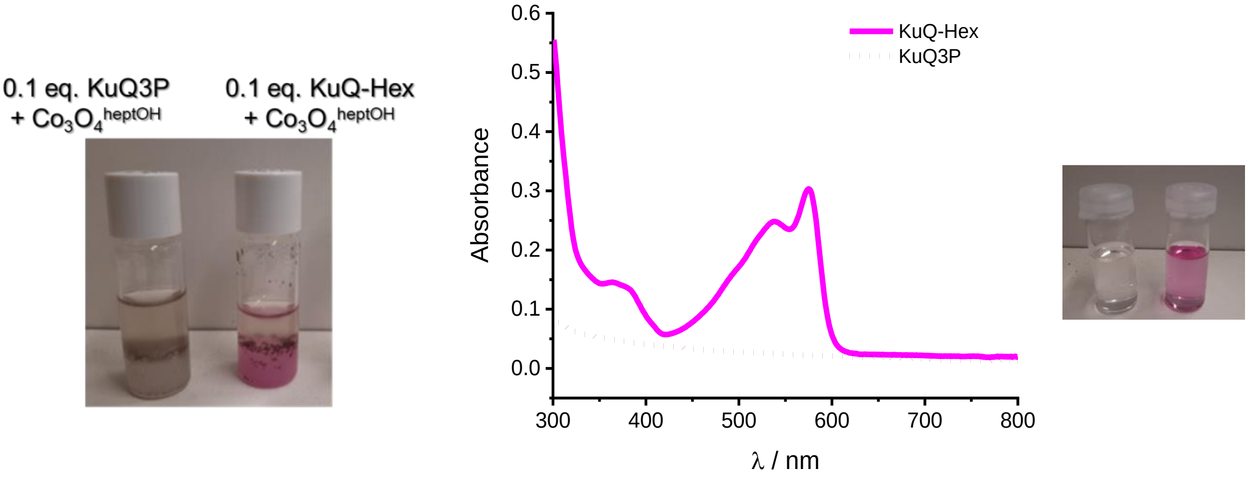

Figure S28. Left: Pictures of a mixture of $\mathbf{Co_3O_4}^{\mathbf{heptOH}}$ NPs and 0.1 eq. **KuQ3P** or 0.1 eq. **KuQ-Hex** in $NaHCO_3/Na_2SiF_6$ (pH 5.8) buffer after 5 h photoirradiation, being extracted with dichloromethane. **Right:** UV/Vis spectra of the dichloromethane extracts.

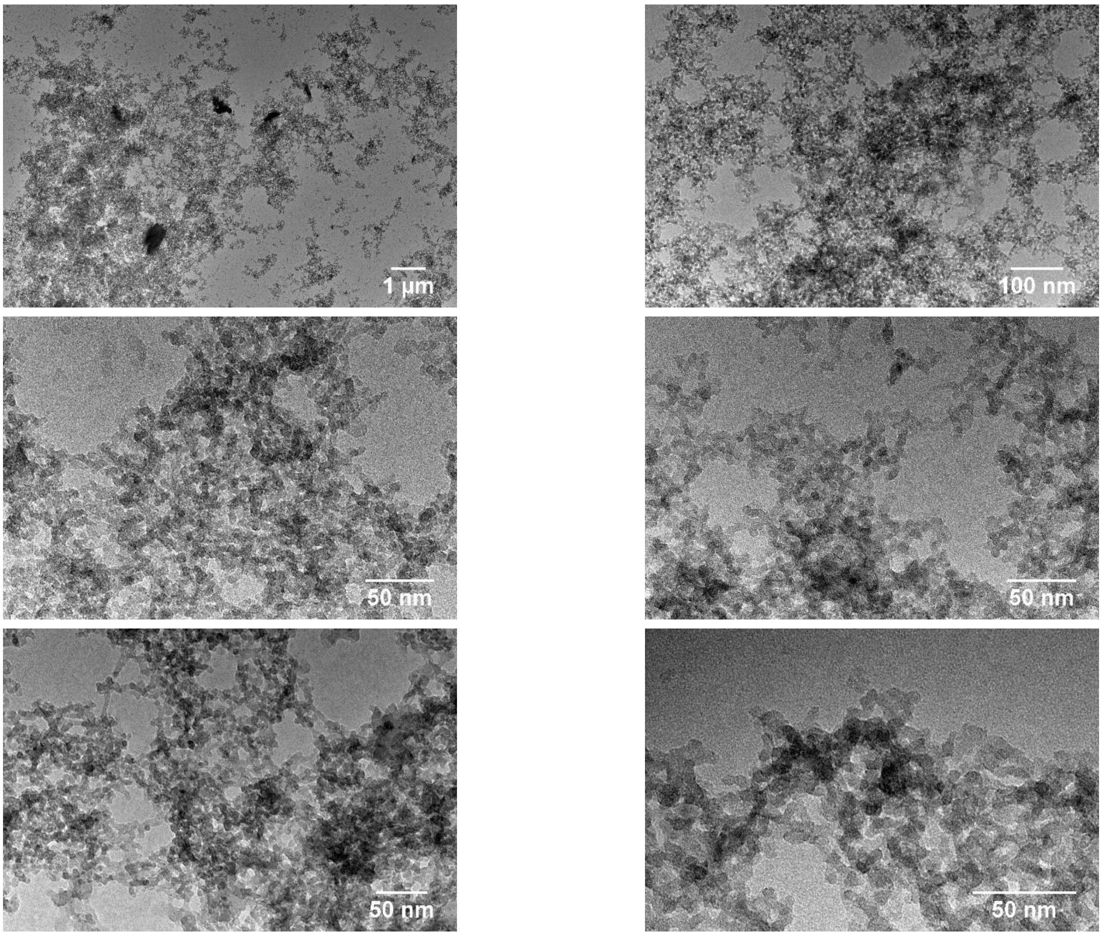

Figure S29. TEM images of **KuQ3P$_{0.1}$@Co$_3$O$_4$** NPs after 5 h photoirradiation under 100 mW·cm^{-2} simulated visible solar light (λ > 400 nm) in NaHCO$_3$/Na$_2$SiF$_6$ (pH 5.8) buffer.

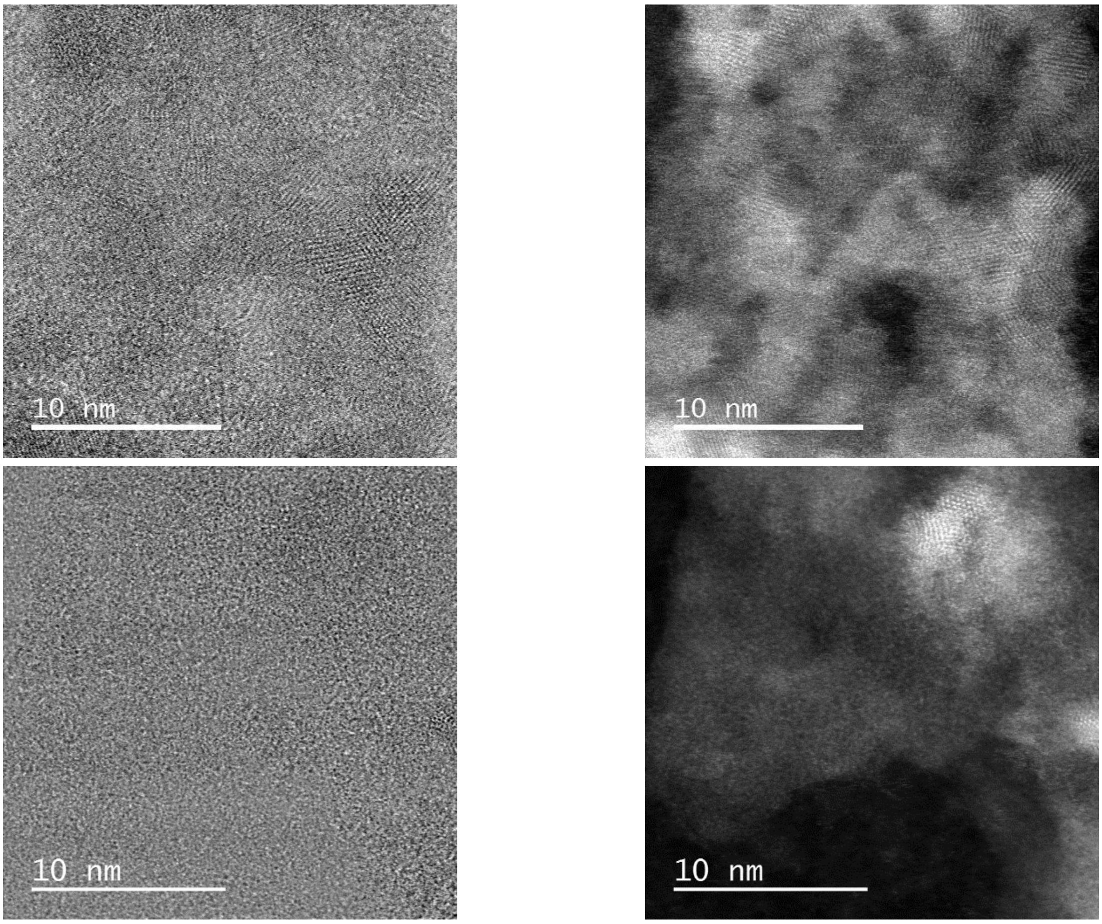

Figure S30. STEM-HAADF images of **KuQ3P$_{0.1}$@Co$_3$O$_4$** NPs after 5 h photoirradiation under 100 mW·cm^{-2} simulated visible solar light, λ > 400 nm.

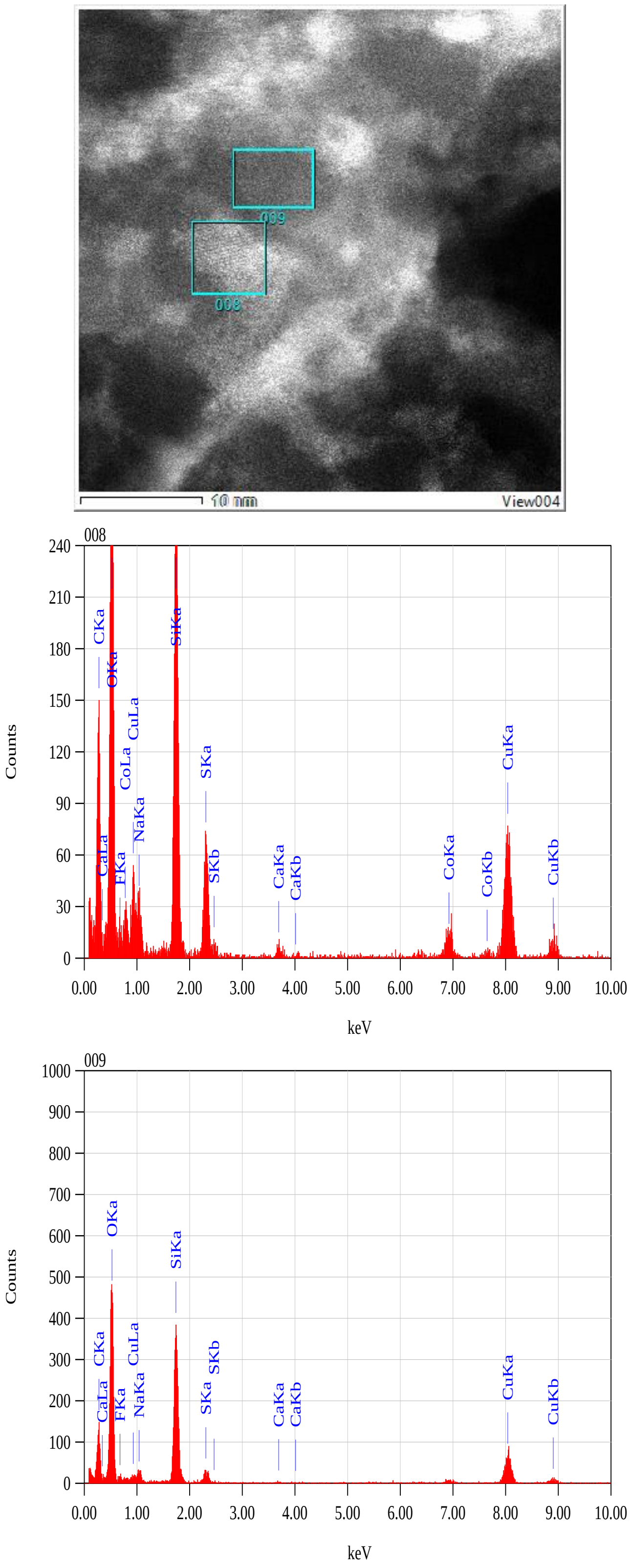

Figure S31. EDX analysis of **KuQ3P$_{0.1}$@Co$_3$O$_4$** NPs after 5 h photoirradiation under 100 mW·cm^{-2} simulated visible solar light, λ > 400 nm.

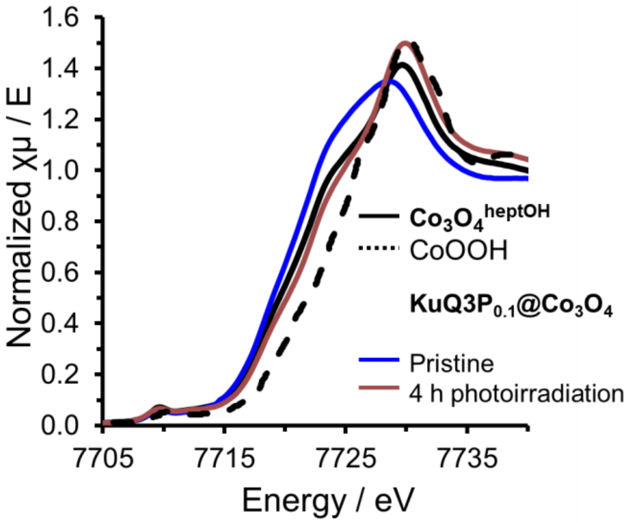

Figure S32. Normalized Co K-edge XANES spectra of **$Co_3O_4^{heptOH}$** (black full line), **$KuQ3P_{0.1}@Co_3O_4$** (blue line), **$KuQ3P_{0.1}@Co_3O_4$** after 270 minutes of photoirradiation with 100 mW·cm^{-2} simulated visible solar light (λ > 400 nm) (brown line) and a CoO(OH) reference (black dashed line). **Note:** CoO(OH) reference has been digitalized from reference [33].

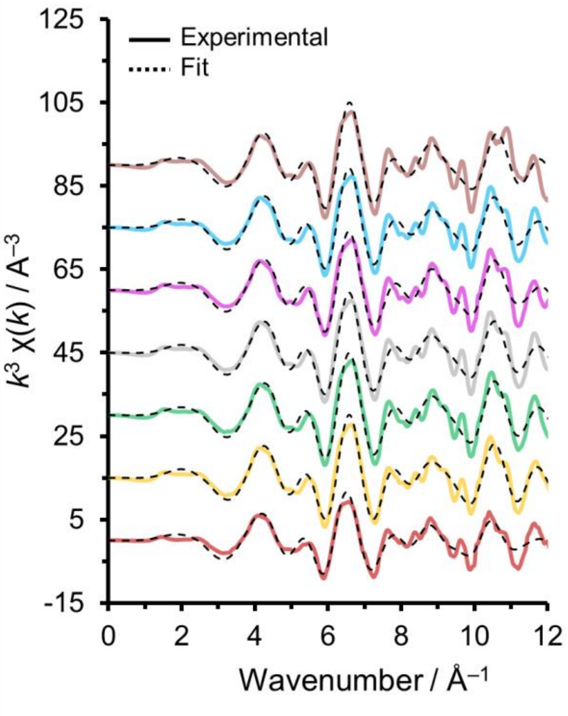

Figure S33. Evolution of k^3-weighted Co EXAFS of **$KuQ3P_{0.1}@Co_3O_4$** during photoirradiation (100 mW·cm^{-2} simulated visible solar light, λ > 400 nm). Experimental data are represented as solid lines and fitted data as dashed lines. Experimental spectra were fitted for over a k-range 3–11 Å^{-1}. Color code: **$Co_3O_4^{heptOH}$** (wine), **$KuQ3P_{0.1}@Co_3O_4$** after irradiation sustained for 15 seconds (yellow), 5 minutes (green), 15 minutes (gray), 45 minutes (magenta), 90 minutes (cyan), 270 minutes (brown).

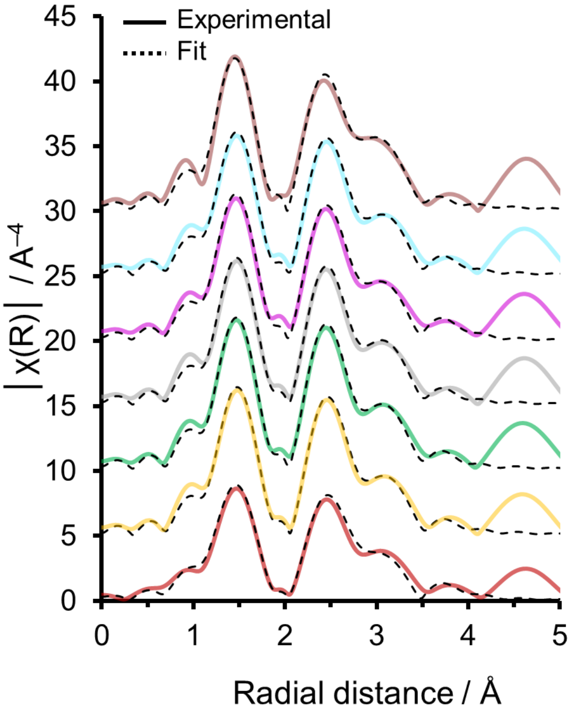

Figure S34. Evolution of the Fourier transforms for k^3-weighted Co EXAFS of **KuQ3P$_{0.1}$@Co$_3$O$_4$** NPs during photoirradiation (100 mW·cm^{-2} simulated visible solar light, λ > 400 nm). Experimental data are represented as solid lines and fitted data as dashed lines. Experimental spectra were fitted for over a k-range 3–11 Å^{-1}. Color code: **Co$_3$O$_4$^{heptOH}** (wine), **KuQ3P$_{0.1}$@Co$_3$O$_4$** after irradiation sustained for 15 seconds (yellow), 5 minutes (green), 15 minutes (gray), 45 minutes (magenta), 90 minutes (cyan), 270 minutes (brown).

Sample	**Region**	**Shell, N**	**R, Å**	**σ^2 (10^{-3} Å^2)**	**S_0^2**	**E_0, eV**	**R-factor**	**Reduced χ^2**
$Co_3O_4^{heptOH}$	k = 3 – 11 Å^{-1}	Co-O, 5.3	1.92	6.1	0.9	-4.4	0.023	101
Co K-edge	R = 1 – 4.2 Å	Co-Co, 4	2.86	7.9				
		Co-Co, 8	3.36	12.4				
		Co-O, 3.2	4.31	1.8				
$KuQ3P_{0.1}@Co_3O_4$	k = 3 – 11 Å^{-1}	Co-O, 5.3	1.90	4.9	0.4	-4.7	0.119	303
Co K-Edge	R = 1 – 4.2 Å	Co-Co, 4	2.83	9.8				
		Co-Co, 8	3.36	12.1				
		Co-O, 3.2	3.98	3.1				
$KuQ3P_{0.1}@Co_3O_4$ After irradiation (t = 15 s)	k = 3 – 11 Å^{-1}	Co-O, 5.3	1.91	4	0.9	-1.7	0.013	190
Co K-Edge	R = 1 – 4.2 Å	Co-Co, 4	2.84	5				
		Co-Co, 8	3.36	9				
		Co-O, 3.2	4.23	13				
$KuQ3P_{0.1}@Co_3O_4$ After irradiation (t = 5 min)	k = 3 – 11 Å^{-1}	Co-O, 5.3	1.91	4	0.9	-2.3	0.007	170
Co K-Edge	R = 1 – 4.2 Å	Co-Co, 4	2.84	5				
		Co-Co, 8	3.35	9				
		Co-O, 3.2	4.31	4				
$KuQ3P_{0.1}@Co_3O_4$ After irradiation (t = 15 min)	k = 3 – 11 Å^{-1}	Co-O, 5.3	1.91	4	0.9	-2.2	0.008	274
Co K-Edge	R = 1 – 4.2 Å	Co-Co, 4	2.84	6				
		Co-Co, 8	3.36	10				
		Co-O, 3.2	4.30	5				
$KuQ3P_{0.1}@Co_3O_4$ After irradiation (t = 45 min)	k = 3 – 11 Å^{-1}	Co-O, 5.3	1.90	4	0.9	-3.2	0.014	142
Co K-Edge	R = 1 – 4.2 Å	Co-Co, 4	2.84	6				
		Co-Co, 8	3.34	10				
		Co-O, 3.2	4.30	1				
$KuQ3P_{0.1}@Co_3O_4$ After irradiation (t = 90 min)	k = 3 – 11 Å^{-1}	Co-O, 5.3	1.91	4	0.9	-2.0	0.011	430
Co K-Edge	R = 1 – 4.2 Å	Co-Co, 4	2.84	6				
		Co-Co, 8	3.35	10				
		Co-O, 3.2	4.30	3				
$KuQ3P_{0.1}@Co_3O_4$ After irradiation (t =270 min)	k = 3 – 11 Å^{-1}	Co-O, 5.3	1.89	4	0.9	-3.7	0.012	431
Co K-Edge	R = 1 – 4.2 Å	Co-Co, 4	2.83	6				
		Co-Co, 8	3.34	9				
		Co-O, 3.2	4.26	10				

Table S5. EXAFS fitting parameters for **$Co_3O_4^{heptOH}$** NPs and **$KuQ3P_{0.1}@Co_3O_4$** NPs before and after photoirradiation (100 mW·cm^{-2} simulated visible solar light, λ > 400 nm) at different times.

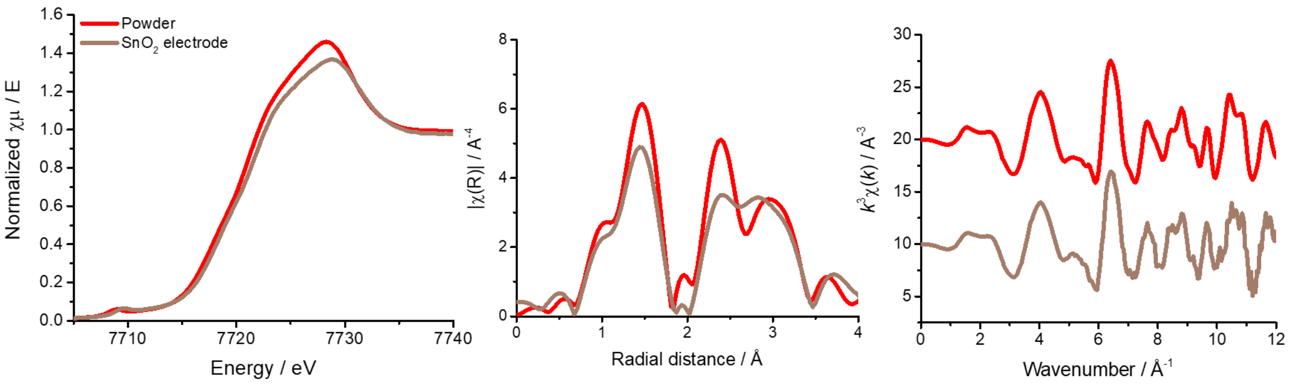

Figure S35. Left: Normalized Co K-edge spectra of **KuQ3P$_{0.2}$@Co$_3$O$_4$** NPs before (red line) and after (brown line) deposition on SnO$_2$ films. **Middle:** Fourier transforms of the k^3-weighted Co EXAFS spectra for the same samples. **Right:** Corresponding k^3-weighted Co EXAFS spectra.

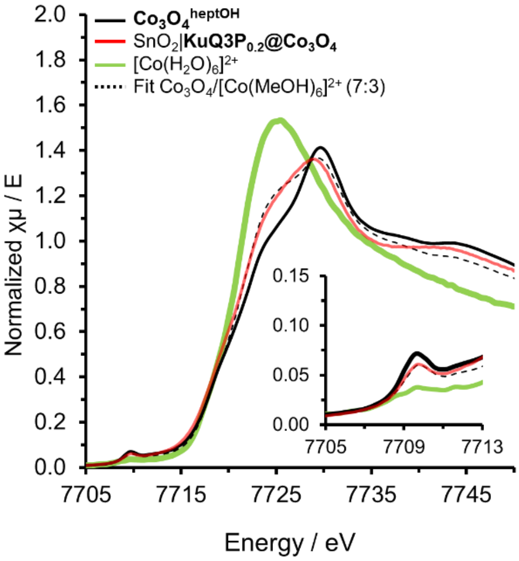

Figure S36. Normalized Co K-edge spectra of **Co$_3$O$_4$$^{\text{heptOH}}$** NPs (black full line), **KuQ3P$_{0.2}$@Co$_3$O$_4$** NPs after deposition on SnO$_2$ films (red line) and [Co(H$_2$O)$_6$]$^{2+}$ (green line), along with the fitting with a mixture of **Co$_3$O$_4$$^{\text{heptOH}}$** and [Co(MeOH)$_6$]$^{2+}$ as a purely octahedrally coordinated model in a 7:3 ratio (black dashed line). **Inset:** Pre-edge region of normalized Co K-edge spectra of the same samples.

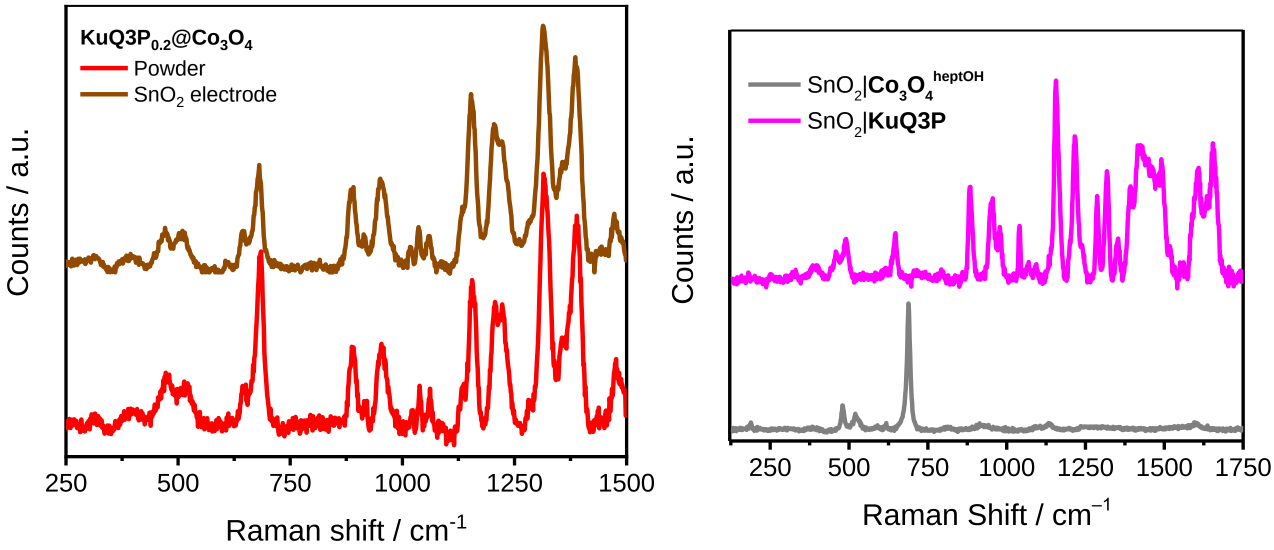

Figure S37. Left: Resonance Raman spectrum of **KuQ3P$_{0.2}$@Co$_3$O$_4$** NPs before (red line) and after (brown line) deposition on SnO$_2$ films. **Note:** The spectrum of the powder sample has been magnified (× 5) for the sake of comparison. **Right:** Resonance Raman spectra of **Co$_3$O$_4$^{heptOH}** NPs deposited on SnO$_2$ films (grey line) and of **KuQ3P** dye anchored to SnO$_2$ as described in **Section 11** (magenta line).

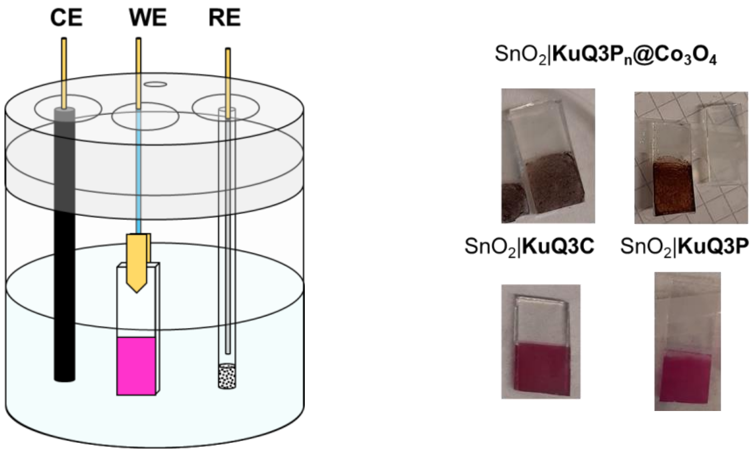

Figure S38. Left: Schematic view of the one-compartment photoelectrochemical cell used for testing the photoelectrodes. **Right:** Pictures exemplifying the SnO$_2$ photoanodes studied in the work.

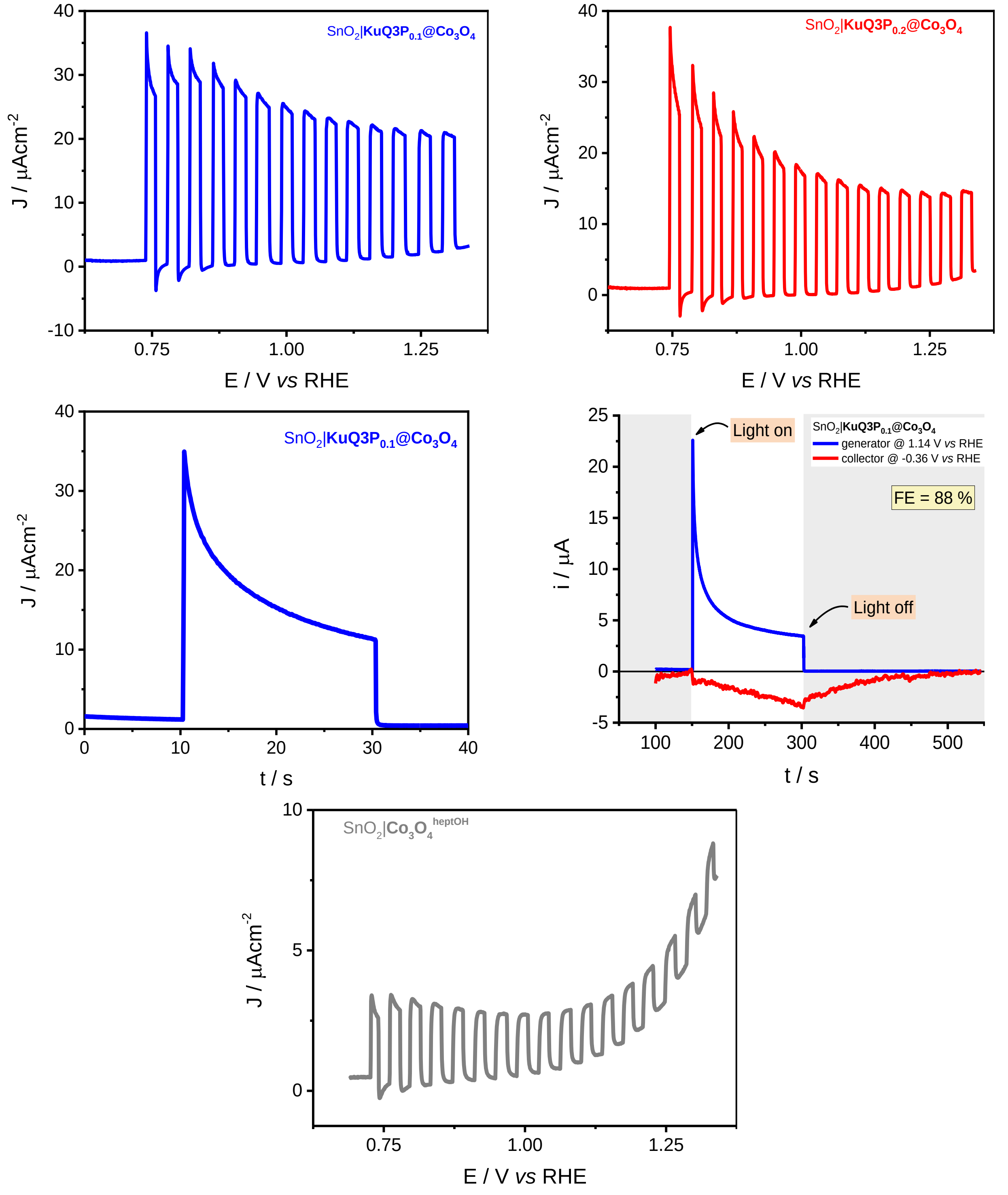

Figure S39. Top: LSV traces under intermittent illumination (100 mW·cm^{-2} simulated visible solar light, λ > 400 nm) of the hybrid nanomaterials on FTO|SnO_2 photoelectrodes. **KuQ3P$_{0.1}$@Co_3O_4** NPs (**left**, blue line); **KuQ3P$_{0.2}$@Co_3O_4** NPs (**right**, red line). Both were registered at a scan rate of 0.020 V·s^{-1}. **Middle:** CA of **KuQ3P$_{0.1}$@Co_3O_4** registered at 1.14 V *vs* RHE under illumination (**left**). CA recorded in a two-plate generator-collector setup to detect O_2 evolved by **KuQ3P$_{0.1}$@Co_3O_4** NPs (**left**). The generator was poised at 1.14 V *vs* RHE and illuminated; the collector was poised at –0.36 V *vs* RHE. **Bottom:** Control LSV trace of unsensitized FTO|SnO_2|**$Co_3O_4^{heptOH}$** under intermittent illumination (100 mW·cm^{-2} simulated visible solar light, λ > 400 nm) registered at a scan rate of 0.020 V·s^{-1}.
All photoelectrochemical experiments were performed in $NaHCO_3$/Na_2SiF_6 (pH 5.8) electrolyte, using simulated visible solar light (100 mW·cm^{-2}, λ > 400 nm).

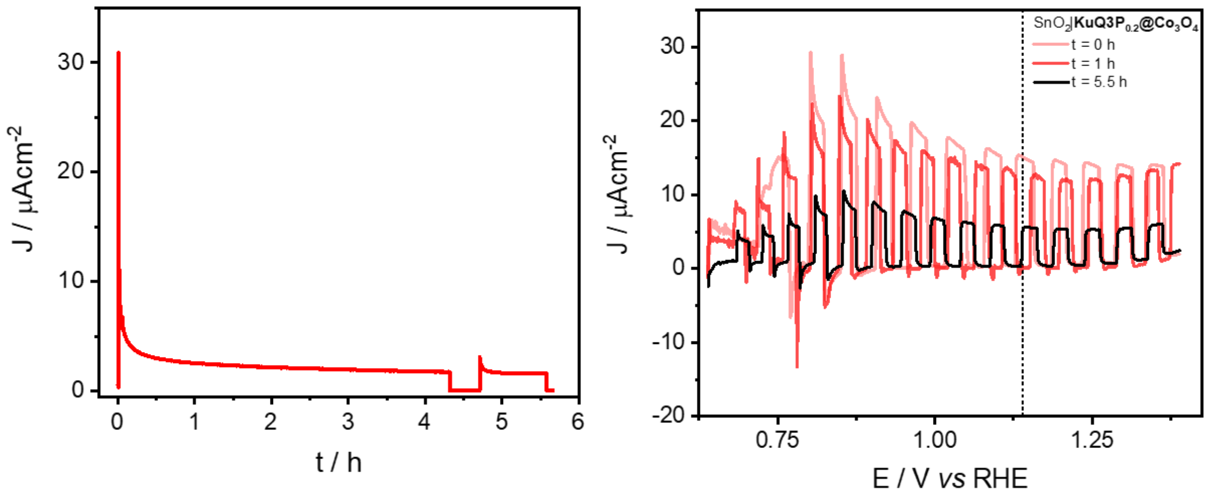

Figure S40. Left: Sustained (5.5 h) CA of SnO$_2$|**KuQ3P$_{0.2}$@Co$_3$O$_4$** registered at 1.14 V *vs* RHE. **Right:** LSV traces under chopped illumination, registered to monitor the system during photoelectrolysis (on the pristine sample, after 1 h, and after 6 h), recorded at 0.020 V·s^{-1}. The value 1.14 V *vs* RHE (potential applied in the CA) is marked by the dashed line. Photoelectrochemical measurements were performed in NaHCO$_3$/Na$_2$SiF$_6$ (pH 5.8) electrolyte, using simulated visible solar light (100 mW·cm^{-2}, λ > 400 nm).

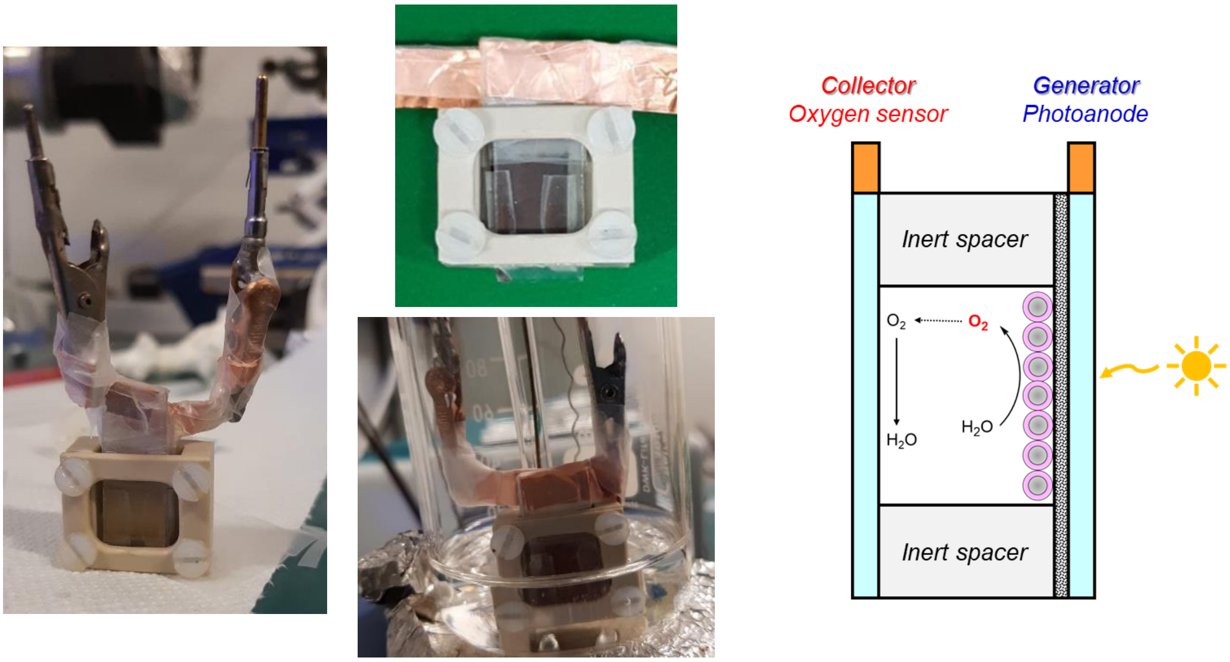

Figure S41. Pictures displaying of the setup used for two-plate generator-collector experiments (**left and middle**) and its schematic operation principle (**right**). The **top middle** figure displays the H-shaped mask between the electrodes clamped together in the PEEK frame.

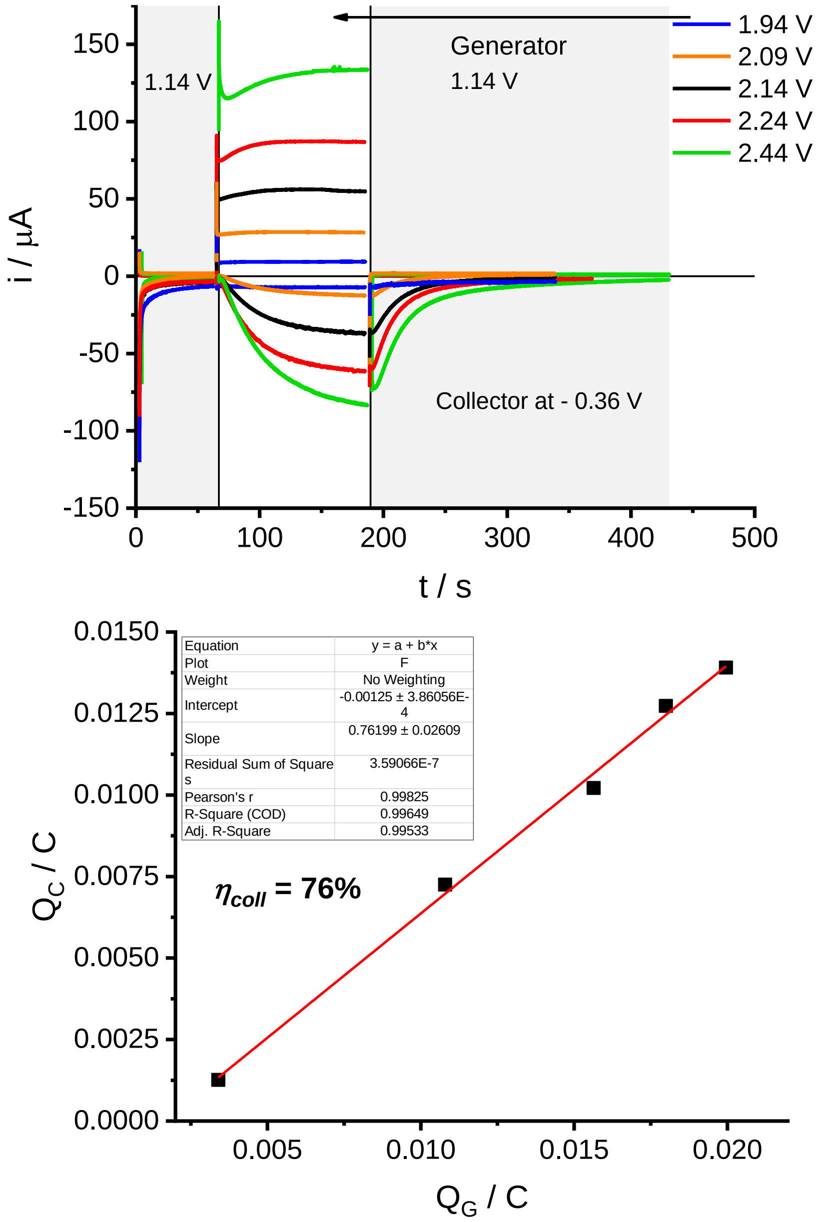

Figure S42. Calibration of the generator-collector setup with FTO generator and FTO collector (poised at –0.36 V *vs* RHE) electrodes, registered in $NaHCO_3$/Na_2SiF_6 (pH 5.8) electrolyte. **Top:** chronoamperograms. **Bottom:** calibration curve obtained upon integration of the generator and collector current traces, providing the collection efficiency.

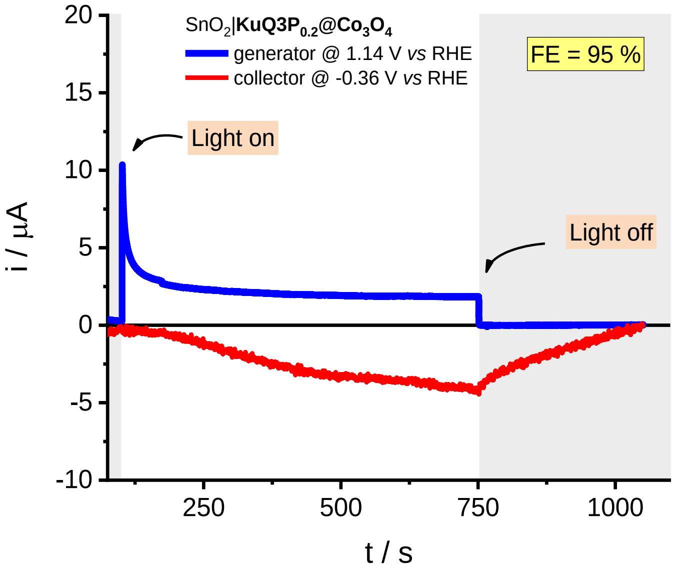

Figure S43. Chronoamperograms recorded in a two-plate generator-collector setup to detect evolved O_2 for **KuQ3P$_{0.2}$@Co$_3$O$_4$** NPs in a longer term (650 s) illumination experiment. The generator was poised at 1.14 V *vs* RHE and illuminated with simulated visible solar light (100 mW·cm^{-2}, λ > 400 nm), the collector was poised at –0.36 V *vs* RHE, registered in $NaHCO_3$/Na_2SiF_6 (pH 5.8) electrolyte.

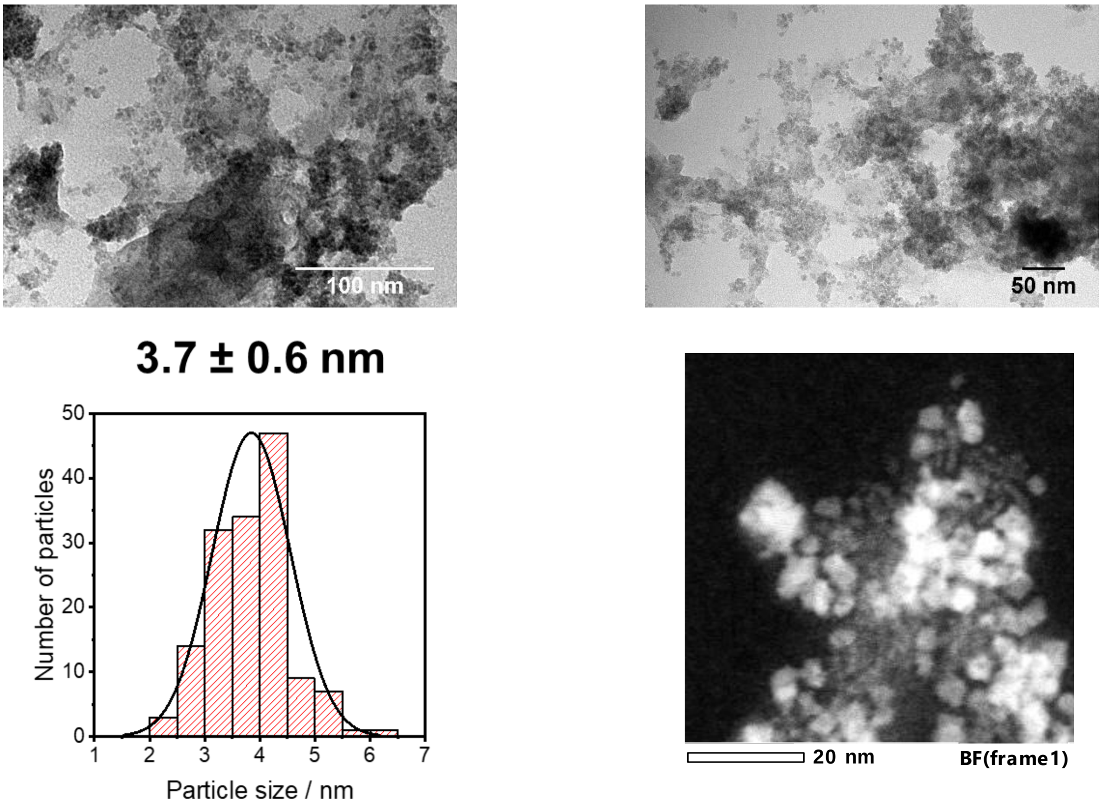

Figure S44. HR-TEM images (**top**), size distribution histogram (**bottom left**) and STEM-HAADF image (**bottom right**) of **KuQ3C$_{0.1}$@Co$_3$O$_4$** NPs.

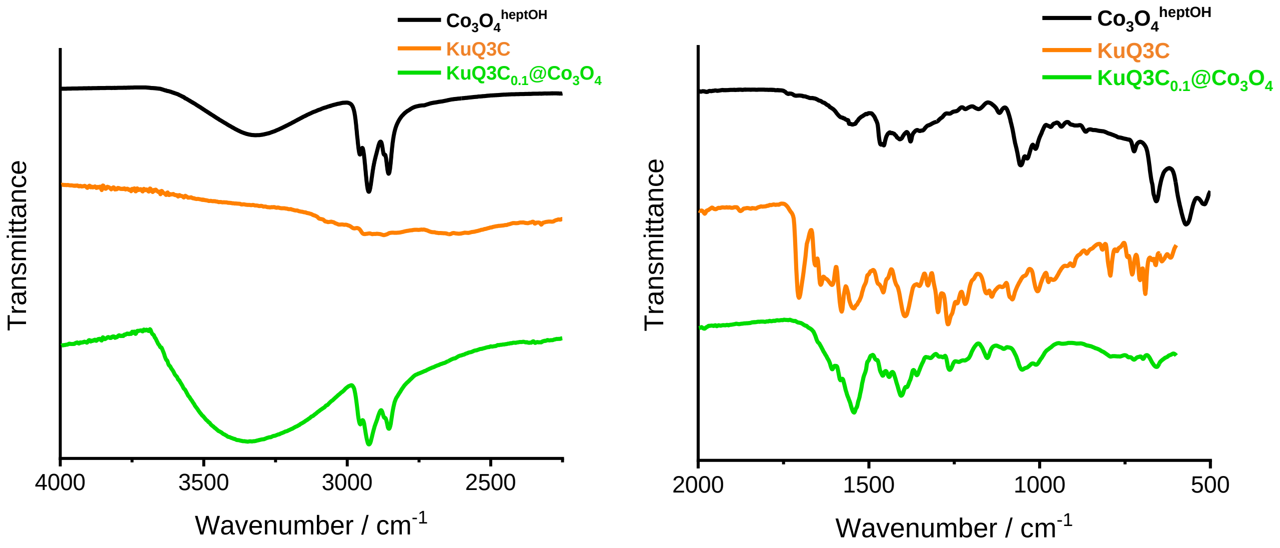

Figure S45. ATR-FTIR spectra of **$Co_3O_4^{heptOH}$** NPs (black line), **KuQ3C** (orange line) and **$KuQ3C_{0.1}@Co_3O_4$** NPs (green line). Spectra were recorded on powder samples. **Note:** The disappearance of the carboxylic acid C=O stretching vibration of free **KuQ3C** is observed in **$KuQ3C_{0.1}@Co_3O_4$**, coherent with coordination of **KuQ3C** to Co_3O_4 NPs**.** Additionally, the separation between the symmetric ($\nu_s(COO^-)$ = 1406 cm^{-1}) and asymmetric ($\nu_{as}(COO^-)$ = 1543 cm^{-1}) stretching signals for the carboxylate group ($\Delta\nu(COO^-)$ = 137 cm^{-1}) are suggestive of a bridging bidentate coordination mode of the anchoring group, bound to two different cobalt sites (see Reference [34]). However, the persistence of the intense signals ascribed to heptOH suggests that quantitative ligand substitution has not occurred during the synthesis of **$KuQ3C_{0.1}@Co_3O_4$**, possibly due to the lower stability of the carboxylate-Co bond with respect to the phosphonate-Co one.

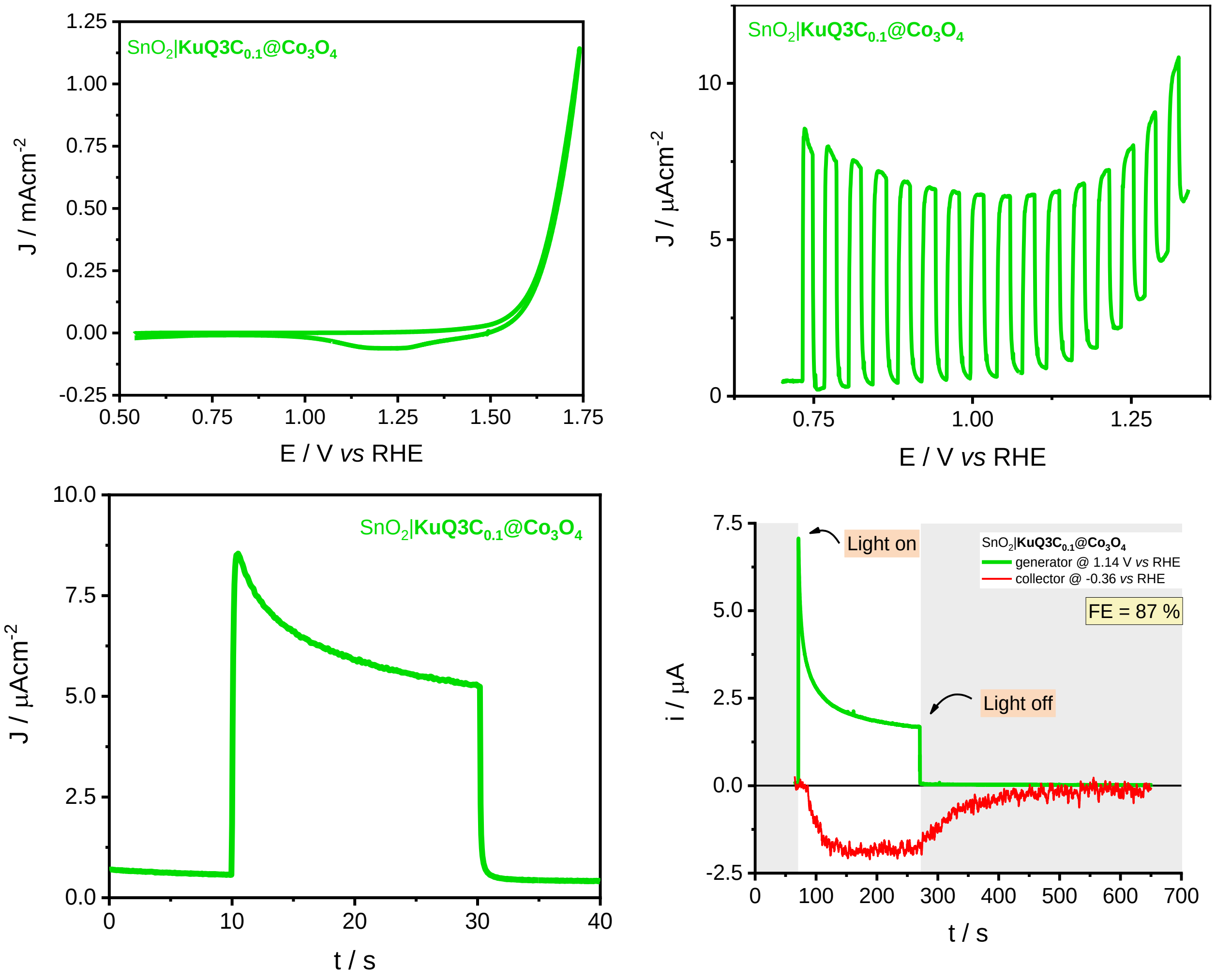

Figure S46. Top: CV of SnO_2|**KuQ3C$_{0.1}$@Co_3O_4** electrodes in the dark (**left**) and LSV under chopped illumination (**right**), recorded at 0.020 V·s^{-1} scan rate. **Bottom left:** CA of **KuQ3C$_{0.1}$@Co_3O_4** NPs registered at 1.14 V *vs* RHE. **Bottom right:** CA recorded in a two-plate generator-collector setup to detect O_2 evolved by **KuQ3C$_{0.1}$@Co_3O_4** NPs. The generator was poised at 1.14 V *vs* RHE and illuminated; the collector was poised at –0.36 V *vs* RHE. All experiments were performed using a Ag/AgCl (3 M NaCl) reference electrode and a glassy carbon disk auxiliary electrode, in $NaHCO_3/Na_2SiF_6$ (pH 5.8) electrolyte. Illumination was performed using simulated visible solar light (100 mW·cm^{-2}, λ > 400 nm).

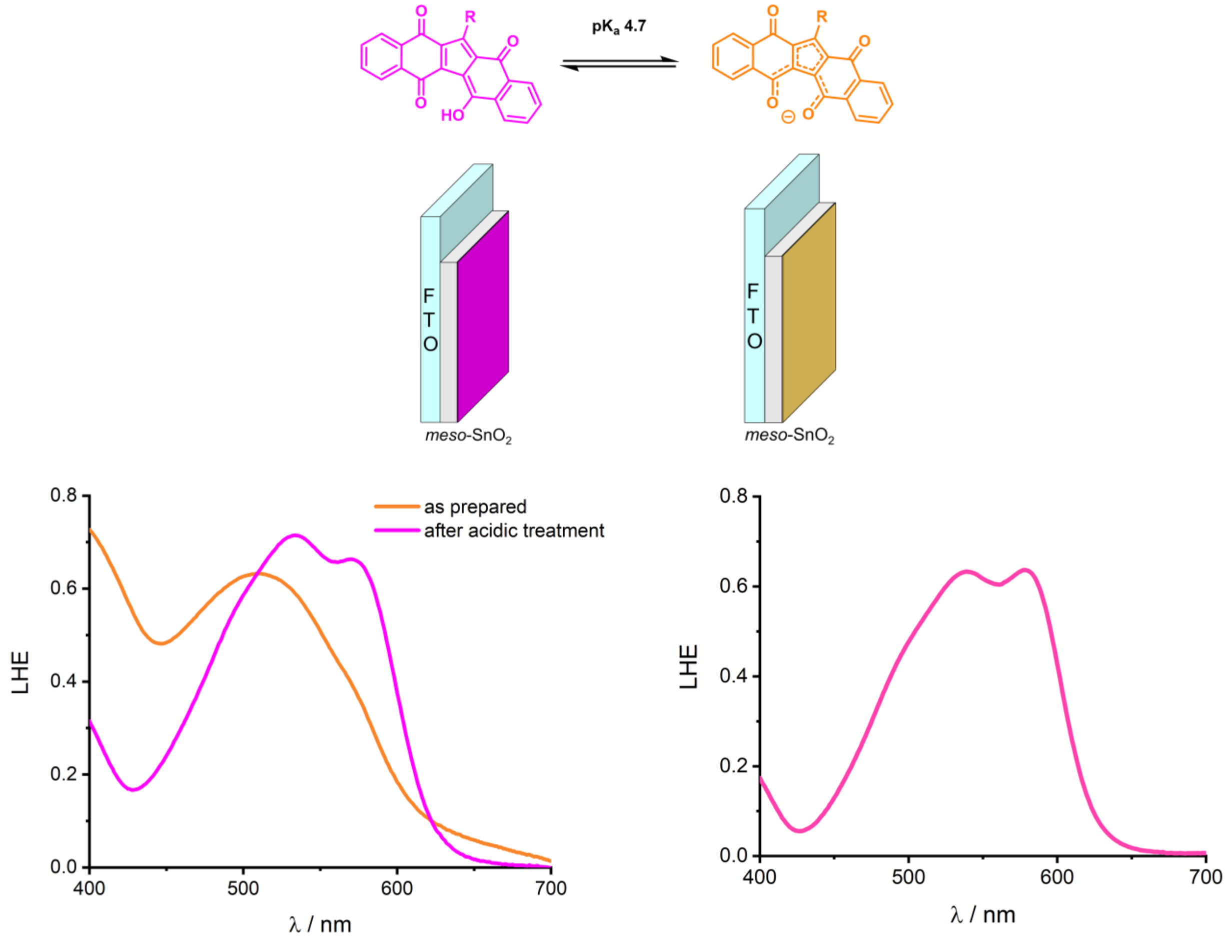

Figure S47. Top: acid-base equilibrium involving the enol (pink) and enolate (orange) forms of **KuQ**, occurring both in solution and on the SnO_2 photoelectrodes. **Bottom left:** electronic absorption spectra expressed as a function of LHE for SnO_2|**KuQ3C** photoelectrodes containing the enol (pink line) and enolate (orange line) of **KuQ3C**. **Bottom right:** electronic absorption spectra expressed as a function of LHE for SnO_2|**KuQ3P**.

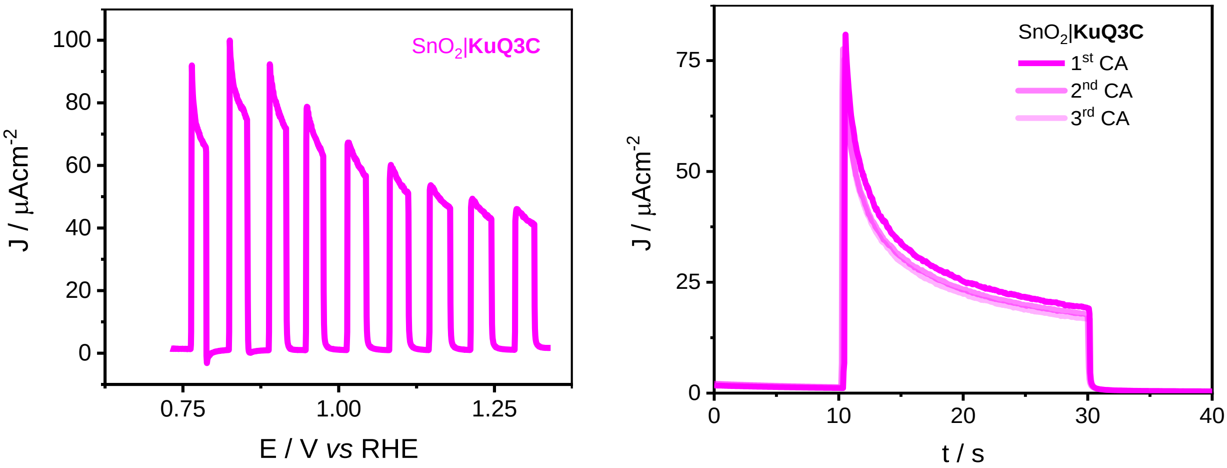

Figure S48. Left: LSV trace under chopped illumination (100 mW·cm^{-2} simulated visible solar light, λ > 400 nm) of SnO_2|**KuQ3C** photoelectrodes, registered in $NaHCO_3/Na_2SiF_6$ (pH 5.8) electrolyte, scan rate 0.020 V·s^{-1}. **Right:** chronoamperograms of SnO_2|**KuQ3C** photoelectrodes registered at 1.14 V *vs* RHE in $NaHCO_3/Na_2SiF_6$ (pH 5.8) electrolyte.

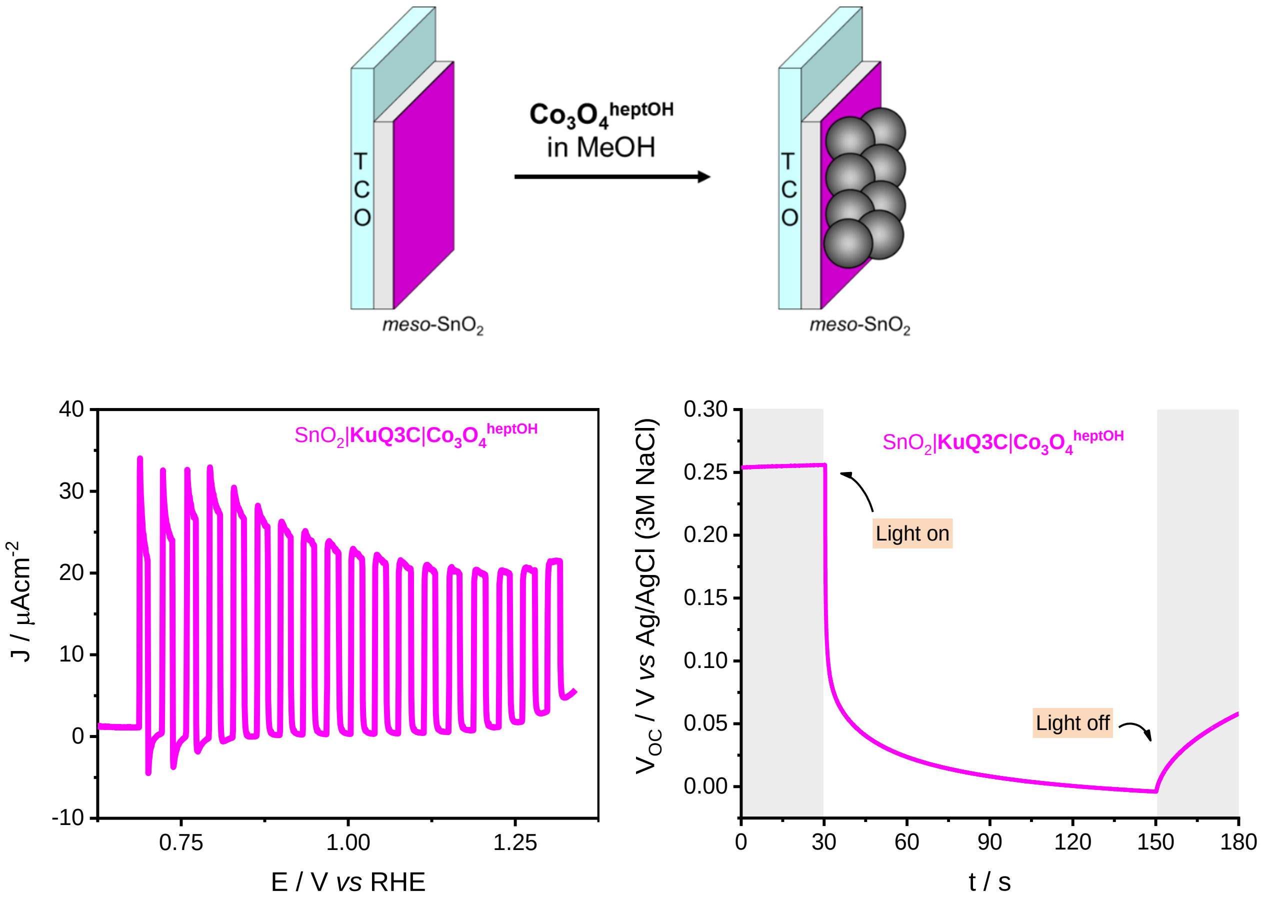

Figure S49. Top: Schematic functionalization procedure of SnO_2|**KuQ3C** photoelectrodes by deposition of $\mathbf{Co_3O_4^{heptOH}}$. **Bottom left:** LSV trace under chopped illumination of SnO_2|**KuQ3C**|$\mathbf{Co_3O_4^{heptOH}}$ photoelectrodes, registered at a scan rate 0.020 V·s^{-1}. **Bottom right:** Open-circuit chronopotentiograms recorded under dark (30 s), under illumination (120 s), and under dark (30 s) for SnO_2|**KuQ3C**|$\mathbf{Co_3O_4^{heptOH}}$. All experiments were performed in $NaHCO_3/Na_2SiF_6$ (pH 5.8) electrolyte. Illumination was performed with 100 mW·cm^{-2} simulated visible solar light, λ > 400 nm.

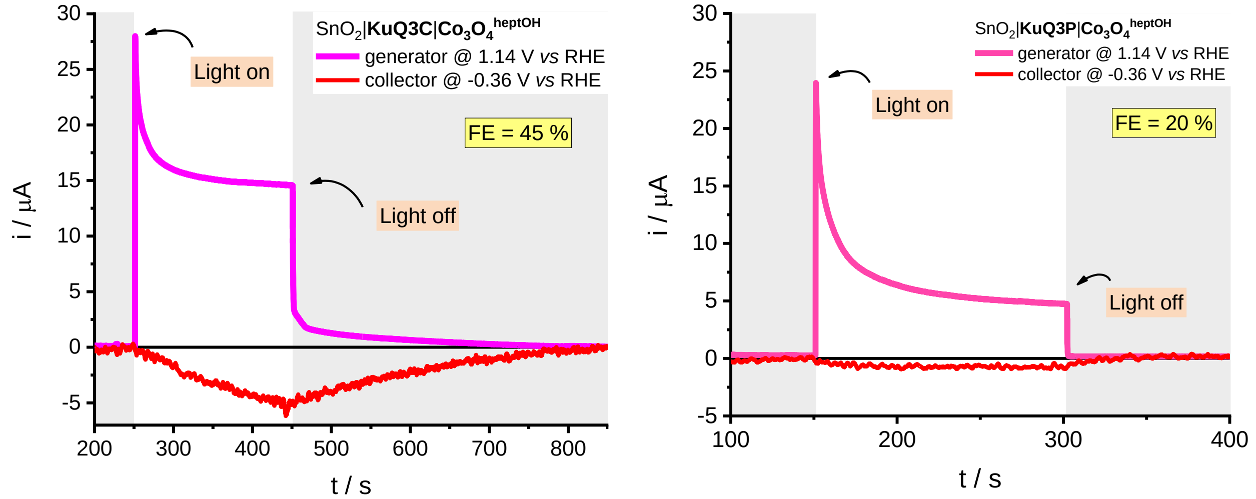

Figure S50. Chronoamperograms recorded in a two-plate generator-collector setup to detect evolved O_2 on “unbound” photoanodes. **Left:** SnO_2|**KuQ3C**|$\mathbf{Co_3O_4^{heptOH}}$. **RightA:** SnO_2|**KuQ3P**|$\mathbf{Co_3O_4^{heptOH}}$. The generator was poised at 1.14 V *vs* RHE and illuminated (100 mW·cm^{-2} simulated visible solar light, λ > 400 nm), the collector was poised at –0.36 V *vs* RHE, registered in $NaHCO_3/Na_2SiF_6$ (pH 5.8) electrolyte.

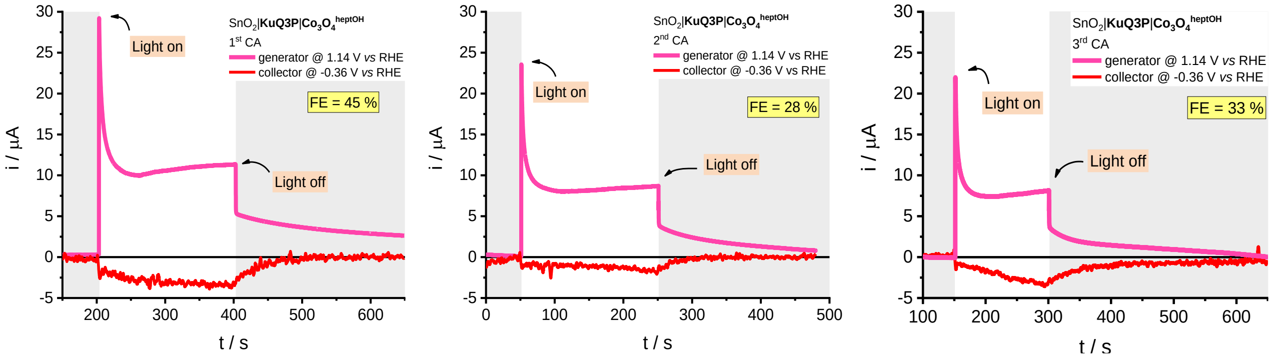

Figure S51. Consecutive chronoamperograms recorded in a two-plate generator-collector setup to detect evolved O_2 on "unbound" SnO_2|**KuQ3P|$Co_3O_4^{heptOH}$** photoanodes. The generator was poised at 1.14 V *vs* RHE and illuminated (100 mW·cm^{-2} simulated visible solar light, λ > 400 nm), the collector was poised at –0.36 V *vs* RHE, registered in $NaHCO_3/Na_2SiF_6$ (pH 5.8) electrolyte.

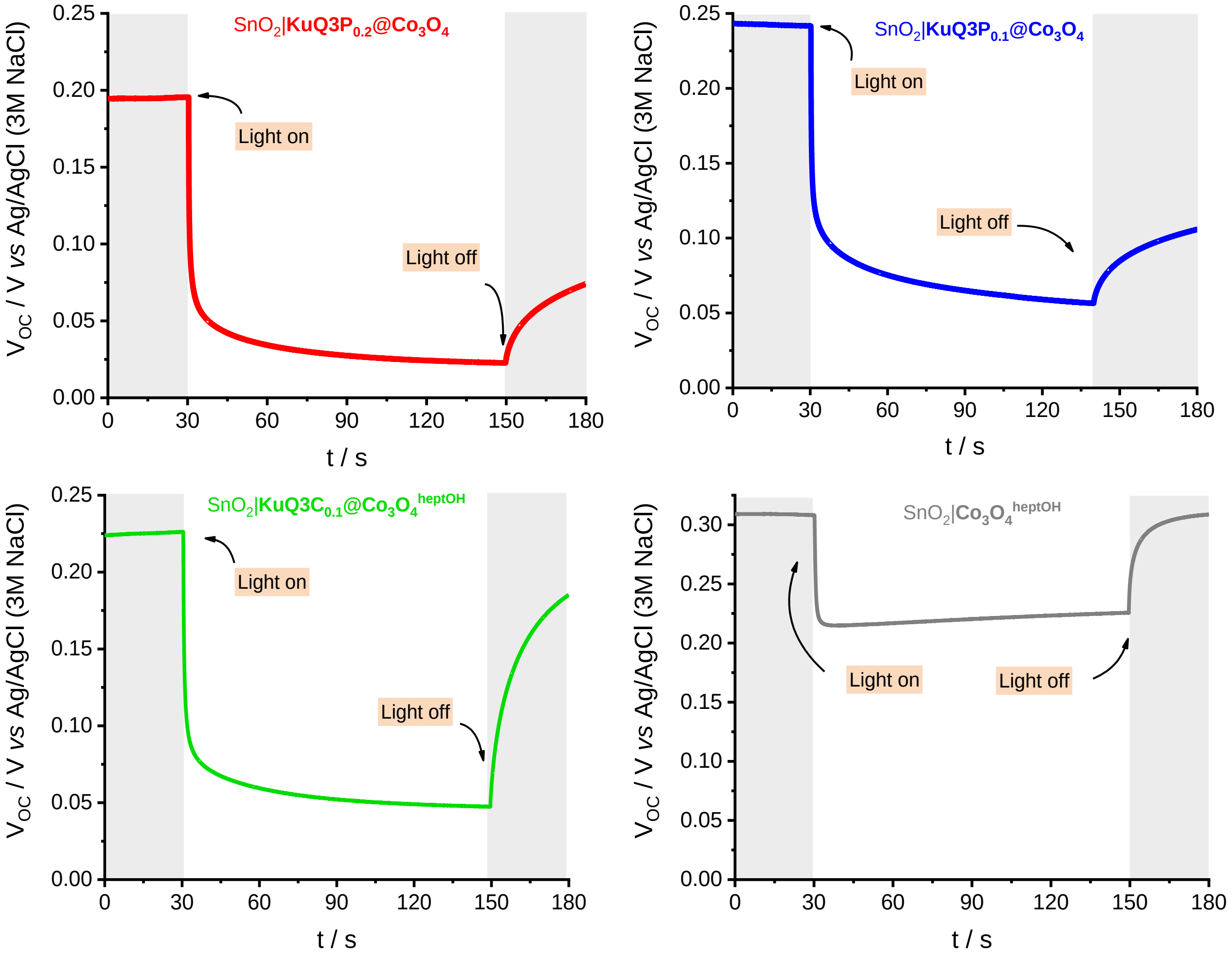

Figure S52. Open-circuit chronopotentiograms recorded under dark (30 s), under illumination (120 s), and under dark (30 s). **Top left** (red line): **KuQ3P$_{0.2}$@Co_3O_4**. **Top right** (blue line): **KuQ3P$_{0.1}$@Co_3O_4**. **Bottom left** (green line): **KuQ3C$_{0.1}$@Co_3O_4. Bottom right** (grey line): **$Co_3O_4^{heptOH}$**. Measurements were recorded in $NaHCO_3/Na_2SiF_6$ (pH 5.8) electrolyte. Illumination was performed with 100 mW·cm^{-2} simulated visible solar light, λ > 400 nm.

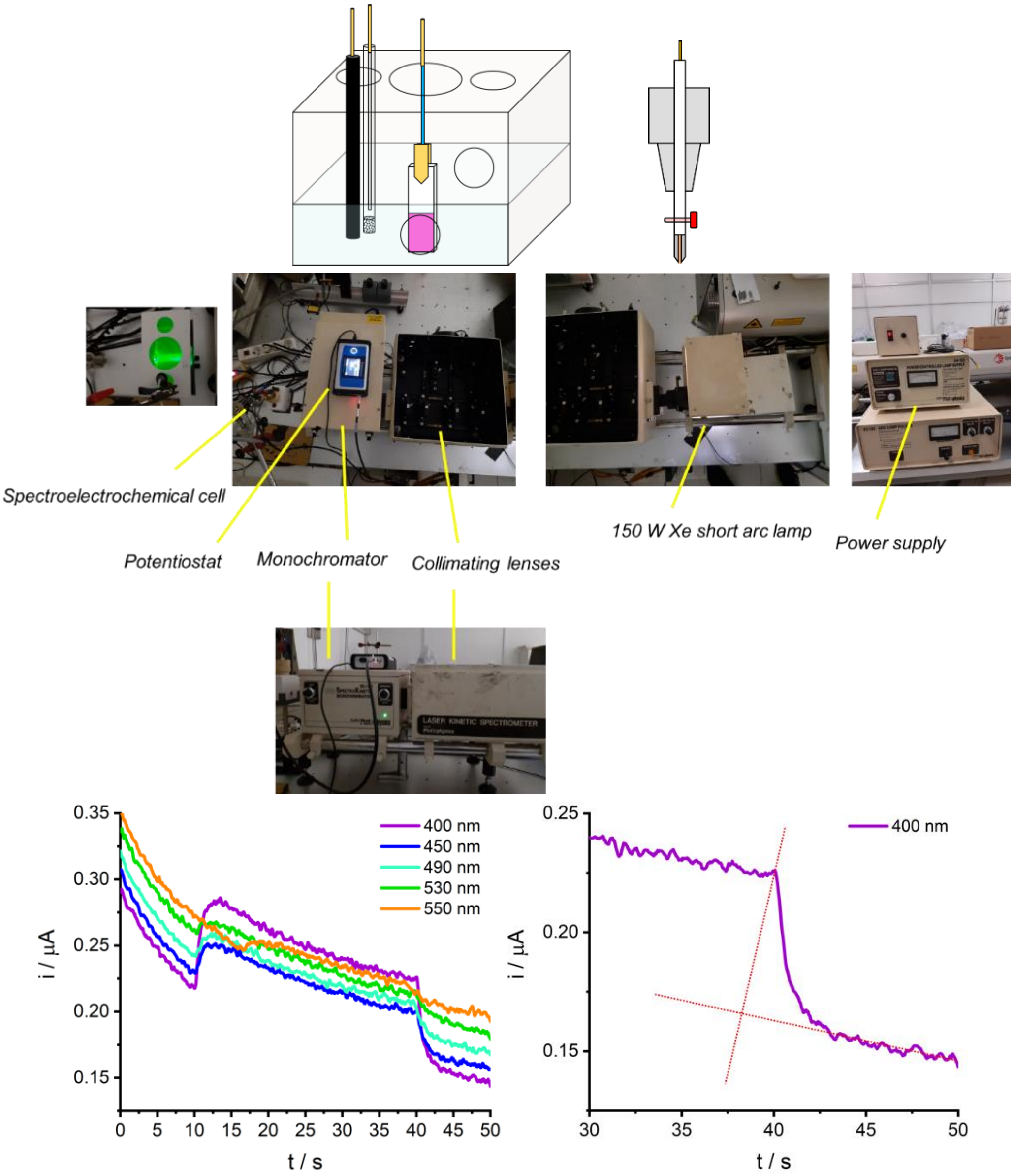

Figure S53. Top: Schematic view of the custom-made cell used for registering the IPCE photo-action spectra. **Middle:** photophysical setup used in the study with the Xe lamp source. **Bottom:** chronoamperograms recorded at 1.14 V *vs* RHE under monochromatic irradiation, in $NaHCO_3/Na_2SiF_6$ (pH 5.8) electrolyte. Photocurrent determination procedure is displayed (CA under irradiation with 400 nm light is displayed for exemplificative purposes).

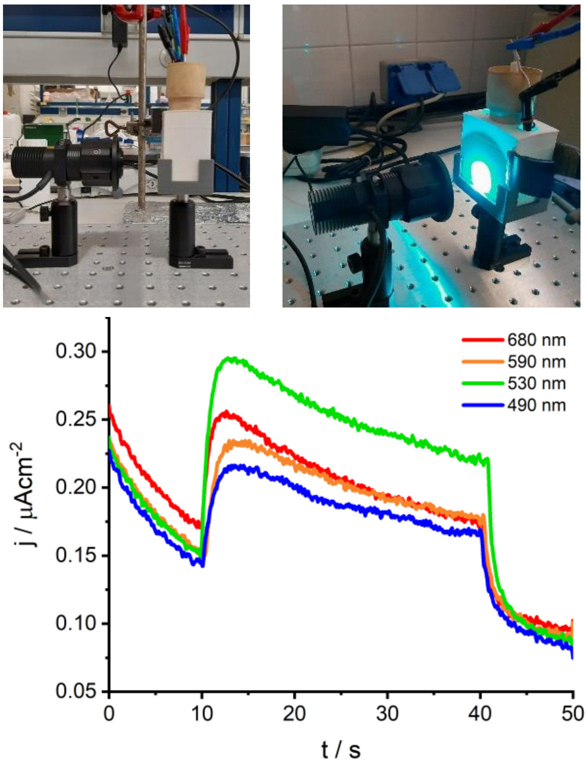

Figure S54. Top: setup used for registering the IPCE photo-action spectrum with LED sources. **Bottom:** chronoamperograms recorded at 1.14 V *vs* RHE different wavelengths with LED sources, in $NaHCO_3/Na_2SiF_6$ (pH 5.8) electrolyte.

System	FE$_{O_2}$ (%)	IPCE (%) @ λ	Conditions	Reference
WO_3|**(PBI$^+$)$_5$@Ru$_4$(POM)** *[a]*	> 97	0.5 @ 490 nm	pH 3 $HClO_4$/$NaClO_4$ 100 mW·cm^{-2} AM 1.5G λ > 450 nm	*Nat. Chem.*, 2019, **11**, 2, 146–153
nano-ITO|**(PBI$^+$)$_5$@Ru$_4$(POM)** *[a]*	> 95	1.2 @ 500 nm	pH 7 $NaHCO_3$ 850 mW·cm^{-2} AM 1.5G λ > 450 nm	*J. Am. Chem. Soc.*, 2022, **144**, 14021–14025
SnO_2|**Ru(bpy)$_3$^{P}**\|^L|**Ru(bda)** *[b,c,d]*	86	29 @ 450 nm	pH 4.56 acetate buffer/$NaClO_4$ 100 mW·cm^{-2} λ > 400 nm	*J. Phys. Chem. C*, 2019, **123**, 30039−30045
TiO_2|**Ru(bpy)$_3$^{P}**\|^L\|**ICZ**\|^L|**Ru(bda)** *[b,c,d,e]*	> 94	19 @ 465 nm	pH 7 phosphate buffer/Na_2SO_4 100 mW·cm^{-2} AM 1.5G λ > 400 nm	*J. Energy Chem.*, 2024, **93**, 526–537
TiO_2|**Ru(bpy)$_3$^{P,CD}@Ru(bda)** *[f]*	68–72	7 @ 460 nm	pH 7 phosphate buffer/CF_3CH_2OH 300 mW·cm^{-2} AM 1.5G λ > 400 nm	*ChemPlusChem*, 2016, **81**, 1056–1059
TiO_2|**IrOx@Ru(bpy)$_3$^{P,M}** *[g]*	up to 100	0.4-0.7 @ 450 nm	pH 5.75 $NaHCO_3$/Na_2SiF_6/Na_2SO_4 100 mW·cm^{-2} λ > 410 nm; H_2O filter	*J. Am. Chem. Soc.*, 2009, **131**, 3, 926–927
FTO|**Ru(phen)$_3$^{P}@Fe-FeOx** *[b]*	*n.d.*	*n.d.*	pH 13 NaOH 100 mW·cm^{-2} λ > 420 nm	*ACS Appl. Mater. Interfaces*, 2021, **13**, 45, 53829–53840
ITO|**PBI^P**|**CoO$_x$** *[b]*	80	1.2 @ 475 nm	pH 7 phosphate buffer 100 mW·cm^{-2} 315 nm < λ < 710 nm	*ACS Appl. Mater. Interfaces*, 2014, **6**, 13367−13377
SnO_2|**PBI^P**|**CoO$_x$** *[b]*	31	*n.d.*	pH 7 phosphate buffer 100 mW·cm^{-2} AM 1.5G λ > 400 nm	*ACS Appl. Mater. Interfaces*, 2017, **9**, 27625−27637
SnO_2|**KuQ3P$_n$@Co$_3$O$_4$**	87–88	0.44	pH 5.8 $NaHCO_3$/Na_2SiF_6 100 mW·cm^{-2} AM 1.5G λ > 400 nm	*This work*

Table S6. Comparison of different dye-sensitized photoanodic systems based on a supramolecular assembly of molecular and/or nanostructured components. Photocurrent was not considered due to the variety of the conditions explored. *[a] The label **PBI$^+$** indicates a cationic perylene bisimide dye. [b] The superscript **P** indicates a phosphonate anchoring group in the ligand structure; **bpy** = 2,2'-bipyridine; **phen** = phenanthroline. [c] **bda** = 2,2'-bipyridine-4,4'-dicarboxylic acid [d] The superscript **L** indicates intermolecular interaction through an alkyl chain bilayer. [e] The label **ICZ** indicates the 5,11-di(octan-3-yl)-4a,5,11,12b-tetrahydroindolo[3,2-b] carbazole ET mediator. [f] The superscript **P,CD** indicates formation of a WOC-dye interfacial inclusion complex involving a cyclodextrin-functionalized Ru(bpy)$_3$ analogue, anchored to TiO_2 by a phosphonate group. [g] The superscript **P,M** indicates the simultaneous presence of a phosphonate moiety for binding to TiO_2 and a malonate anchoring group connected to the IrOx NPs.*

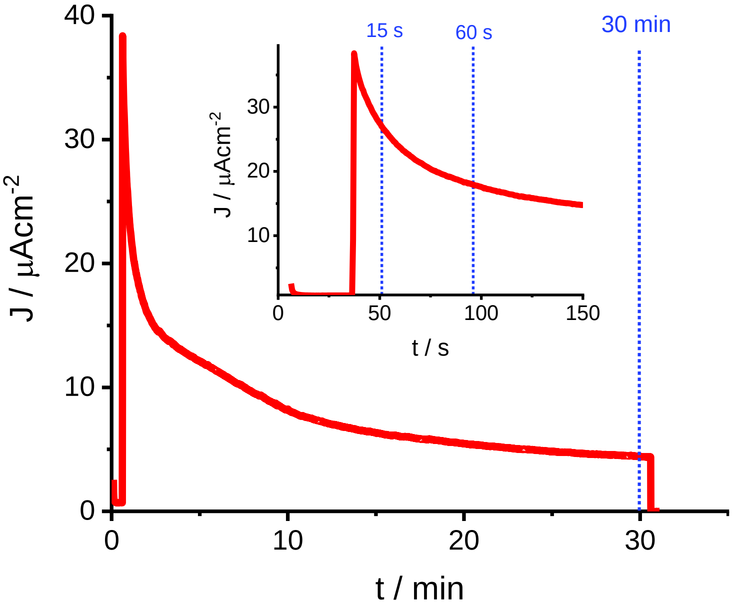

Figure S55. Photoelectrolysis (1 h) on SnO_2|**$KuQ3P_{0.2}$@Co_3O_4** photoelectrodes (1.14 V *vs* RHE, $NaHCO_3$/Na_2SiF_6 pH 5.8 electrolyte), displaying time labels corresponding to the various samples tested for *ex situ* XAS. Illumination was performed with 100 mW·cm^{-2} simulated visible solar light, λ > 400 nm.

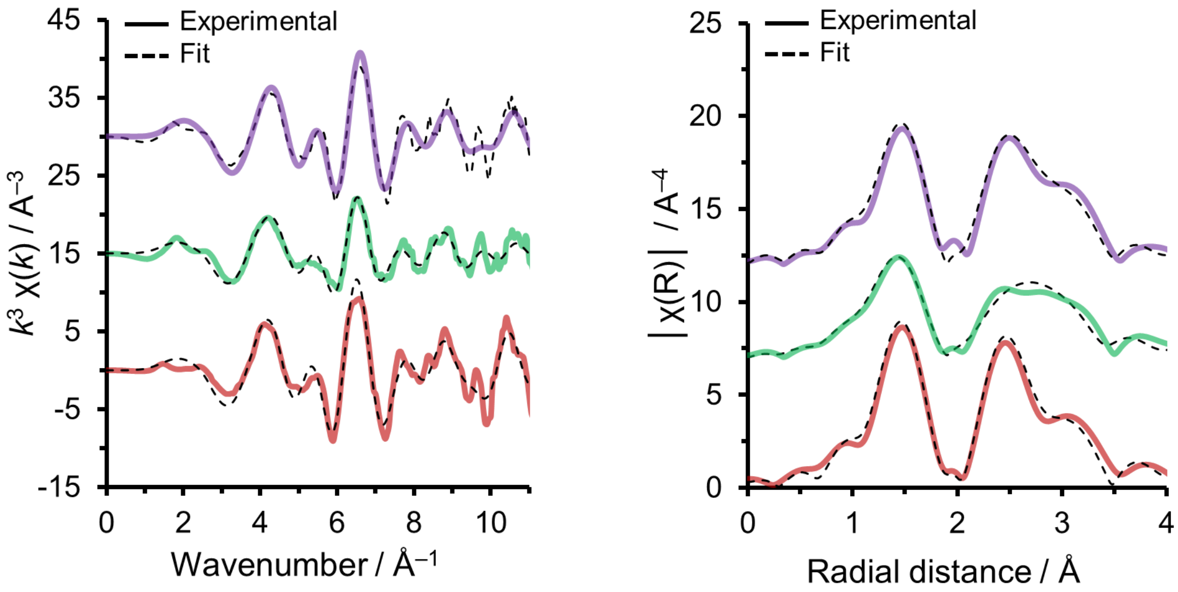

Figure S56. Left: Evolution of k^3-weighted Co EXAFS of **$Co_3O_4^{heptOH}$** (wine line), SnO_2|**$KuQ_{0.2}$@Co_3O_4** (green line) and SnO_2|**$KuQ_{0.2}$@Co_3O_4** after 30 mins of photoelectrocatalysis (purple line) using 100 mW·cm^{-2} simulated visible solar light, λ > 400 nm at E_{app} = 1.14 V *vs* RHE in $NaHCO_3$/Na_2SiF_6 (pH 5.8) electrolyte. Experimental data are represented as solid lines and fitted data as dashed lines. Experimental spectra were fitted for over a k-range 3–11 Å^{-1}. **Right:** Evolution of the Fourier transforms for k^3-weighted for the same samples. Experimental data are represented as solid lines and fitted data as dashed lines. Experimental spectra were fitted for over a k-range 3–11 Å^{-1}.

Sample	**Region**	**Shell, N**	**R, Å**	**σ^2 (10^{-3} Å^2)**	**S_0^2**	**E_0, eV**	**R-factor**	**Reduced χ^2**
$Co_3O_4^{heptOH}$	k = 3 – 11 Å^{-1}	Co-O, 5.3	1.92	6.1	0.9	-4.4	0.023	101
Co K-edge	R = 1 – 4.2 Å	Co-Co, 4	2.86	7.9				
		Co-Co, 8	3.36	12.4				
		Co-O, 3.2	4.31	1.8				
$KuQ3P_{0.2}@Co_3O_4$	k = 3 – 11 Å^{-1}	Co-O, 5.3	1.90	11.4	0.9	-4.5	0.048	71
Co K-Edge	R = 1 – 4.2 Å	Co-Co, 4	2.87	19.1				
		Co-Co, 8	3.33	14.9				
		Co-O, 3.2	4.23	4.3				
$KuQ3P_{0.2}@Co_3O_4$ After photoelectrocatalysis (t = 30 min)	k = 3 – 11 Å^{-1}	Co-O, 5.3	1.92	8.5	0.9	-1.0	0.028	66
Co K-Edge	R = 1 – 4.2 Å	Co-Co, 4	2.85	9.9				
		Co-Co, 8	3.34	12.5				
		Co-O, 3.2	4.25	3.1				

Table S7. EXAFS fitting parameters for **$Co_3O_4^{heptOH}$** and for **$KuQ3P_{0.2}@Co_3O_4$** before and after 30 min photoirradiation (100 mW·cm^{-2} simulated visible solar light, λ > 400 nm).

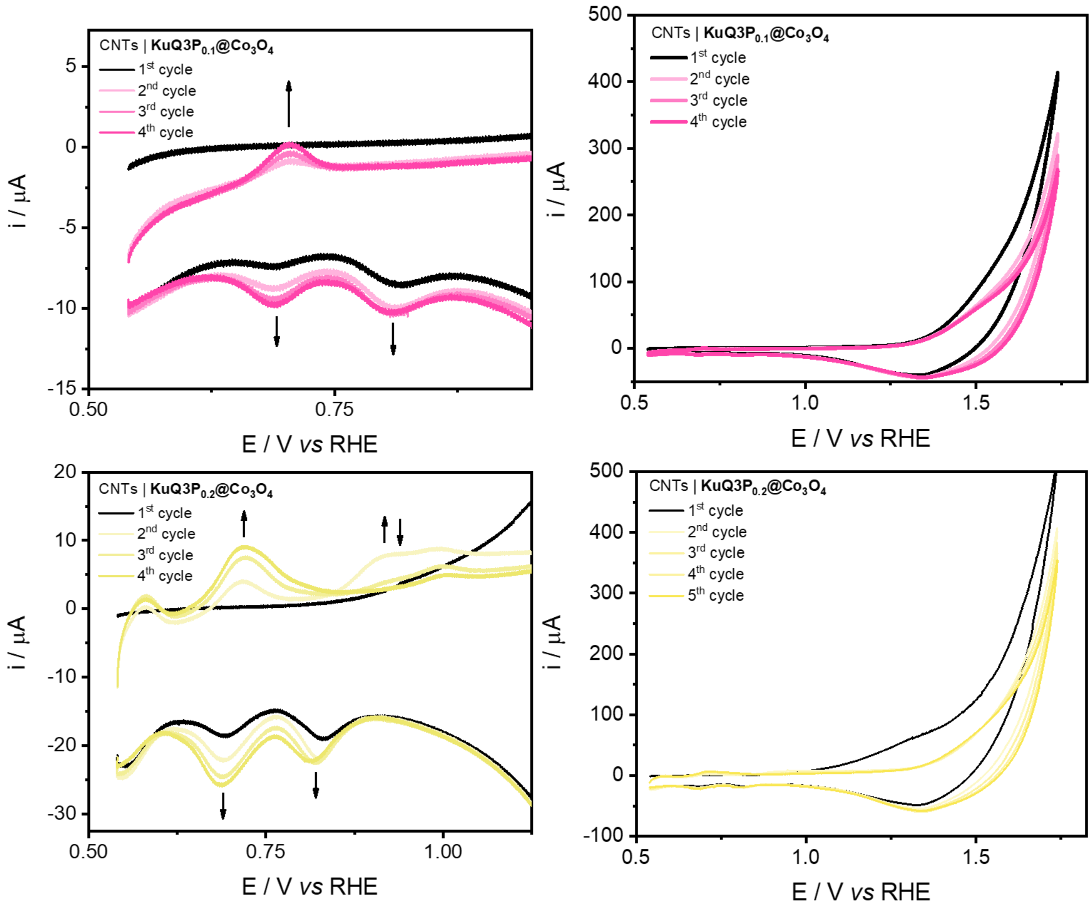

Figure S57. CV traces of **KuQ3P$_{0.1}$@Co$_3$O$_4$** (**top**) and **KuQ3P$_{0.2}$@Co$_3$O$_4$** (**bottom**) (1.0 mg·mL^{-1} in ethanol) loaded onto multi-walled carbon nanotubes (5.0 mg·mL^{-1}), CNTs|**KuQ3P$_n$@Co$_3$O$_4$**, and dropcasted on FTO electrodes (250 µL·cm^{-2}). Conditions: NaHCO$_3$/Na$_2$SiF$_6$ (pH 5.8) electrolyte, 0.020 V·s^{-1}. **Note:** two novel cathodic features (peak potentials at 0.69 and 0.80 V *vs* RHE) are observed on the first backward scan (black line) after accessing the water oxidation regime; their peak current gradually increase upon subsequent cycling (colored lines). Likewise, a corresponding anodic feature (peak potential at 0.70 V *vs* RHE) appears and its current increases from the second cycle onwards. These novel features are ascribed to the formation of CoO(OH) as a result of surface over-oxidation of the starting Co$_3$O$_4$ NPs. The different behavior compared to that observed in **Figure S20** is ascribed to the more intimate contact between the WOC NPs and the electrode provided by the CNTs in the present case.

14. References

[1] J. De Tovar, N. Romero, S. A. Denisov, R. Bofill, C. Gimbert-Suriñach, D. Ciuculescu-Pradines, S. Drouet, A. Llobet, P. Lecante, V. Colliere, Z. Freixa, N. McClenaghan, C. Amiens, J. García-Antón, K. Philippot and X. Sala, *Mater Today Energy*, 2018, **9**, 506–515.
[2] M. Forchetta, V. Conte, G. Fiorani, P. Galloni and F. Sabuzi, *Organics*, 2021, **2**, 107–117.
[3] M. Bonomo, F. Sabuzi, A. Di Carlo, V. Conte, D. Dini and P. Galloni, *New J. Chem.*, 2017, **41**, 2769–2779.
[4] A. Coletti, S. Lentini, V. Conte, B. Floris, O. Bortolini, F. Sforza, F. Grepioni and P. Galloni, *J. Org. Chem*., 2012, **77**, 6873–6879.
[5] B. K. Teo and N. J. A. Sloane, *Inorg. Chem.*, 1985, **24**, 26, 4545–4558.
[6] I. Bazzan, A. Volpe, A. Dolbecq, M. Natali, A. Sartorel, P. Mialane and M. Bonchio, *Catal. Today*, 2017, **290**, 39–50.
[7] N. Du, H. Zhang, B. Chen, J. Wu, X. Ma, Z. Liu, Y. Zhang, D. Yang, X. Huang and J. Tu, *Adv. Mater.*, 2007, **19**, 4505–4509.
[8] G. A. Volpato, M. Marasi, T. Gobbato, F. Valentini, F. Sabuzi, V. Gagliardi, A. Bonetto, A. Marcomini, S. Berardi, V. Conte, M. Bonchio, S. Caramori, P. Galloni and A. Sartorel, *Chem. Commun.*, 2020, **56**, 2248–2251.
[9] G. A. Volpato, E. Colusso, L. Paoloni, M. Forchetta, F. Sgarbossa, V. Cristino, M. Lunardon, S. Berardi, S. Caramori, S. Agnoli, F. Sabuzi, P. Umari, A. Martucci, P. Galloni and A. Sartorel, *Photochem. Photobiol. Sci.*, 2021, **20**, 1243–1255.
[10] H. Park, E. Bae, J.-J. Lee, J. Park and W. Choi, *J. Phys. Chem. B*, 2006, **110**, 8740–8749.
[11] B. Ravel,and M. Newville, *J. Synchrotron Rad.*, 2005, **12**, 537–541.
[12] W. F. Finney, E. Wilson, A. Callender, M. D. Morris and L. W. Beck, *Environ. Sci. Technol.*, 2006, **40**, 8, 2572–2577.
[13] H.-C. Chen, D. G. H. Hetterscheid, R. M. Williams, J. I. van der Vlugt, J. N. H. Reek and A. M. Brouwer, *Energy Environ. Sci.*, 2015, **8**, 975–982.
[14] J. R. Swierk and T. E. Mallouk, *Chem. Soc. Rev.*, 2013, **42**, 2357–2387.
[15] T. Gobbato, F. Rigodanza, E. Benazzi, P. Costa, M. Garrido, A. Sartorel, M. Prato and M. Bonchio, *J. Am. Chem. Soc.*, 2022, **144**, 14021–14025.
[16] B. D. Sherman, M. V. Sheridan, C. J. Dares and T. J. Meyer, *Anal. Chem.*, 2016, **88**, 7076–7082.
[17] D. S. Ellis, Y. Piekner, D. A. Grave, P. Schnell and A. Rothschild, *Front. Energy Res.*, 2022, **9**, 726069.
[18] Y. H. Lai, M. Kato, D. Mersch and E. Reisner, *Faraday Discuss.*, 2014, **176**, 199–211.
[19] J. T. Kirner, J. J. Stracke, B. A. Gregg and R. G. Finke, *ACS Appl. Mater. Interfaces*, 2014, **6**, 13367–13377.
[20] J. T. Kirner and R. G. Finke, *ACS Appl. Mater. Interfaces*, 2017, **9**, 27625–27637.
[21] M. Natali, F. Nastasi, F. Puntoriero and A. Sartorel, *Eur. J. Inorg. Chem.*, 2019, **15**, 2027–2039.
[22] V. Venkatraman, A. E. Yemene and J. de Mello, *Sci. Rep.*, 2019, **9**, 16983.
[23] C. F. Jewell, A. Subramanian, C.-Y. Nam and R. G. Finke, *ACS Appl. Mater. Interfaces*, 2022, **14**, 22, 25326–25336.
[24] J. R. Swierk, N. S. McCool, T. P. Saunders, G. D. Barber and T. E. Mallouk, *J. Am. Chem. Soc.*, 2014, **136**, 10974–10982.
[25] J. R. Swierk, N. S. McCool, T. P. Saunders, G. D. Barber, M. E. Strayer, N. M. Vargas-Barbosa and T. E. Mallouk, *J. Phys. Chem. C*, 2014, **118**, 17046–17053.
[26] J. R. Swierk, N. S. McCool and T. E. Mallouk, *J. Phys. Chem. C*, 2015, **119**, 13858–13867.
[27] M. S. Song, M. A. Mahadik, P. Anushkkaran, J.-H. Park, W.-S. Chae, H. H. Lee and J. S. Jang, *Chemosphere*, 2024, **361**, 142554.
[28] F. Sabuzi, S. Lentini, F. Sforza, S. Pezzola, S. Fratelli, O. Bortolini, B. Floris, V. Conte and P. Galloni, *J. Org. Chem.*, 2017, **82**, 10129–10138.
[29] F. Valentini, F. Sabuzi, V. Conte, V. N. Nemykin and P. Galloni, *J. Org. Chem.*, 2021, **86**, 5680–5689.
[30] S. Ardo and G. J. Meyer, *Chem. Soc. Rev.*, 2009, **38**, 115–164.
[31] W. Kang, R. Wei, H. Yin, D. Li, Z. Chen, Q. Huang, P. Zhang, H. Jing, X. Wang and C. Li, *J. Am. Chem. Soc.*, 2023, **145**, 3470–3477.
[32] J. T. Kirner and R. G. Finke, *J. Mater. Chem. A Mater.*, 2017, **5**, 19560–19592.
[33] J. Zhou, Y. Wang, X. Su, S. Gu, R. Liu, Y. Huang, S. Yan, J. Li and S. Zhang, *Energy Environ. Sci.*, 2019, **12**, 739–746.
[34] N. Wu, L. Fu, M. Su, M. Aslam, K. C. Wong and V. P. Dravid, *Nano Lett.*, 2004, **4**, 2, 383–386.